LUDWIG-MAXIMILIANS-UNIVERSITÄT MÜNCHEN

MASTER'S THESIS

Optimization of a high-energy few-cycle optical parametric chirped pulse amplifier system

Optimierung eines hochenergetischen, breitbandigen optischen parametrischen Verstärkersystems für gechirpte Pulse

Pascal Jordan Weinert

April 19, 2016

Abstract

In this thesis, various methods are investigated to enhance the performance of the LWS-20, a two-color pumped four-stage noncollinear OPCPA (NOPCPA)-based laser system delivering high-intensity few-cycle laser pulses. The focus has been laid on pulse energy, spectral bandwidth and carrier-envelope phase stability.

In the first and larger part, $(2+1)$-dimensional split-step simulations of the NOPCPA amplifier stages have been performed including all second-order nonlinear processes and self-phase modulation. Firstly, the present configuration has been simulated and analyzed. The simulations indicate that the quantum efficiency of the overall system is not yet optimal a gap is observed experimentally between the spectral parts of the stages pumped with 532 nm (green) and those pumped with 355 nm (blue) laser light. Subsequently, various parameter scans were performed in order to develop strategies for increasing the output energy and eliminating the spectral gap.

A way to increase the output energy is to increase the pump intensity. The simulations suggest benefits from a moderate decrease of the pump beam radius before detrimental saturation effects appear, in accordance with an experimental scan where the pump energy was varied.

For the spectral gap, an additional crystal behind each blue-pumped stage and possibly one behind the second green-pumped stage with a different crystal angle are most promising. An approach of replacing the present crystal by two thinner crystals each individually detuned for an overall broader gain does not produced considerably better results but adds increased complexity in the alignment process.

In the second part, the possibility of passive seed carrier-envelope phase stabilization by intra-pulse difference-frequency generation and subsequent wavelength-shifting was investigated experimentally in the laser system. The achievable conversion efficiencies are too low for an implementation.

Supervisors
Prof. Dr. László Veisz and Prof. Dr. Ferenc Krausz
Max-Planck-Institut für Quantenoptik
Lehrstuhl für Laserphysik, Ludwig-Maximilians-Universität München

Contents

Introduction **1**

1 Fundamentals **3**
1.1 Nonlinear optics . . . 3
1.1.1 Frequency mixing . . . 3
1.1.2 Effective nonlinearity . . . 4
1.1.3 Collinear phase matching . . . 5
1.1.4 Nonlinearity of the refractive index . . . 6
1.2 Optical parametric chirped-pulse amplification . . . 6
1.2.1 Amplification principle . . . 7
1.2.2 Noncollinear phase matching . . . 8
1.2.3 Evolution of the electromagnetic fields . . . 12
1.3 Carrier-envelope phase stability . . . 13
1.3.1 Carrier-envelope phase and Carrier-envelope offset . . . 13
1.3.2 Measuring the CEO of a pulse train . . . 14
1.3.3 Single-shot CEO measurement . . . 15

2 LWS-20 laser system **17**
2.1 kHz front-end . . . 17
2.2 Noncollinear OPCPA . . . 18

3 NOPCPA simulations **23**
3.1 Simulation principle . . . 23
3.1.1 Computing ressources . . . 26
3.2 Suitable NOPCPA geometries . . . 27
3.2.1 Angular sensitivity . . . 28
3.2.2 PVWC vs. TPM geometry . . . 28
3.2.3 Stage 1A . . . 29
3.2.4 Stage 2A . . . 32
3.2.5 Stages 1B and 2B . . . 33
3.3 Influence of the pump intensity on the amplification . . . 36
3.3.1 Pump radius variation . . . 36
3.3.2 Pump energy variation . . . 40
3.4 Additional crystals for broader phase-matching . . . 41
3.4.1 Additional crystals . . . 41

3.4.2 Detuning the A crystals . . . 48

4 Difference-frequency generation **49**
4.1 Setup . . . 49
4.1.1 Phase matching . . . 50
4.2 Results and discussion . . . 53
4.2.1 Phase-matching types . . . 53
4.2.2 Spectral features . . . 54
4.2.3 Conversion efficiency . . . 55
4.3 Alternative for CEP stability . . . 56

5 Conclusions **57**

Appendix **III**

A Dispersion formulae **III**
A.1 Refractive index . . . III
A.2 Group velocity and spectral phase . . . IV

B List of Abbreviations **V**

C List of Figures **IX**

D List of Tables **XI**

E Bibliography **XIII**

Introduction

After the invention of the first laser in 1960 [1], pulsed lasers have continuously gained growing interest in research, particularly because of the high reachable peak powers which were needed for example for advancing nonlinear optics. Already in the early days of laser technology, Q-switching was demonstrated [2] and finally, the development of mode-locked lasers [3, 4] provided an irreplaceable tool for the evolution of ultrafast lasers. Since then, pulse durations could be reduced by orders of magnitudes, promoting the rise of time-resolved spectroscopic methods.

Kerr-lens mode-locked Ti:Sapphire lasers [5] are used to this day as a standard workhorse in ultrafast laser science thanks to the broad bandwidth of the active medium allowing to obtain pulses containing only a few optical cycles directly from the oscillator.

Techniques for pulse broadening based on continuum generation [6] and for compression with combinations of gratings, prisms and chirped mirrors [7] have further pushed down the limits of available driving pulses for nonlinear experiments. In parallel, achievable pulse energies were increased by developing chirped-pulse amplification (CPA) schemes [8] being able to yield unprecedented intensities. Optical parametric amplification (OPA) [9, 10] with its broad gain bandwidth and large single-pass gain was applied first in the beginning of the laser era. In the last twenty-five years it gained importance for supporting ultra-short pulses. Especially the combination of CPA and OPA, called optical parametric chirped-pulse amplification (OPCPA) [11], gave rise to unprecedented pulse synthesis options.

With the available techniques, laser pulses can be tailored better and better to the specific needs of highly-nonlinear ultra-fast processes such as laser-plasma interactions like harmonic generation in solids [12]. Therefore, current research in these areas is still pushing the frontiers, especially when both, ultra-short and ultra-high-power pulses are needed.

An example of a laser system employing OPCPA is the Light Wave Synthesizer 20 (LWS-20). It has been under constant development achieving sub-5 fs pulses with outstanding energies of 80 mJ to 90 mJ. This thesis is a part of the ongoing optimization and focuses on the conversion efficiency and bandwidth of the OPCPA stages. As the relative phase between carrier wave and the intensity envelope of ultra-short pulses highly affects the performed experiments, a smaller part assesses the possibility of passive phase stabilization.

1 | Fundamentals

In this chapter, the underlying physics for the work done in this thesis is developed. Very important throughout this work is the exploitation of nonlinear optics, which is why the most important aspects are outlined in the beginning. Afterwards, optical parametric chirped-pulse amplification is described, laying a focus on phase matching issues. Finally, central aspects concerning carrier-envelope phase stability are discussed.

1.1 Nonlinear optics

The huge field of nonlinear optics deals with phenomena connected to the alteration of optical properties of media by sufficiently intense light fields. The fundamental approach is that a material's polarization $\vec{P}$ shows a nonlinear dependence on the electrical field strength $\vec{E}$ [13]:

$$P_i(t) = \underbrace{\varepsilon_0 \int \chi^{(1)}_{ij}(t-t_1)E_j(t_1)\,\mathrm{d}t_1}_{P^{(1)}_i(t)=P_{\mathrm{l},i}(t)} + \underbrace{\varepsilon_0 \iint \chi^{(2)}_{ijk}(t-t_1,t-t_2)E_j(t_1)E_k(t_2)\,\mathrm{d}t_1\,\mathrm{d}t_2 + \ldots}_{P^{(2)}_i(t)+\ldots=P_{\mathrm{nl},i}(t)} \tag{1.1}$$

where ε_0 is the vacuum permittivity and χ the electric susceptibility.

1.1.1 Frequency mixing

Assuming an instantaneous response $\chi^{(n)}(t-t_1,\ldots,t-t_n) = \chi^{(n)}\delta(t-t_1,\ldots,t-t_n)$ and a bichromatic input $\vec{E}(t) = \vec{E}_{0,a}\exp[-\mathrm{i}\omega_a t] + \vec{E}_{0,b}\exp[-\mathrm{i}\omega_b t] + \mathrm{c.c.}$, the second-order nonlinearity will have the following components (sum convention implies summation over twice-occurring indices):

$$\begin{aligned} P^{(2)}_i(t) = \varepsilon_0\chi^{(2)}_{ijk}\Bigg(& \underbrace{E_{0,aj}E_{0,ak}\mathrm{e}^{-2\mathrm{i}\omega_a t}}_{\text{SHG}} + \underbrace{E_{0,bj}E_{0,bk}\mathrm{e}^{-2\mathrm{i}\omega_b t}}_{\text{SHG}} + \underbrace{\left(E_{0,aj}E_{0,bk}+E_{0,bj}E_{0,ak}\right)\mathrm{e}^{-\mathrm{i}(\omega_a+\omega_b)t}}_{\text{SFG}} \\ & + \underbrace{\left(E_{0,aj}E^*_{0,bk}+E^*_{0,bj}E_{0,ak}\right)\mathrm{e}^{-\mathrm{i}(\omega_a-\omega_b)t}}_{\text{DFG}} + \underbrace{E_{0,aj}E^*_{0,ak}+E_{0,bj}E^*_{0,bk}}_{\text{OR}} + \mathrm{c.c.}\Bigg), \end{aligned} \tag{1.2}$$

leading to various frequency components in the polarization. They have double of each of the input frequencies (second harmonic generation, SHG), the sum (SFG) and difference (DFG) of both frequencies or finally, a constant part (optical rectification, OR). These frequencies in the polarization will be transferred to the emitted radiation.

Taking the Fourier transform of the above equation further illustrates the frequency mixing:

$$P_i^{(2)}(\omega_c) = \varepsilon_0 \sum_{\omega_a+\omega_b=\omega_c} \chi_{ijk}^{(2)}(\omega_c;\omega_a,\omega_b) E_j(\omega_a) E_k(\omega_b)\,. \tag{1.3}$$

Here, the sum symbol denotes summation over all permutations of the involved frequencies where $\omega_b = \pm\omega_a$ is possible, too. In this notation, frequencies can be negative, too, which corresponds to the complex conjugate, cf. equation (1.2). Denoting the susceptibility by $\chi_{ijk}^{(2)}(\omega_c;\omega_a,\omega_b)$ reflects that $\omega_a+\omega_b=\omega_c$ which is also the frequency with which the second-order polarization varies.

Very important for the further parts of this thesis is difference-frequency generation (DFG) where an atom is excited to a higher virtual level by absorbing a photon with frequency ω_a. Stimulated by the other field (ω_b), the atom decays back to its initial state in a two-photon process emitting a photon of frequency ω_b and $\omega_c = \omega_a - \omega_b$, each. The same can also happen in the absence of the second electric field by the weaker spontaneous decay of the excited atom. This is known as optical parametric fluorescence (OPF) or spontaneous parametric down-conversion (SPDC) and caused by vacuum fluctuations [14].

1.1.2 Effective nonlinearity

In principle, the given nonlinear susceptibility tensors in the form of equations (1.2) and (1.3) have a very high number of elements. Fortunately, the number of independent elements can be vastly reduced by demanding real fields, restricting to optical frequencies far below the lowest resonance and exploiting a permutation symmetry by coordinate exchange [14, 15]. For beta barium borate (BBO) which is one of the most commonly used nonlinear crystals and which belongs to the point group $3m$ (C_{3v})[1],an effective scalar nonlinearity d_{eff} is used [14, 18, 19]:

$$P^{(2)}(\omega_3) = 4\varepsilon_0 d_{\text{eff}} E(\omega_1) E(\omega_2) \tag{1.4}$$

$$d_{\text{eff}} = \begin{cases} d_{15}\sin\theta - d_{22}\cos\theta\sin 3\phi & \text{for ooe (type I), oeo, eoo} \\ d_{22}\cos^2\theta\cos 3\phi & \text{for eoe (type II), oee (type III), eeo} \end{cases}. \tag{1.5}$$

Here, o and e stand for ordinary and extraordinary polarization, respectively, which is explained in the following section. θ is the angle between optical axis and the beam and ϕ corresponds to the rotation around the rotational symmetry axis. In this thesis the values $d_{22} = 2.22\,\text{pm}\cdot\text{V}^{-1}$ $d_{31} = -0.16\,\text{pm}\cdot\text{V}^{-1}$ [20] are used.

[1] Note that several authors suggest the space group $R3$ rather than $R3c$ for BBO [16, 17], thus implying a point group 3 instead of $3m$. However, the asymmetry is very small which is why $d_{11} = -d_{12} = -d_{26}$ is two orders of magnitude smaller than d_{22} [17] and does not lead to a considerably different effective nonlinearity.

Process	Type I	Type II	Type III
SFG (ω_1, $\omega_2 \rightarrow \omega_3 = \omega_1 + \omega_2$)	o, o → e	e, o → e	o, e → e
DFG (ω_3, $\omega_2 \rightarrow \omega_1 = \omega_3 - \omega_2$)	e, o → o	e, o → o	e, e → o
DFG (ω_3, $\omega_1 \rightarrow \omega_2 = \omega_3 - \omega_1$)	e, o → o	e, e → o	e, o → e

Tab. 1.1: Phase-matching types for SFG and DFG in BBO [21] and $\omega 1 \leq \omega_2 < \omega_3 = \omega_1 + \omega_2$.

1.1.3 Collinear phase matching

Due to chromatic material dispersion (cf. appendix A.1), the phases of the waves included in the process would naturally drift apart over the propagation through the crystal. Components created at different positions will then not add up in phase leading to destructive interference and result in an extremely reduced conversion efficiency. Hence, proper phase matching is necessary to keep this phase mismatch to a minimum. It is proportional to the corresponding wave vector mismatch (WVM)

$$\Delta k := k_3 - k_1 - k_2 = \frac{1}{c}\left(n_3\omega_3 - n_1\omega_1 - n_2\omega_2\right). \tag{1.6}$$

Here, the convention is used that $\omega_1 \leq \omega_2 < \omega_3 = \omega_1 + \omega_2$ for generalization. Furthermore, it is assumed that the waves propagate collinearly resulting in a scalar equation.

The most common way for fulfilling the phase-matching condition $\Delta k = 0$ is to make use of the birefringence of the nonlinear medium. The birefringence results from an anisotropy causing the material response to differ depending on the beam polarization. In the simplest case, the medium is an uniaxial crystal, i.e. has only one distinct and so called optical axis. For the component of the beam that is polarized perpendicularly to the plane of wave vector and optical axis, the refractive index is independent of the direction of the former yielding the name *ordinary*. Contrarily, the refractive index for the *extraordinary* component whose polarization lies in the plane, varies with the beam direction θ (c.f. equation (A.5) and figure 1.3a). For three interacting frequencies, the propagation direction can often be chosen such that the WVM vanishes.

In the usual case of normal dispersion, the frequency-dependence of the refractive index can only be compensated in a birefringent medium if the higher frequency component is polarized such that it experiences the smaller of the two refractive indices n_e or n_o. The corresponding axis is called fast axis and the other one slow axis. In a positive birefringent crystal, the ordinary index is smaller than the extraordinary, $n_o < n_e$, and thus the ordinary axis is the fast axis. BBO is a negative crystal and here, the extraordinary index is smaller. Depending on the crystal, the ordinary axis can have a higher refractive index than the extraordinary axis or a smaller. The former is known as negative and the latter as positive birefringence. Table 1.1 lists all possible phase matching types for different processes. Normally, type I is easiest to achieve, followed by type II . Type III is most difficult and only feasible in crystals with a large birefringence. For interacting pulses of a finite spectral bandwidth, perfect phase matching is only possible at a certain wavelength combination; for all others, the intensity will drop, depending on the crystal length L:

$$I \propto \operatorname{sinc}^2\left(\frac{\Delta k \cdot L}{2}\right) \tag{1.7}$$

assuming plane waves and a low pump intensity [16]. Obviously, the phase-matching bandwidth increases with decreasing crystal length.

1.1.4 Nonlinearity of the refractive index

Another important nonlinearity in materials concerns the refractive index and causes many spatio-temporal effects. As the refractive index is closely related to the susceptibility by

$$n' = \sqrt{1+\chi} \tag{1.8}$$

it behaves nonlinearly with the applied laser intensity as well. It can be shown that the major change scales linearly with the intensity

$$n' = n + n_2 I \tag{1.9}$$

which is known as the optical Kerr effect. In this thesis, the effective refractive index is explicitly denoted with a prime and the intensity-independent refractive index n is not indexed with a zero as usual in order to avoid confusion with the ordinary refractive index n_o. Expansion of equations (1.8) and (1.9) leads to a proportionality of n_2 to the effective $\chi^{(3)}$ [14].

One important feature caused by the nonlinearity of the refractive index is self-focusing which occurs for a positive n_2 due to the higher intensity at the center of a laser beam leading to a so-called Kerr lens for the whole beam. An inhomogeneous beam additionally results in many small lensing effects leading to amplification of the inhomogeneities and can even reach in a break-down into multiple filaments.

The most important temporal effect is called self-phase modulation (SPM) and leads to a phase change of

$$\phi_\mathrm{SPM}(\vec{r},t) = -n_2 I(\vec{r},t)\frac{\omega}{\mathrm{c}}\mathrm{d}z \tag{1.10}$$

when propagating over a distance $\mathrm{d}z$ [18]. The temporal equivalent of self-focusing is pulse steepening at the trailing edge due to the delay imposed on the pulse maximum.

1.2 Optical parametric chirped-pulse amplification

The heart of the LWS-20 laser system is the optical parametric chirped-pulse amplifier (OPCPA) and as such is most interesting to investigate closer. In the following, the focus lies on parametric amplification in BBO crystals. BBO is a negative uniaxial crystal and offers a relatively low dispersion with high birefringence, a large transmission and a phase-matching tunability range spanning from the ultraviolet to the near infrared (NIR) [22, 23] making it very suitable for many second-order applications.

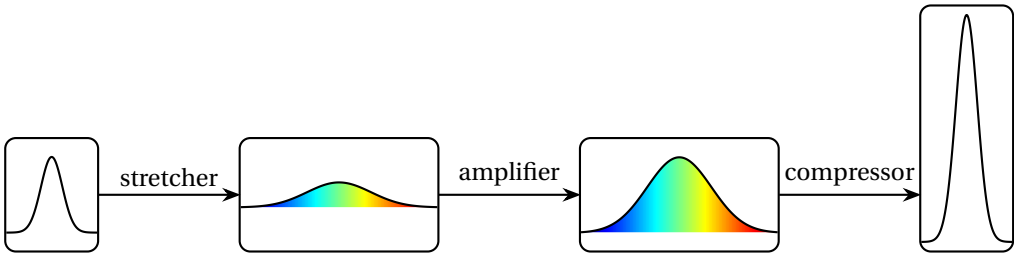

Fig. 1.1: Schematic CPA principle.

1.2.1 Amplification principle

In order to achieve ultra-short high-energy pulses, it is necessary to combine two amplification principles eliminating a few drawbacks at the same time.

Chirped-pulse amplification

Firstly, as mentioned above, highly-intense pulses undergo spatial distortions, notably self-focusing, as well as temporal and spectral distortions caused by the nonlinearities of the media in the beam path. Intensities can even be so high that material damage occurs, for example in the amplifying medium. Since few-femtosecond pulses easily reach high intensities already at moderate pulse energies, the idea is to stretch the pulses in the time domain by imposing a chirp, i.e. a nonlinear and dominantly quadratic spectral phase, on the pulse and thus making it longer and less intense [8]. It is then amplified and subsequently, a compressor removes the chirp, i.e. flattens the spectral phase, resulting in a short and intense pulse [24]. This scheme is called chirped-pulse amplification (CPA) and illustrated in figure 1.1.

Optical parametric amplification

The second principle is called optical parametric amplification (OPA). Traditionally, a laser active medium is used for amplification in regenerative or multi-pass amplifiers. Based on their optical transitions, the gain curve and bandwidth depend on the medium and are fixed. For broadband pulses, gain narrowing plays an important role and can only be partially compensated by spectral filters. Furthermore, the quantum defect in the lasing medium and absorption, amongst others, cause detrimental thermal lensing effects [25, 26].

An OPA, however, has the advantage of high single-pass gain, good wavelength-tunability, little thermal effects due to the non-existent quantum defect in parametric processes, no amplified spontaneous emission (ASE) and a direct response maximizing the amplified pulse contrast. It is a second-order nonlinear process closely related to difference-frequency generation (DFG). As mentioned in section 1.1.1, the lower-frequency input pulse, called *seed* or *signal* in the context of OPA, stimulates the depletion of the virtual level which has been populated by the so-called *pump* pulse. The pump photon (ω_p) thus splits into a signal photon (ω_s) and the *idler* with frequency (cf. figure 1.2)

$$\omega_\mathrm{i} = \omega_\mathrm{p} - \omega_\mathrm{s}\,. \tag{1.11}$$

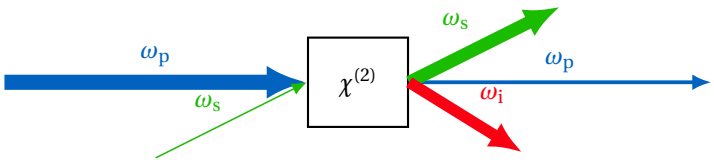

a: Wave picture: Due to the second-order susceptibility, DFG occurs. Arrow lengths represent frequency resp. photon energy.
.

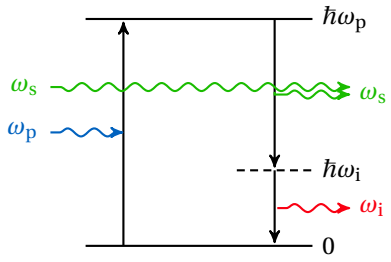

b: Photon picture: The idler photon excites a virtual level which then decays stimulated by a seed photon into another seed photon and an idler photon fulfilling energy conservation .

Fig. 1.2: Principle of optical parametric amplification: the energy from the pump beam gets divided up into the amplified signal and the idler beam.

As mentioned above, parametric fluorescence appears when a pump photon decays spontaneously. If parameters like the phase respectively the pulse length or contrast are important, this is an unwanted process. As it scales with the crystal length, it sets an upper limit to the same.

Due to the principal absence of dissipative effects, very high pump powers can be applied leading to very high single-pass gain. This, and the fact that two femtosecond pulses would quickly separate whilst propagating [27], favors the use of longer, stretched pulses and thus optical parametric chirped-pulse amplification (OPCPA).

1.2.2 Noncollinear phase matching

As discussed in section 1.1.3, perfect phase-matching is only possible for monochromatic waves. This is exactly the problem when a broadband seed like in the LWS-20 laser system (see chapter 2) is to be amplified: the WVM would vanish at only one wavelength (see figure 1.3a) leading to a very small gain bandwidth in a collinear geometry. A simple but effective way to circumvent this restriction is a noncollinear geometry. Here, the pulses do not travel collinearly but pump and signal lie under an angle α. In the following, phase-matching type I is assumed, cf. table 1.1.

Again, ideal phase matching occurs if $\Delta k = 0$, as illustrated in figure 1.3b. The above-mentioned energy conservation (1.11) has to be fulfilled, as well as momentum conservation which has to be treated vectorially now:

$$\Delta\vec{k} := \vec{k}_p - \vec{k}_s - \vec{k}_i \stackrel{!}{=} 0\,. \tag{1.12}$$

In figure 1.3a, it can be seen that detuning the seed frequency will lead to a WVM because of different refractive indices in seed and idler. By aligning seed and pump under an angle α, a configuration may be found where the change of the seed's wave vector length is compensated by a corresponding change of the idler wave vector length and angle such that the triangle in figure 1.3b is always nearly closed which corresponds to an almost vanishing WVM. In practice, the WVM is still only vanishing at several

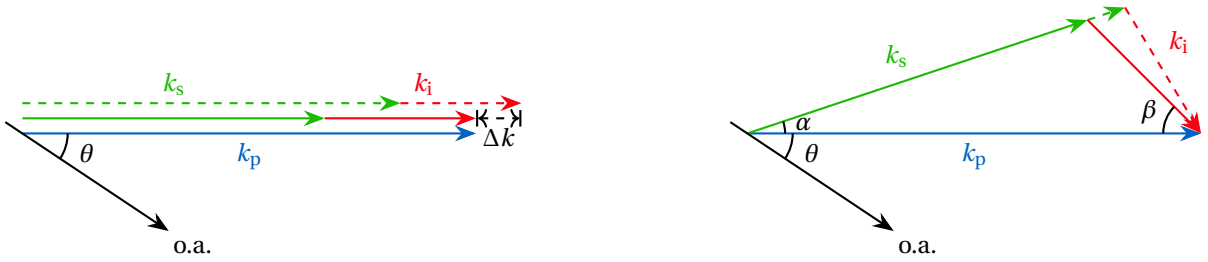

a: Collinear phase matching .

b: Noncollinear phase matching in the PVWC geometry (see below) of a positively birefringent crystal .

Fig. 1.3: Principle of collinear (a) vs. noncollinear (b) phase matching of pump ($\vec{k}_p$), signal ($\vec{k}_s$) and idler ($\vec{k}_i$) in an OPA. Note that in the latter case, more signal wavelengths are phase-matched in contrast to the former case.

distinct wavelengths, but noncollinear phase matching helps to keep it low over a certain bandwidth which is usually much larger than for collinear phase matching and makes a high conversion efficiency possible.

Spatial walk-off

Obviously, noncollinear propagation limits the region where pump and signal pulses are overlapping and interacting. Additionally, the extraordinarily polarized pump beam undergoes so-called birefringent walk-off. As the extraordinary refractive index changes with the crystal angle θ, i.e. the angle between the pump's wave vector and the optical axis, the pump beam direction which is denoted by the Poynting vector $\vec{S}_p$ differs from its wave vector by the so-called birefringent walk-off angle [28]

$$\rho(\theta) = -\frac{1}{n_e}\frac{\mathrm{d}n_e(\theta)}{\mathrm{d}\theta}. \tag{1.13}$$

In other words, the wave vector will point from the origin to the surface of the index ellipsoid whilst the Poynting vector stands perpendicular on it (cf. figure 1.4). An ordinary beam does not undergo this effect because there is no directional dependence of the ordinary refractive index, thus wave vector and Poynting vector point into the same direction.

Depending on the exact geometry, this walk-off can point towards the signal beam direction or in the opposite direction. Experimentally, it can be shown that only the cases when all beams lie in one principal plane [29], i.e. in one plane with the crystal's optical axis, lead to significantly good phase-matching. This yields two possible phase matching geometries: The first is Poynting vector walk-off compensation (PVWC) where α and ρ (partially) compensate each other, cf. figure 1.4a, leading to a longer interaction between pump and seed. The second case is called tangential phase-matching (TPM), cf. figure 1.4b. Here, signal and idler are moving away from the pump beam in different directions which results in a reduced overlap interaction length, lowering the total conversion efficiency. However, especially in areas where signal and pump don't overlap anymore, this makes the idler act as a seed for the signal and vice versa, thus leading to an increased pump depletion and conversion efficiency [30] and thereby partially compensating for the aforementioned reduction in

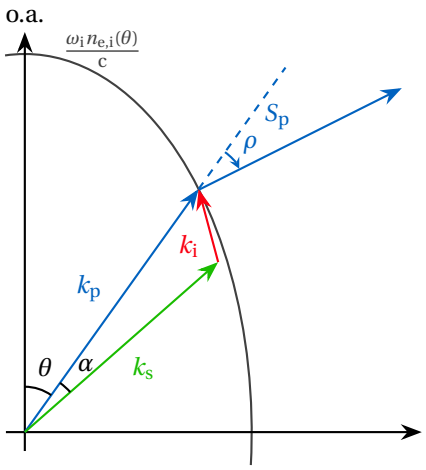

a: In the PVWC geometry, the pump walk-off goes in the same direction as α, increasing the area of spatial overlap upon propagation.
.

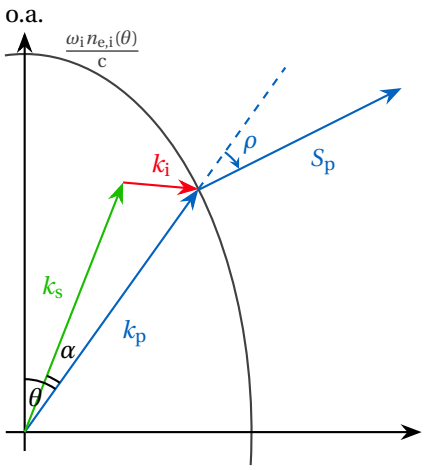

b: In the TPM geometry, seed ($\vec{k}_s$) and idler ($\vec{k}_i$) are propagating away from the pump ($\vec{S}_p$) in different directions leading to continuous co-seeding and suppressed back-conversion .

Fig. 1.4: PVWC vs. TPM geometry in a negatively birefringent crystal. The spatial walk-off ρ of the pump beam results from the pump Poynting vector $\vec{S}_p$ standing perpendicular on the crystal's index ellipsoid.

efficiency. Additionally, in areas where the beams do not overlap, no back-conversion is possible, leading to a potentially broader gain curve [31].

Choosing an appropriate geometry

Based on the principles expounded in the previous sections, first analytical calculations can be made for getting a feeling of suitable noncollinear OPCPA (NOPCPA) geometries. In order to find optimal pairs of crystal crystal angle and nonlinear angle for a given wavelength and to get an idea about the phase-matching bandwidth, energy and momentum conservation (see equations (1.11) and (1.12)) are used for type I phase matching in BBO. Here, signal and idler have ordinary and the pump extraordinary polarization. For the sake of a clear presentation, many dependencies on frequencies are simplified to subscripts corresponding to pump, signal and idler beams. The idler frequency is not a free parameter and always calculated using equation (1.11). In order to get from momentum to frequencies, bear in mind that the wave number in media has the following form:

$$k = \frac{\omega n}{c} = \frac{2\pi n}{\lambda}. \tag{1.14}$$

Noncollinear angle There are two possibilities for obtaining a good phase-matching geometry. One way is to assume a given crystal angle θ and pump frequency ω_p and to find the optimal noncollinear angle α between seed and pump. In a geometry as depicted in figure 1.3b, the ideal noncollinear angle

α_{pm} where the phase mismatch vanishes for a given seed frequency ω_s is calculated by exploiting the law of cosines:

$$k_\mathrm{i}^2 = k_\mathrm{p}^2 + k_\mathrm{s}^2 - 2k_\mathrm{p}k_\mathrm{s}\cos\alpha \tag{1.15}$$

$$\alpha_{\mathrm{pm}}(\omega_\mathrm{p},\omega_\mathrm{s},\theta) = \pm\arccos\left(\frac{\omega_\mathrm{p}^2 n_{\mathrm{e,p}}^2(\theta) + \omega_\mathrm{s}^2 n_{\mathrm{o,s}}^2 - \omega_\mathrm{i}^2 n_{\mathrm{o,i}}^2}{2\omega_\mathrm{p} n_{\mathrm{e,p}}(\theta)\omega_\mathrm{s} n_{\mathrm{o,s}}}\right). \tag{1.16}$$

As the goal is a broadband amplification, the found angle is not necessarily the best angle as the WVM could grow largely for only small frequency differences in the seed. The noncollinear angle yielding the broadest phase-matching bandwidth for a given central wavelength is expected at a geometry where equation (1.15) changes least under a change of k_s. Deriving with respect to k_s requires the relation

$$\frac{\mathrm{d}k_\mathrm{i}}{\mathrm{d}k_\mathrm{s}} = \underbrace{\frac{\mathrm{d}\omega_\mathrm{s}}{\mathrm{d}k_\mathrm{s}}}_{v_{\mathrm{g,s}}} \cdot \underbrace{\frac{\mathrm{d}\omega_\mathrm{i}}{\mathrm{d}\omega_\mathrm{s}}}_{-1} \cdot \underbrace{\frac{\mathrm{d}k_\mathrm{i}}{\mathrm{d}\omega_\mathrm{i}}}_{v_{\mathrm{g,i}}^{-1}} = -\frac{v_{\mathrm{g,s}}}{v_{\mathrm{g,i}}} = -\frac{n_{\mathrm{g,i}}}{n_{\mathrm{g,s}}} \tag{1.17}$$

where the group velocity v_g and group velocity index n_g have been introduced. In principle, they denote the velocity of a wave packet and the corresponding refractive index, cf. equations (A.6) and (A.7). Applying the derivative to the law of cosines yields

$$\alpha_{\mathrm{bw}}(\omega_\mathrm{p},\omega_\mathrm{s},\theta) = \pm\arccos\left(\frac{1}{\omega_\mathrm{p} n_{\mathrm{e,p}}(\theta)} \cdot \left(\frac{n_{\mathrm{g,o,i}}}{n_{\mathrm{g,o,s}}}\omega_\mathrm{i} n_{\mathrm{o,i}} + \omega_\mathrm{s} n_{\mathrm{o,s}}\right)\right). \tag{1.18}$$

Crystal angle It is also possible to go the other way round, albeit more complicated. Starting from a given noncollinear angle α, the angle for vanishing WVM is found by substituting longitudinal momentum conservation and the extraordinary refractive index (A.5) into the transversal momentum conservation. The result is:

$$\begin{aligned}\frac{\cos^2\theta}{n_{\mathrm{o,p}}^2} + \frac{\sin^2\theta}{n_{\mathrm{e}\perp,\mathrm{p}}^2} &= \underbrace{\omega_\mathrm{p}^2\left(\omega_\mathrm{s} n_{\mathrm{o,s}}\cos\alpha + \omega_\mathrm{i} n_{\mathrm{o,i}}\cos\arcsin\left(\frac{\omega_\mathrm{s} n_{\mathrm{o,s}}}{\omega_\mathrm{i} n_{\mathrm{o,i}}}\sin\alpha\right)\right)^{-2}}_{=:A(\omega_\mathrm{p},\omega_\mathrm{s},\alpha)} \\ \Rightarrow \theta_{\mathrm{pm}}(\omega_\mathrm{p},\omega_\mathrm{s},\alpha) &= \pm\arctan\sqrt{\frac{n_{\mathrm{o,p}}^{-2} - A}{A - n_{\mathrm{e}\perp,\mathrm{p}}^{-2}}}.\end{aligned} \tag{1.19}$$

Here, $n_{\mathrm{e}\perp}$ denotes the extraorinary principal value, i.e. the extraordinary refractive index for $\theta = 90°$, cf. appendix A.1. Additionally, by transposing equation (1.18) using equation (A.5), the crystal angle for broadest phase-matching can be found:

$$\begin{aligned}\frac{\cos^2\theta_{\mathrm{bw}}}{n_{\mathrm{o,p}}^2} + \frac{\sin^2\theta_{\mathrm{bw}}}{n_{\mathrm{e}\perp,\mathrm{p}}^2} &= \underbrace{\omega_\mathrm{p}^2\left(\frac{n_{\mathrm{g,o,i}}}{n_{\mathrm{g,o,s}}}\omega_\mathrm{i} n_{\mathrm{o,i}} + \omega_\mathrm{s} n_{\mathrm{o,s}}\right)^{-2}\cos^2\alpha}_{=:B(\omega_\mathrm{p},\omega_\mathrm{s},\alpha)} \\ \Rightarrow \theta_{\mathrm{bw}}(\omega_\mathrm{p},\omega_\mathrm{s},\alpha) &= \pm\arctan\sqrt{\frac{n_{\mathrm{o,p}}^{-2} - B}{B - n_{\mathrm{e}\perp,\mathrm{p}}^{-2}}}.\end{aligned} \tag{1.20}$$

Noncollinear WVM For situations of imperfect phase matching, the non-vanishing WVM is computed as follows, assuming a vanishing transversal component:

$$\Delta k = \Delta k_{\parallel} = \frac{1}{c}\left[\omega_\mathrm{p} n_\mathrm{e,p}(\theta) - \omega_\mathrm{s}\cos(\alpha) n_\mathrm{o,s} - (\omega_\mathrm{p}-\omega_\mathrm{s}) n_\mathrm{o}(\omega_\mathrm{p}-\omega_\mathrm{s})\sqrt{1-\frac{\omega_\mathrm{s}^2 n_\mathrm{o,s}^2 \sin^2(\alpha)}{(\omega_\mathrm{p}-\omega_\mathrm{s})^2 n_\mathrm{o}^2(\omega_\mathrm{p}-\omega_\mathrm{s})}}\right]. \quad (1.21)$$

Parasitic second harmonic generation (SHG) Besides the OPCPA process, parasitic SHG of type I could appear, competing with the OPA process. From equations (1.6) and (A.5) the phase-matching condition for this unwanted process follows as

$$\theta_\mathrm{pm,SHG}(\omega_\mathrm{s}) = \arctan\sqrt{\frac{n_\mathrm{o}(2\omega_\mathrm{s})^{-2} - n_\mathrm{o}(\omega_\mathrm{s})^{-2}}{n_\mathrm{o}(\omega_\mathrm{s})^{-2} - n_{\mathrm{e}\perp}(2\omega_\mathrm{s})^{-2}}}. \quad (1.22)$$

Keeping the definitions above, SHG will occur at an angle $\alpha_\mathrm{SHG} = \theta_\mathrm{pm,SHG} - \theta$, respectively $\theta_\mathrm{SHG} = \theta_\mathrm{pm,SHG} - \alpha$.

1.2.3 Evolution of the electromagnetic fields

While phase-matching is essential and sets the limits of achievable efficiency, the magnitude is largely influenced by involved field strengths, respectively intensities. In the slowly varying envelope approximation (SVEA), the evolution of the complex field envelopes of pump, signal and idler is described by three coupled differential equations [32, 33]:

$$\frac{\partial E_\mathrm{p}}{\partial z} = -\mathrm{i}\frac{\omega_\mathrm{p}}{n_\mathrm{p} c} d_\mathrm{eff} E_\mathrm{s} E_\mathrm{i} \mathrm{e}^{\mathrm{i}\Delta k z} \quad (1.23a)$$

$$\frac{\partial E_\mathrm{s}}{\partial z} = -\mathrm{i}\frac{\omega_\mathrm{p}}{n_\mathrm{s} c} d_\mathrm{eff} E_\mathrm{p} E_\mathrm{i}^* \mathrm{e}^{-\mathrm{i}\Delta k z} \quad (1.23b)$$

$$\frac{\partial E_\mathrm{i}}{\partial z} = -\mathrm{i}\frac{\omega_\mathrm{p}}{n_\mathrm{i} c} d_\mathrm{eff} E_\mathrm{p} E_\mathrm{s}^* \mathrm{e}^{-\mathrm{i}\Delta k z}. \quad (1.23c)$$

They show that the presence of all three fields, i.e. a sufficient spatial and temporal overlap, is needed for an efficient conversion. In addition to this spatio-temporal requirement, the overall parametric gain G is estimated when assuming flat-top temporal and spatial pulse profiles [18, 34]:

$$G = 1 + (gL)^2 \frac{\sinh^2\sqrt{(gL)^2 - (\Delta k L/2)^2}}{(gL)^2 - (\Delta k L/2)^2} \quad (1.24a)$$

$$g = 4\pi d_\mathrm{eff}\sqrt{\frac{I_\mathrm{p}(0)}{2\varepsilon_0 n_\mathrm{p} n_\mathrm{s} n_\mathrm{i} \mathrm{c} \lambda_\mathrm{s} \lambda_\mathrm{i}}}. \quad (1.24b)$$

For small intensities, this yields the approximation of equation (1.7).

A consideration of the imaginary parts in equation (1.23) provides information on the phases, in particular a very simple equation for the idler phase [32, 33]:

$$\phi_\mathrm{i}(z) = \phi_\mathrm{p}(0) - \phi_\mathrm{s}(0) - \frac{\pi}{2} - \frac{\Delta k z}{2}. \quad (1.25)$$

Thusly, the phase accordingly depends only on the difference of the input phases if the WVM is constant. The importance of this phase will be outlined in the following section.

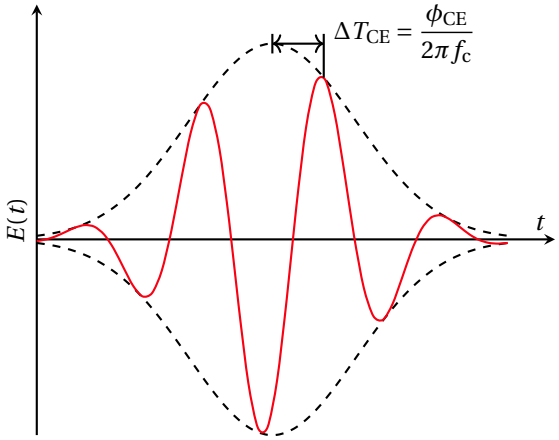

Fig. 1.5: A few-cycle pulse with a carrier frequency f_c, CEP ϕ_{CE} and a Gaussian envelope.

1.3 Carrier-envelope phase stability

The experiments performed in the Veisz group exploit highly nonlinear processes that have a significant dependence directly on the electric field and not only on the intensity respectively amplitude. Here, the carrier-envelope phase (CEP) of a few-cycle laser pulse becomes very important. Especially, the process of high harmonic generation (HHG) is highly affected.

Obviously, it is desirable to fully control or to stabilize the phase. Even if this is not possible, a characterization of the CEP stability for every laser shot is useful. Later, the results of this observation yield deeper insight in electric field dependence of various experiments when combined with single-shot experimental observables.

1.3.1 Carrier-envelope phase and Carrier-envelope offset

The CEP ϕ_{CE} can be understood as the phase corresponding to the time difference ΔT_{CE} between the maximum of the amplitude envelope and the closest maximum of the carrier oscillation as shown in figure 1.5. For an assessment of a system's CEP stability, a measurement of the variation of the carrier-envelope offset (CEO), i.e. the slip of the CEP between two pulses, is practical. It can be derived from the fringe positions obtained by an interferometric measurement between two consecutive pulses [35].

In an oscillator, this offset is built up due to the difference of group and phase velocity in the dispersive elements in the cavity leading to a group-phase offset (GPO) of

$$\Delta\phi_{GPO} = \frac{2\pi}{\lambda}\int_0^L \left(n_g(z) - n(z)\right) \mathrm{d}z = \frac{\omega^2}{c}\int_0^L \frac{\mathrm{d}n(z)}{\mathrm{d}\omega}\,\mathrm{d}z \tag{1.26}$$

where L is the length of one round-trip in the cavity and z is the coordinate following the beam path. The CEO of two subsequently outcoupled pulses amounts to [36]

$$\Delta\phi_{CEO} = \Delta\phi_{GPO} \mod 2\pi\,. \tag{1.27}$$

Additionally to this static offset, predominantly fluctuations of pulse energy and roundtrip time directly add variations to the GPO and thereby the CEO. The first one is coupled to the phase via the Kerr effect while the latter one via dispersion in the beam path (mainly air), namely the group delay dispersion (GDD) [35]. Outside the cavity, however, only the temporal derivative of such fluctuations plays a role as two subsequent pulses outside of the oscillator undergo the same GPO evolution in the absence of fluctuations or drifts [36].

1.3.2 Measuring the CEO of a pulse train

Complementary to the temporal description, a consideration in the frequency domain reveals a convenient method to measure the CEO. The Fourier transform of an equally-spaced train of Gaussian pulses is a frequency comb with a Gaussian envelope:

$$\begin{aligned} E(t) &= \cos(\omega_\mathrm{c} t)\cdot\left\{\exp\left[-2\ln 2\left(\frac{t}{\Delta\tau}\right)^2\right]\star\sum_{m=-\infty}^{\infty}\delta\left(t-\frac{m}{f_\mathrm{rep}}\right)\right\} \\ \xrightarrow{\mathrm{FT}}\ \tilde{E}^+(\omega) &= \pi\sqrt{\frac{\pi}{2\ln 2}}\Delta\tau\omega_\mathrm{rep}\cdot\exp\left[-\frac{\Delta\tau^2}{8\ln 2}(\omega-\omega_\mathrm{c})^2\right]\cdot\sum_{m=-\infty}^{\infty}\delta\left(\omega-\omega_\mathrm{c}-m\omega_\mathrm{rep}\right). \end{aligned} \tag{1.28}$$

Here, the star $\star$ denotes a convolution. Note that in general only the spectral parts with positive frequencies are considered as they correspond to a measurable spectrum. This electric field in the spectral domain is denoted by $\tilde{E}^+$. In order to get back to the original expression in the time domain, the real part of the back transform of $\tilde{E}^+$ is taken. Any equidistant pulse train as the above described will have a CEO of $\Delta\phi_\mathrm{CEO} = 2\pi f_\mathrm{c} f_\mathrm{rep}^{-1} \mod 2\pi$. Consequently, the spectrum will consist of a comb of equidistant frequencies

$$f_k = f_\mathrm{CEO} + k\cdot f_\mathrm{rep}\,,\ k\in\mathbb{N}_0 \tag{1.29}$$

spaced by the repetition rate $\frac{\omega_\mathrm{rep}}{2\pi} = f_\mathrm{rep} = T_\mathrm{R}^{-1}$ with an offset of $f_\mathrm{CEO} = \frac{\Delta\phi_\mathrm{CEO}}{2\pi} f_\mathrm{rep} = f_\mathrm{c} - \ell f_\mathrm{rep}$ where $\ell = \lfloor\frac{f_\mathrm{c}}{f_\mathrm{rep}}\rfloor$ [37] or accordingly $\omega_\mathrm{CEO} = 2\pi f_\mathrm{CEO}$, cf. figure 1.6.

Provided that the spectrum has a sufficiently large bandwidth $\Delta f/f = 2\frac{m-n}{m+n}$, beating of the mth harmonic $f_m = m f_\mathrm{CEO} + m k_m f_\mathrm{rep}$ of a frequency line and the nth harmonic $f_n = n f_\mathrm{CEO} + n k_n f_\mathrm{rep}$ of another yields

$$f_\mathrm{beat} = f_m - f_n = (m-n) f_\mathrm{CEO}\,, \tag{1.30}$$

if $m k_m = n k_n$.

Often used is the so-called f-$2f$ approach, where $(m,n) = (2,1)$ and the second harmonic is created in a nonlinear crystal. If the spectrum does not span the necessary octave ($\Delta f/f = \frac{2}{3}$) it is usually broadened exploiting SPM and other nonlinear effects in nonlinear bulk media or photonic crystal fibers (PCFs). Also a $2f$-$3f$ approach is possibly efficient enough, especially when the spectrum already spans more than two-thirds of an octave. Here, the second harmonic is beaten with the third harmonic created by subsequent sum-frequency generation (SFG).

An alternative requiring an octave-spanning spectrum is 0-f, where the difference frequency $f_\mathrm{DF} = (k_\mathrm{high} f_\mathrm{rep} + f_\mathrm{c}) - (k_\mathrm{low} f_\mathrm{rep} + f_\mathrm{c}) = (k_\mathrm{high} - k_\mathrm{low}) f_\mathrm{rep}$ of the high and low ends of the spectrum is generated and afterwards combined with the low-frequency end of the fundamental pulse in a heterodyne measurement and yielding a beat frequency $f_\mathrm{beat} = f_\mathrm{CEO}$ [38].

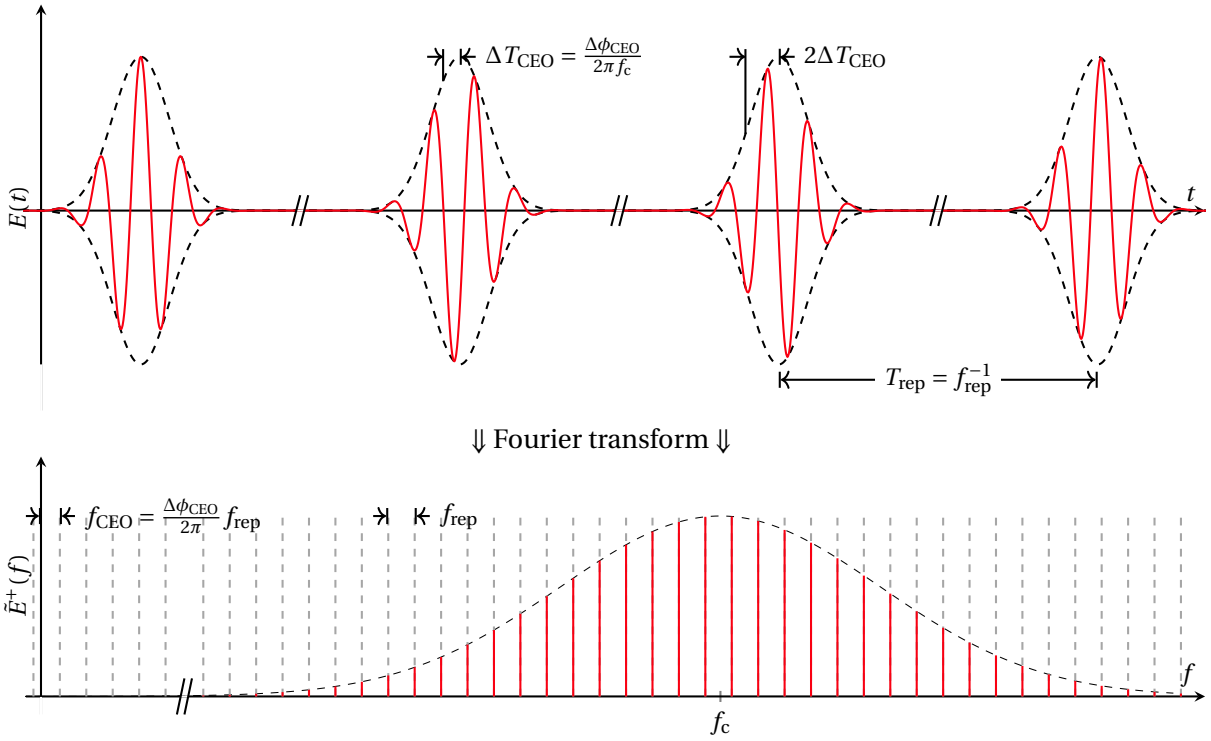

Fig. 1.6: A pulse train in the time domain is a frequency comb in the frequency domain.

1.3.3 Single-shot CEO measurement

If the repetition rate is too low, it is difficult to determine the CEO as described above. Here, it is exploited that the CEP is encoded into the phase of the spectral representation of the electric field:

$$\begin{aligned} E(t) &= \cos\left(\omega_c t - \phi_{\mathrm{CE}}\right) \cdot \exp\left[-2\ln 2\left(\frac{t}{\Delta\tau}\right)^2\right] \\ \xrightarrow{\mathrm{FT}} \tilde{E}^+(\omega) &= \pi\sqrt{\frac{\pi}{2\ln 2}}\Delta\tau \cdot \mathrm{e}^{-\mathrm{i}\phi_{\mathrm{CE}}} \exp\left[-\frac{\Delta\tau^2}{8\ln 2}(\omega-\omega_c)^2\right] =: \mathrm{e}^{-i\phi_{\mathrm{CE}}}\tilde{E}'(\omega)\,. \end{aligned} \tag{1.31}$$

The creation of harmonics due to the nonlinear polarization gives the chance to perform a spectral interferometry (SI) measurement by replacing the photo diode in the interferometric setups described above by a spectrometer. For example, when using an f-$2f$ interferometer, the phase of the second harmonic will be doubled due to the quadratic dependence of a crystal's polarization $P^{(2)}$ on the electric field, assuming an instant response of the nonlinear medium:

$$\tilde{P}^{(2)}(\omega) = \chi \int_{-\infty}^{\infty} \tilde{E}^+(\omega')\tilde{E}^+(\omega-\omega')\,\mathrm{d}\omega' \tag{1.32}$$

$$= \mathrm{e}^{-\mathrm{i}2\phi_{\mathrm{CE}}}\chi \int_{-\infty}^{\infty} \tilde{E}'(\omega')\tilde{E}'(\omega-\omega')\,\mathrm{d}\omega'\,, \tag{1.33}$$

$$\tilde{E}_{\mathrm{SH}}(\omega) \propto \mathrm{e}^{\mathrm{i}\pi/2}\tilde{P}^{(2)}(\omega) \tag{1.34}$$

where the phase shift of $\frac{\pi}{2}$ occurs under second harmonic generation assuming perfect phase matching [32]. This principle was first proposed by Mehendale et al. using the interference of second and

third harmonic [39] and first used by Kakehata et al. using a linear common-path interferometer [40]. The interferogram

$$I_{\mathrm{SI}}(\omega) \propto I_{\mathrm{FF}}(\omega) + I_{\mathrm{SH}}(\omega) + 2\sqrt{I_{\mathrm{FF}}(\omega) I_{\mathrm{SH}}(\omega)} \cos\left(\omega\tau + \phi_{\mathrm{CE}} - \phi_{\mathrm{const}}\right) \tag{1.35}$$

where τ is the time delay between the blue component (I_{FF}) and the second harmonic of the red component interfering with each other and $\phi_{\mathrm{const}} = \frac{\pi}{2}$ under idealized conditions (see above) but shifted due to linear dispersion[41]. The delay determines the modulation period of the spectrum and has to be chosen both small enough to be able to spectrally resolve the modulation and sufficiently large to observe several fringes. Here, a spectrally constant delay $\tau_{\mathrm{i}} \equiv \tau_0$ introduced by a delay line (case i) and a varying delay $\tau_{\mathrm{ii}} = \tau(\omega)$ resp. $\tau_{\mathrm{ii}} = \tau(\lambda)$ (case ii) have very different effects as the following consideration reveals. Over the spectral overlap region of the fundamental and its second harmonic, it is justifiable to approximate the introduced delay to the first order. $\tau(\lambda) \simeq \tau_0 + (\lambda - \lambda_0) a_\tau$. The cosine part of equation (1.35) then looks like

$$I_{\mathrm{ii}} \sim \cos\left(\frac{2\pi \mathrm{c}}{\lambda}\tau_0 + \frac{2\pi \mathrm{c}}{\lambda}\lambda a_\tau - \frac{2\pi \mathrm{c}}{\lambda}\lambda_0 a_\tau + \phi\right) \tag{1.36}$$

$$= \cos\left(\frac{2\pi \mathrm{c}}{\lambda}\underbrace{(\tau_0 - \lambda_0 a_\tau)}_{=:\tau_{0,\mathrm{ii}}} + \underbrace{2\pi \mathrm{c} a_\tau + \phi}_{=:\phi_{\mathrm{ii}}}\right). \tag{1.37}$$

So even though $I_{\mathrm{i}}(\lambda_0) = I_{\mathrm{ii}}(\lambda_0)$, the fringe periods are completely different, not to mention the phase shift $\phi_{\mathrm{ii}} - \phi$.

Since ϕ_{const} is unknown, it is only possible to determine the relative evolution of the CEP between pulses by comparing the fringe positions.

2 | LWS-20 laser system

In the Veisz group, at the Laboratory for Attosecond and High-Field Physics (LAP), three experimental setups have been built up over the past few years: High-harmonic generation in gases as well as on solids and electron acceleration. The goal to investigate ultrafast relativistic processes requires both, high energy and very short pulses. In order to achieve these, the LWS-20 laser system has been developed. Its heart is a four-stage two-color pumped noncollinear optical parametric chirped-pulse amplifier (NOPCPA) operating at a repetition rate of 10 Hz and delivering broadband pulses with energies up to 80 mJ spanning from 580 nm to 1020 nm which makes it possible to achieve peak powers of nearly 20 TW. This is unique in the world and reflected by the name of the laser system: Light Wave Synthesizer 20 (LWS-20). As the work undergone in the scope of this thesis focuses on the examination and further development of the laser system, the current system is described in this chapter. The layout is outlined in figure 2.1.

2.1 kHz front-end

The front-end provides the short and broadband pulses that will be amplified later. It is built around a commercial system (Femtopower Compact Pro by Femtolasers GmbH) which employs a Ti:Sapphire oscillator yielding few-nJ 8 fs pulses at a repetition rate of 80 MHz. The major part of the out-coupled energy is stretched and amplified in a multi-pass amplifier passing through a Pockels at the fourth pass cell with 1 kHz. After the subsequent prism compressor, the pulses delivered by the Femtopower have a length of around 20 fs and an energy of 800 µJ.

Now, the pulses are broadened by self-phase modulation (SPM) in a neon-filled hollow-core fiber (HCF) giving 350 µJ pulses with a transform limit (TL) of 4 fs. Optionally, the pulses are sent through a chirped-mirror compressor and cross-polarized wave generation (XPW) for temporal contrast enhancement with an overall efficiency of typically less than 10 %, on an experimental day usually around 5 %. If energy is more important than the contrast, the compressor and XPW are bypassed. Recently, the contrast enhancement has been used for all experiments.

The pulses are then stretched to 100 ps in a negative-dispersion grism stretcher which has been replaced recently [42, 43]. An acousto-optic programmable dispersive filter (AOPDF) (Dazzler, Fastlite) is used to reduce the residual phase. It works at a repetition rate of 10 Hz and compresses the pulses to 67 ps, yielding an input to the NOPCPA of 1 µJ to 3 µJ when operated without XPW.

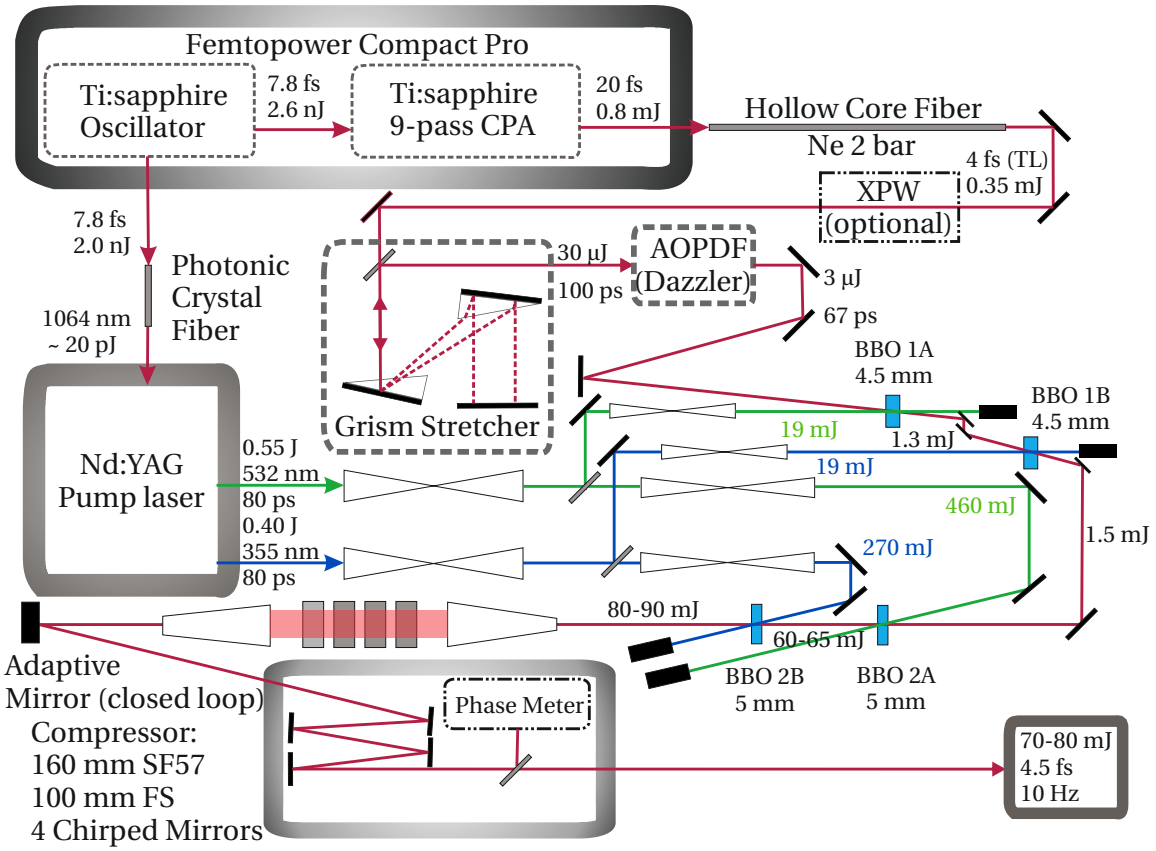

Fig. 2.1: Layout of the LWS-20 laser system. Courtesy of Laszlo Veisz and Daniel Rivas.

2.2 Noncollinear OPCPA

The thus created pulses seed the optical parametric synthesizer (OPS) which, as mentioned above, consists of four NOPCPA stages pumped by green ($\lambda = 532\,\text{nm}$, stages 1A, 2A) and blue ($\lambda = 355\,\text{nm}$, stages 1B, 2B) laser light.

The reason for two-color pumping is directly connected to phase matching: the phase-matching range for the optical parametric amplification (OPA) process for the short-wavelength part of the spectrum when using the green pump or conversely, for the long-wavelength part when using the blue pump, is very narrow. Additionally, the first case would result in a very long-wavelength idler undergoing significant absorption [23]. This would lead to strongly reduced conversion efficiency as visible in equation (1.23).

Pump laser In order to synchronize pump and seed, the pump laser is seeded by the remaining oscillator output that has not been sent into the multipass amplifier (optical synchronization). The pulses are shifted to a central wavelength of 1064 nm using a photonic crystal fiber (PCF), pre-amplified in a fiber amplifier and then used as a seed of a flash-lamp pumped Nd:YAG laser system (Ekspla). It

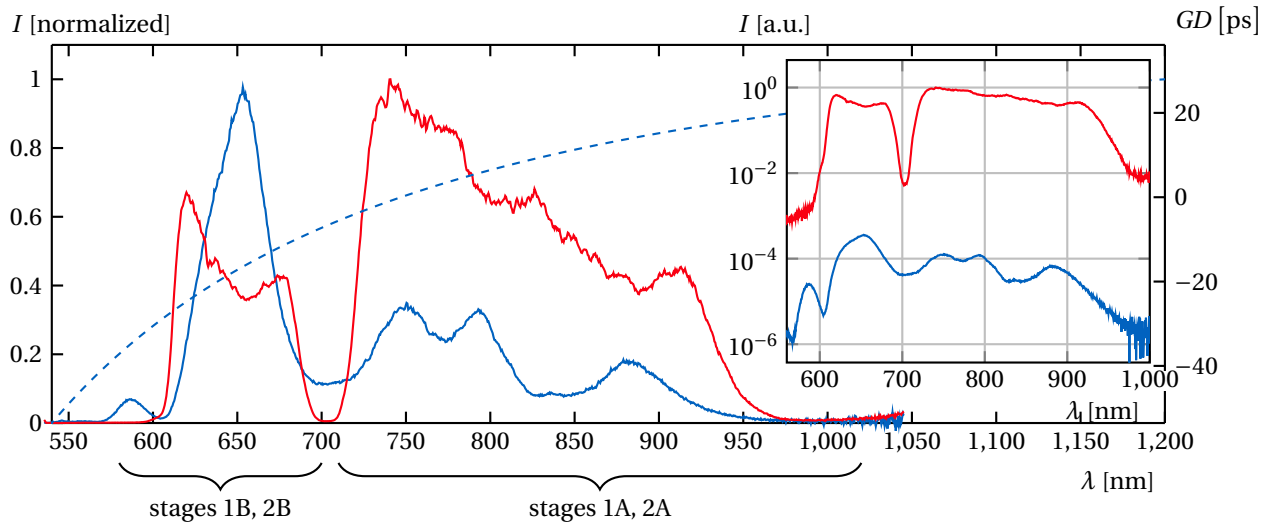

Fig. 2.2: Normalized measured output spectrum XPW (solid blue, 14 µJ) and full NOPCPA (solid red, 68 mJ) with calculated input group delay (dashed blue). Both spectra were acquired from scattered light of white paper. Inset: XPW intensity scaled by energy ratio. Note that the optical parametric chirped-pulse amplification (OPCPA) input is 1-2 orders of magnitude smaller than the XPW output, so the gain is higher by the same amount in reality.

delivers two separate beams of 80 ps pulses with an energy of one joule each. One beam is frequency-doubled to $\lambda = 532\,\text{nm}$ and split into parts of 19 mJ for stage 1A and 460 mJ for stage 2A, the other one is frequency-tripled to $\lambda = 355\,\text{nm}$ and split into 19 mJ pulses for stage 1B and 270 mJ pulses for stage 2B. All beams are relay imaged on the beta barium borate (BBO) crystals in order to provide a good spatial beam profile [44] and overlapped temporally and spatially with the seed beams.

Amplification The seed passes through the stages in the order 1A, 1B, 2A, 2B where the green-pumped A stages amplify the long-wavelength part from 700 nm to 1020 nm and the B blue-stages the short-wavelength part from 580 nm to 700 nm. A typical XPW spectrum is displayed in figure 2.2 together with a typical overall output spectrum of the NOPCPA. The gain is larger than suggested in the inset as between XPW and the first OPCPA stage, the beam is weakened by more than one order of magnitude, mainly due to losses in the AOPDF and the stretcher [43]. This is compensated in the simulations by defining a lower input energy of 150 nJ. It should be mentioned that the beam is not weakened uniformly in reality, leading to a distorted seed spectrum. However, the spectrum does still allow for meaningful simulations.

The group delay of the input pulse after the stretcher and the AOPDF represented by the dashed line in figure 2.2 has been calculated in accordance with [43] backwards from a theoretical fully-compressed pulse by taking into account the dispersion of the compressor and the BBO crystals in the NOPCPA system, cf. equations (A.10) and (A.15). The higher-order phases (cf. equations (A.11) to (A.14)) for $\lambda_c = 747\,\text{nm}$ are $GDD = 40\,638\,\text{fs}^2$, $TOD = 25\,709\,\text{fs}^3$, $FOD = 10\,552\,\text{fs}^4$ and $FID = 16\,081\,\text{fs}^5$. The change of the phase caused by the OPCPA process as described in [33, 34] was assumed to be negligible compared to the huge group delay dispersion (GDD) added by the stretcher.

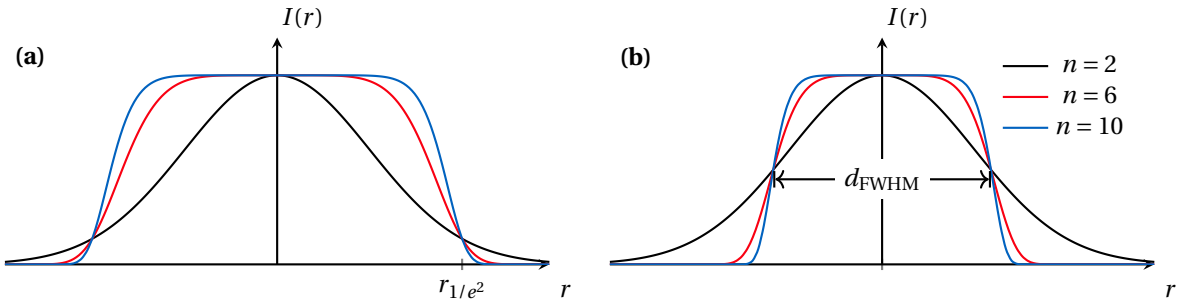

Fig. 2.3: Super-Gaussians of order 2 (normal Gaussian), 6 and 10 as defined by equation (2.1a) with the same r_{1/e^2} (a) and FWHM (b), respectively.

Albeit providing a broader amplification range, two-color pumping leads to a gap between the spectral parts amplified in the A stages and those in the B stage.

Spatial beam profiles The seed has a Gaussian beam profile ($n = 2$) in time and space, the pump has a Gaussian temporal envelope and a super-Gaussian of order $n = 6$ (stages 1A, 1B) or $n = 10$ (stages 2A, 2B). The intensity distribution with a full width at half maximum (FWHM) diameter d_{FWHM} is

$$I_n(r) = I_0 \exp\left[-2\frac{r^n}{r_{1/\mathrm{e}^2}^n}\right] \tag{2.1a}$$

$$r_{1/\mathrm{e}^2} = \frac{d_{\mathrm{FWHM}}}{\sqrt[n]{2^{n-1}\ln 2}}. \tag{2.1b}$$

As figure 2.3 shows, the use of pulses with such a beam profile has the advantage of a more uniform intensity distribution, reducing gain guiding [45] and increasing the overall gain.

For a better overview, the important system parameters are summarized in table 2.1. Remember that the crystal cut angle θ_{cut} is not the effective θ since the crystals are experimentally tilted and thereby adjusted for best results. The signal beam is expanded before stage 2A. Values for the signal radius in B stages are omitted here since they depend largely on the pump diameter of the preceding stage.

The pump radii were determined by fitting line-outs of spatial intensity measurements with a camera. The measurement for stage 1A is assumed to be erratic because a similar peak intensity as the $13\,\mathrm{GW\cdot cm^{-2}}$ reported in [46] is expected. When calculating the peak intensity I_0 using equation (2.1a) and assuming a (second-order) Gaussian temporal envelope, this would result only in a peak intensity $I_0 = 4.45\,\mathrm{GW\cdot cm^{-2}}$. This assumption is backed by measurements with a burn paper that show only a radius $r_{\mathrm{p,1A}} = 1.23\,\mathrm{mm}$. However, this pump size would still only result in half of the referenced peak intensity. For the simulations, a rough radius scan resulted in an output energy comparable to the experiment when choosing $r_{\mathrm{p,1A}} = 0.75\,\mathrm{mm}$. Likewise, the pump radius for 1B was chosen as $r_{\mathrm{p,1A}} = 0.75\,\mathrm{mm}$.

Compression The output pulses with an energy of around 80 mJ to 90 mJ are spatially expanded and compressed in bulk blocks of 160 mm SF57 glass and 160 mm fused silica (FS) to 200 fs. A deformable mirror in interplay with a wavefront sensor cleans the wavefront and the final compression is done in

stage	crystal		pump				seed	
	dim [mm^3]	θ_{cut} [°]	λ [nm]	r_{1/e^2} [mm]	τ_{FL} [ps]	W [mJ]	r_{1/e^2} [mm]	α [°]
1A	$7 \times 7 \times 4.5$	24	532	1.5[1]	80	19	1.5	−2.23
1B	$5 \times 5 \times 4.5$	34.55	355	1.5[2]	80	19		−3.40
2A	$23 \times 23 \times 5$	23.83	532	5.3	80	460	7.5	−2.23
2B	$15 \times 15 \times 5$	34.55	355	6	80	270		−3.40

Tab. 2.1: Parameters of the OPCPA stages. The negative sign of the noncollinear signal angle α arises from the tangential phase-matching (TPM) phase-matching geometry and the convention used in section 1.2.2.

vacuum by four chirped mirrors. A small portion of the beam is sent to a single-shot mini-stereo-ATI phase meter [47] for performing carrier-envelope phase (CEP) tagging.

In the end, the pulses are sent to the different beamlines where the experiments are performed.

[1] This value is assumed to be erratic, see the description in the text. The value used for the simulations is 0.75 mm.
[2] The value used for the simulations is 1.2 mm.

3 | NOPCPA simulations

The considerations and calculations so far disregard any other nonlinear processes and give only an estimate of magnitudes. Additionally, they do not take any propagation effects into account at all. In reality, these play an important role, especially for strong pulses and thick crystals. In order to get a more realistic idea, simulations of the optical parametric chirped-pulse amplification (OPCPA) stages have been performed. This allows to understand ongoing processes better and is a useful tool for investigating possible improvements of the system.

After describing the software used for simulations (section 3.1) the right parameters for the simulations are determined consistent with section 2.2. Then, the consequences of reducing the pump radius on a gain increase and other occurring effects are examined as well as the prospects of adding other crystals to increase the degrees of freedom for phase matching.

3.1 Simulation principle

The software `chi2D` written by Tino Lang has been used for extensive simulations of use-cases for the LWS-20 OPCPA system. It is based on a $(2+1)$-dimensional split-step algorithm which includes all second-order processes, as well as self-phase modulation (SPM). In the following, the most important features and principles are explained briefly. For more details, please refer to the original publication [31] and his PhD thesis [30].

Pulse propagation

For calculating the pulse propagation, two dimensions suffice without neglecting too many spatial effects because walk-off and all propagation directions lie in one principal plane, as mentioned in section 1.2.2. The main propagation direction lying under an angle ϑ with the optical axis will be denoted by z and the other direction within the principal plane by x. In the conducted simulations in this thesis, the pump wave vector is always set to lie initially on the z axis, such that $\alpha_{\mathrm{p,e}}(z=0)=0$ and $\vartheta=\theta$.

There is no beam separation in the orthogonal y direction and even diffraction is negligible within the Rayleigh length in that direction which is satisfied due to the large beam sizes in the LWS-20. For the propagation in z-direction, the paraxial wave equation is used under the slowly varying envelope approximation (SVEA) in longitudinal direction following the approach of Fleck et al. [48, 49]. The

SVEA implies that there is no big change of electric field during propagation over a wavelength. The complex waves are represented as a superposition of plane waves with spatial frequencies ν_x and $\nu_y \approx 0$ and $\lambda = \frac{\mathrm{c}}{n_{\mathrm{o,e}} f}$. Then, the accumulated phase is $\mathrm{e}^{ik_z z}$ with $k_z^2 \approx k^2 - k_x^2$. With the aforementioned restrictions, the electric field evolution for ordinary and extraordinary polarization can be treated separately in the Fourier domain for one propagation step $\mathrm{d}z$:

$$E_{\mathrm{o,e}}(f,\nu_x,z+\mathrm{d}z) = E_{\mathrm{o,e}}(f,\nu_x,z)\exp\left[\mathrm{i}\underbrace{\sqrt{\left(\frac{2\pi f}{c}n_{\mathrm{o,e}}(f,\nu_x)\right)^2-(2\pi\nu_x)^2}}_{k_z}\mathrm{d}z\right] \tag{3.1}$$

using equations (A.4) and (A.5) for the refractive index. This implements dispersion, walk-off and diffraction. The angle of propagation relative to z, $\alpha_{\mathrm{o,e}}$, is linked to the corresponding spatial frequencies by the first-order grating equation:

$$\alpha_{\mathrm{o}} = \arcsin\left(\frac{\nu_x\lambda_0}{n_{\mathrm{o}}}\right) = \arcsin\left(\frac{\nu_x \mathrm{c}}{f n_{\mathrm{o}}}\right) \tag{3.2a}$$

$$\alpha_{\mathrm{e}}(f,\nu_x,n_{\mathrm{e}}) = \arcsin\left(\frac{\nu_x}{f}\frac{\mathrm{c}}{n_{\mathrm{e}}(f,\vartheta+\alpha_{\mathrm{e}})}\right). \tag{3.2b}$$

As the employed extraordinary refractive index changes with the angle, the angle is approximated using an iterative algorithm.

Frequency mixing

Contrary to the usual approach of treating every second-order process and each of the three involved fields separately as in equation (1.23), all second-order processes are included in two coupled differential equations, as depicted in figure 3.1:

$$\partial_z E_{\mathrm{o}}(t,x) = -\mathrm{i}\kappa_{\mathrm{o}}(\overbrace{\underbrace{E_{\mathrm{e}}E_{\mathrm{e}}}_{\text{ee-o}}+\underbrace{2E_{\mathrm{e}}E_{\mathrm{o}}^*}_{\text{oo-e}}}^{\text{Type I}}+\overbrace{\underbrace{2E_{\mathrm{e}}E_{\mathrm{e}}^*}_{\text{eo-e}}+\underbrace{2E_{\mathrm{e}}E_{\mathrm{o}}+2E_{\mathrm{o}}E_{\mathrm{e}}^*}_{\text{eo-o}}}^{\text{Type II}}) \tag{3.3a}$$

$$\partial_z E_{\mathrm{e}}(t,x) = -\mathrm{i}\kappa_{\mathrm{e}}(\underbrace{E_{\mathrm{o}}E_{\mathrm{o}}}_{\text{oo-e}}+\underbrace{2E_{\mathrm{o}}E_{\mathrm{e}}^*}_{\text{ee-o}}+\underbrace{2E_{\mathrm{o}}E_{\mathrm{o}}^*}_{\text{eo-o}}+\underbrace{2E_{\mathrm{e}}E_{\mathrm{o}}+2E_{\mathrm{e}}E_{\mathrm{o}}^*}_{\text{eo-e}}) \tag{3.3b}$$

where $\kappa_{\mathrm{o,e}}$ is the nonlinear interaction parameter

$$\kappa_{\mathrm{o,e}}(f,\nu_x) = \frac{\pi f d_{\mathrm{eff}}}{n_{\mathrm{o,e}}(f,\nu_x)\mathrm{c}} \tag{3.4}$$

and is calculated in the Fourier domain. d_{eff} is approximated as constant for all processes and wavelengths.

Besides the second-order processes which are all included in equations (3.3), SPM is optionally implemented by using the intensity $I = 2\varepsilon_0 \mathrm{c} n_{\mathrm{o,e}}(f,\nu_x)\,\mathrm{FT}\{|E(t,x)^2|\}$ in equation (1.10) in order to define an SPM parameter

$$\kappa_{\mathrm{SPM}} = 4\pi\varepsilon_0 n_2 n(f,\nu_x) f\,, \tag{3.5}$$

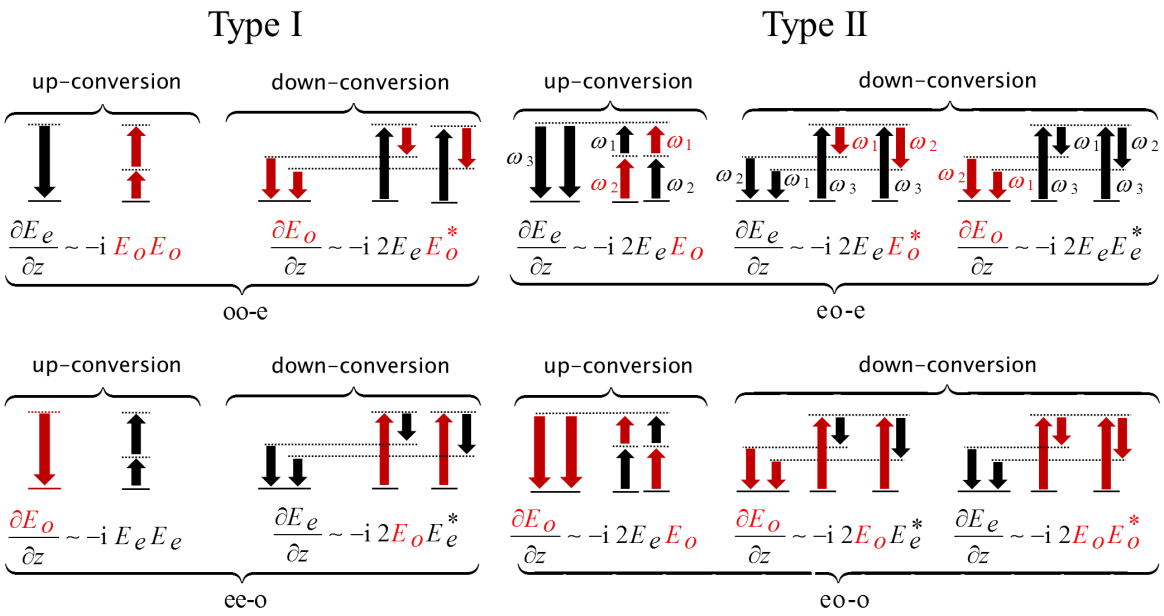

Fig. 3.1: Possible second-order interactions of extraordinary and ordinary light fields. Taken from [30].

and using it equivalently to equations (3.3):

$$E(f, \nu_x, z + \mathrm{d}z) = E(f, \nu_x, z) + \kappa_{\mathrm{SPM}}(f, \nu_x)\, \mathrm{FT}\left\{\mathrm{i}|E(t,x)|^2\, \mathrm{d}z E(x,t)\right\}. \tag{3.6}$$

This also includes the other third-order effects mentioned in section 1.1.4, most notably Kerr lensing.

Implementation

The input is represented by the two orthogonally polarized fields $E_{\mathrm{o,e}}(f, \nu_x, z = 0)$, and the refractive indices $n_{\mathrm{o,e}}(f, \nu_x)$ as well as $\kappa_{\mathrm{o,e}}$ and the transmission $T(f)$ are calculated as starting conditions. In addition to the electric field, a noise field array can be superimposed with approximately one photon per frequency interval and random phase.

The first half-step is performed by solving the propagation equations (3.1) with an explicit Euler algorithm. After a two-dimensional fast Fourier transform (FFT), the changes of the electric fields, $\partial E_{\mathrm{o,e}}(f, \nu_x)$, are calculated using equations (3.3) and undergo a two-dimensional inverse FFT (iFFT). Then, $\kappa_{\mathrm{o,e}}(f, \nu_x)$ for the next step is calculated following equation (3.4) and the frequency mixing is applied to the electric fields: $E = E + \partial E \cdot \kappa$. For the SPM, another computation (equation (3.6)) is necessary.

Now, the next iteration is performed, by starting with the propagation again. The split-step algorithm is depicted in figure 3.2.

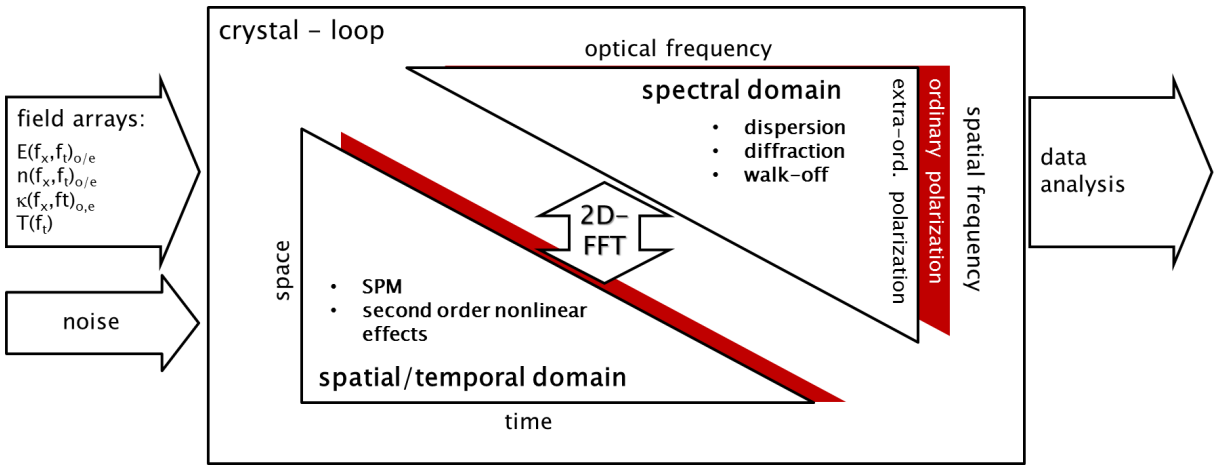

Fig. 3.2: Scheme showing the principle of the split-step code used by `chi2D.exe`. Taken from [30].

3.1.1 Computing ressources

While the software supports CUDA graphics processing units (GPUs) for very fast simulations of low-power OPCPAs, the application on high-power OPCPA stages and longer pulse durations (~ 100 ps) yields some difficulties. The power itself is not the obstacle but the required large beam diameters and long stretching. The spatial grid must span at least the full signal beam and be fine enough to resolve the spatial frequencies corresponding to propagation directions at certain wavelengths. From equation (3.2), the minimum number of transversal pixels for a space windows with the size Δx is determined to be

$$N_{x,\mathrm{min}} = \max_{\{\lambda,\alpha\}} \left\lceil \frac{1}{\lambda} 2\Delta x n_{\mathrm{o,e}}(\lambda) \sin\alpha) \right\rceil , \tag{3.7}$$

i.e. the maximum over all needed combinations of λ and α. The factor 2 results from the necessity to include positive and negative directions. Additionally, there should be enough room for spatial walk-off which is fortunately very small compared to the overall beam size. Likewise, the temporal grid should at least span the signal pulse throughout the whole process in its time window Δt and be fine enough to include the pump wavelength:

$$N_{t,\mathrm{min}} = \left\lceil \frac{\mathrm{c}\Delta t}{\lambda_{\mathrm{p}}} \right\rceil . \tag{3.8}$$

Keep in mind that the restrictions in equations (3.7) and (3.8) don't assure that all kinds of other effects are included in the simulation and may be lost when lying outside the grid. However, this is to be expected almost exclusively for high frequencies as long-wavelength components are automatically included and also the mapped angular range decreases with decreasing wavelengths. For an efficient FFT, the matrices need to have dimensions 2^n, $n \in \mathbb{N}$, blowing them up even more. Consequently, the four matrices $E_{\mathrm{o,e}}(t,x)$, $E_{\mathrm{o,e}}(f,\nu_x)$ are too large for the graphic memory and need to be stored in the RAM. Thus, all calculations need to be done by the CPU, slowing the simulations down extremely. For the simulations, a total of 48 GB of RAM have been installed, still not being enough for the last stage (2B) by virtue of the large beam diameters and the short-wavelength 3ω pump.

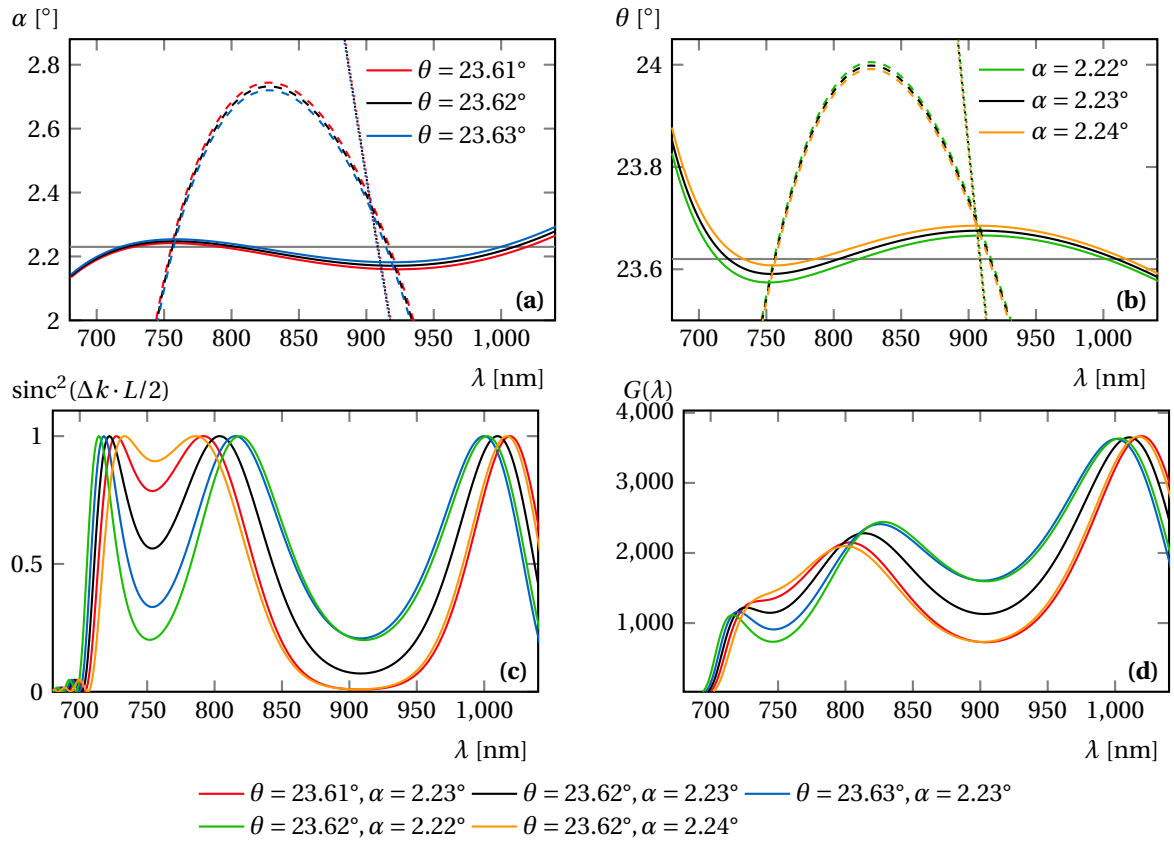

Fig. 3.3: Angular sensitivity of phase-matching in the 1A stage. (a) The optimal noncollinear angle α_{pm} (solid), broad-bandwidth angle α_{bw} (dashed) and SHG angle α_{SHG} (dotted).(b) The optimal crystal angle θ_{pm} (solid), θ_{bw} (dashed) and θ_{SHG} (dotted).(c) The resulting small-intensity gain (normalized) as determined by equations (1.7) and (1.21).(d) Theoretical gain assuming $W_{\mathrm{p}} = 19\,\mathrm{mJ}$, $r_{\mathrm{p}} = 1.5\,\mathrm{mm}$ and a flat-top pump beam, cf. equation (1.24a).

Furthermore, post-analysis was impeded by a problem of saving the large result arrays $E_{\mathrm{o,e}}(f, \nu_x)$ to the hard drive. Especially when using the output as an input for another crystal, much information is lost.

3.2 Suitable NOPCPA geometries

Noncollinear phase-matching varies depending on the material dispersion and is very sensitive even on small angle detuning, thus being referred to as critical phase matching as well. As the noncollinear and especially the crystal angle are difficult to measure with sufficient precision and earlier publications on the LWS-20[46, 50] might have used a different Sellmeier formula, the formulae in section 1.2.2 were used in a `Wolfram Mathematica` notebook using the `Manipulate` functionality. First, the given angles were checked and other promising geometries were used as input parameters for simulations. This approach is valid since experimentally the geometry is tuned for best results. It is also needed as an extensive, multi-dimensional scan in the simulations over a large area with a small step size would be desirable in fact, but it was not possible because of the long computing times (cf. section 3.1.1).

Crystal 1A was chosen as an example for general remarks owing to the focus of this work which lies on the A stages.

3.2.1 Angular sensitivity

Figure 3.3 shows that a slight detuning of 0.01° barely changes the angles for second harmonic generation (SHG) or the angles for locally broadest phase-matching and the angles for perfect phase-matching are changed slightly more, cf. figures 3.3a and 3.3b. However, the WVM changes quite significantly both position and height of the minima in the gain curve (figures 3.3c and 3.3d). Hereby the magnitude of the effect caused by detuning α or θ is comparable and within some limits the phase-matching range can be tuned without big changes on the overall shape of the phase-matching efficiency curve by tuning α and θ together.

In the last plot, the influence of the intensity is visualized which distorts the gain curve towards a maximum above 1000 nm. This is still only an approximation since the pump beam is a sixth-order Gaussian in space and second-order in time. The overall peak intensity was chosen for the plots rather than the average intensity in space and time, which is why the resulting numbers are too high.

An experimental investigation on the angular sensitivity of the LWS-20 can be found in [51]. It was conducted using an old laser setup with just two green-pumped stages but two general results apply also here: Phase matching is very sensitive and the phase matching bandwidth tends to become narrower towards shorter wavelengths. Since both angles were changed independent of each other, actually shifting the whole phase-matching curve was not examined there.

3.2.2 PVWC vs. TPM geometry

In figures 3.3a and 3.3b, only the positive solution of equations (1.16) and (1.18) to (1.20) was plotted although a negative solution exists as well. All solutions are combined in figure 3.4 for both stages using the phase-matching angles θ from [50] ($\theta_{1A,2A} = 23.62°$, $\alpha_{1A,2A} = 2.23°$ and $\theta_{1B,2B} = 34.58°$, $\alpha_{1B,2B} = 3.4°$). Contrarily to the noncollinear angles for optical parametric amplification (OPA), α_{pm} and α_{bw}, the angle for parasitic SHG, α_{SHG} has only one solution which happens to be positive in the amplification wavelength range of the respective stage and is intersecting the curve for the positive noncollinear angle around 900 nm and 630 nm, respectively.

In the following, only the positive solutions will be plotted. Keep in mind, that only the SHG angle cannot be mirrored at the horizontal axis.

Operating the OPA with a noncollinear angle close to the intersection would lead to very efficient, unwanted SHG. The possibility to choose either positive or negative solution gives the freedom to circumvent certain parasitic processes and essentially means choosing between PVWC (positive α) and TPM (negative α) geometry. For the LWS-20 it is clearly beneficial to employ the TPM geometry which has been confirmed experimentally, too. This corresponds to a negative α or θ. One draw-back remains for the B stages, nevertheless. As figure 3.4b shows, the phase-matching condition for SHG is fulfilled for wavelengths around 750 nm when operated in TPM condition. This does not affect the amplification in this crystal but might influence the output of the A stages.

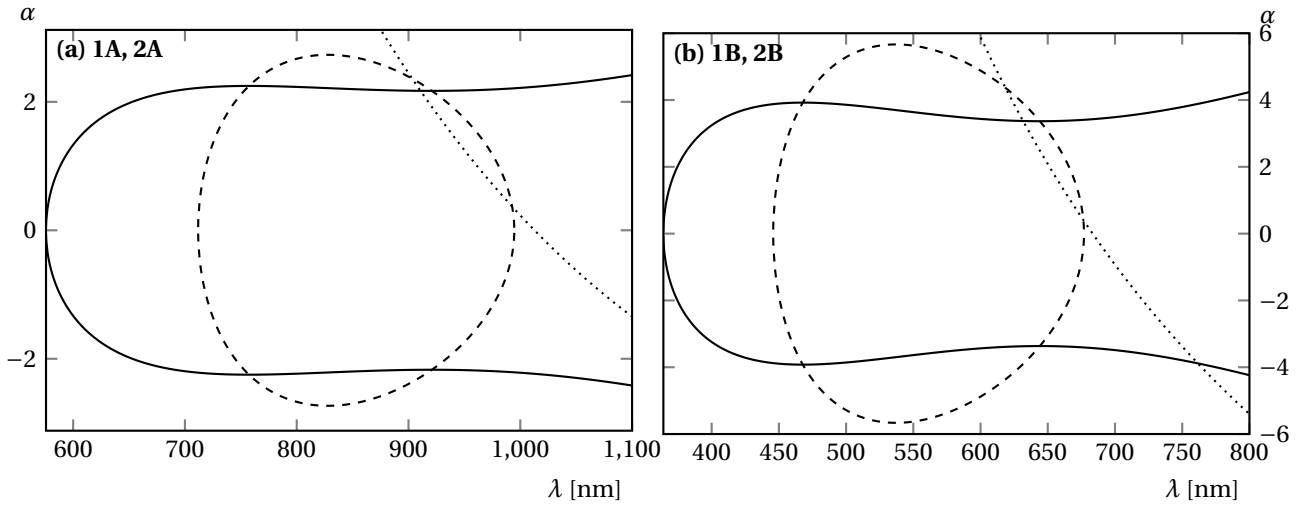

Fig. 3.4: Noncollinear angle α_{pm} for optimal OPA (solid) and α_{SHG} SHG (dotted) phase matching together with the locally broadest bandwidth angle α_{bw} (dashed) for the OPA as determined by equations (1.16), (1.18) and (1.22). In both, stages 1A, 2A (a) and 1B, 2B (b) parasitic SHG will occur in the Poynting vector walk-off compensation (PVWC) geometry, favoring tangential phase-matching (TPM).

Thanks to the relatively large beam diameters, the walk-off cannot significantly separate the beams, even in the TPM geometry, and the output is expected to be higher than in the PVWC geometry because of the absence of SHG. This is a great advantage compared to low-energy systems where tight focusing is required for good efficiencies, a regime where TPM results not only in reduced efficiency but also detrimental spatial effects leading to a severe reduction of the spatial quality [30, 31].

3.2.3 Stage 1A

Phase matching considerations and simulations show that there is a trade-off between the overall efficiency and the phase-matching bandwidth. Firstly, the bandwidth decreases for longer crystals while the gain increases (cf. equations (1.24a) and (1.7)). Secondly, it depends on the pump intensity (equation (1.24b)). Thirdly, it depends on the choice of the angles, as shown in section 3.2.1.

For illustration, three geometries have been selected to be presented and discussed here: $\theta = 23.62°, \alpha = 2.23°$ (black in figures 3.5 to 3.7) as reported in [50] as well as $\theta = 23.69°, \alpha = 2.27°$ (red) and $\theta = 23.55°, \alpha = 2.16°$ (blue) which offer a considerably better conversion efficiency at only slightly reduced bandwidth (the former) respectively a somewhat broader phase matching range at the cost of efficiency loss (the latter). The analytic considerations are depicted in figure 3.5. In the plotted configurations 3.5a, the optimal α_{pm} crosses the line of a constant α three times and vice versa for figure 3.5b, leading to three peaks in the gain curves figures 3.5c and 3.5d. This raises the possibility to tune the peak distances and their prominence by varying both angles.

Both angle plots in conjunction with their corresponding phase-matching and gain curve in figures 3.5c and 3.5d clearly show that for good efficiency both angles need to be increased resulting in flatter curves compared to the original design (black). These curves approach having a saddle point where

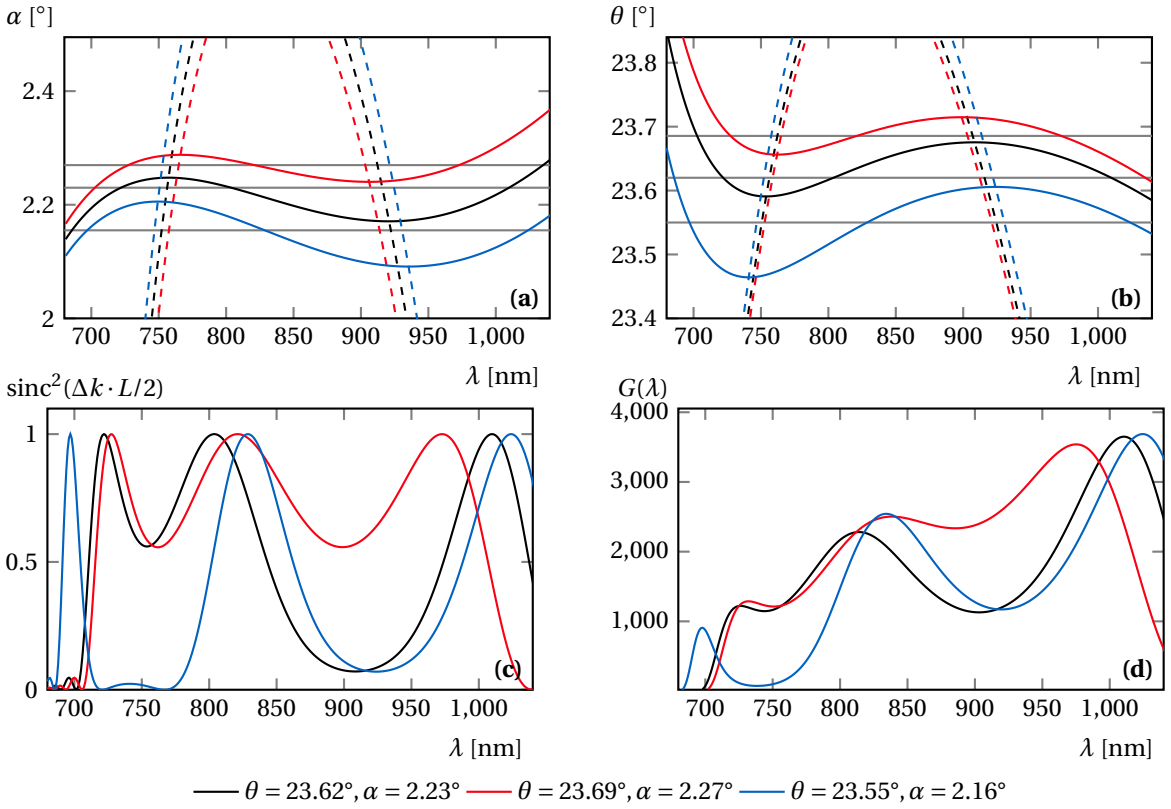

Fig. 3.5: Comparison of phase matching for three different 1A geometries. (a) The optimal noncollinear angle α_{pm} (solid) and broad-bandwidth angle α_{bw} (dashed). (b) The optimal cut angle θ_{pm} (solid) and θ_{bw} (dashed). (c) The resulting phase-matching amplitude modulation (normalized) as determined by equation (1.7).(d) Theoretical gain assuming $W_{\mathrm{p}} = 19\,\mathrm{mJ}$, $r_{\mathrm{p}} = 1.5\,\mathrm{mm}$, a flat-top pump beam, cf. equation (1.24a) and a crystal length $L_{1\mathrm{A}} = 4.5\,\mathrm{mm}$.

they also overlap tangentially with the dashed lines representing the smallest variation at one point with respect to the seed. This would ensure a very flat gain curve over a certain range with a high efficiency therein. However, the shorter and longer wavelengths suffer a much higher wave vector mismatch (WVM) there. Conversely, decreasing both angles results in a lower gain curve which spreads out further into the wings. As a result, a compromise needs to be found when aiming for broadband high energy pulses.

The simulations have been performed assuming a pump radius of 0.75 mm as mentioned in section 2.2 and a seed energy $W_{\mathrm{s,in}} = 150\,\mu\mathrm{J}$ with the cross-polarized wave generation (XPW) stage inserted. Figure 3.6 shows the obtained output spectra and table 3.1 the respective energies and conversion efficiencies. By its very nature optical parametric amplification cannot convert the full pump energy to the signal beam since a part is always transferred to the idler beam, accounting for the so-called quantum defect. A reasonable quantity is the fraction of the created signal photon number ΔN_{s} and the total number of input pump photons N_{p} and called quantum efficiency (QE):

$$\eta = \frac{\Delta N_{\mathrm{s}}}{N_{\mathrm{p}}}. \tag{3.9}$$

Division by the input yields the energy gain plotted in figure 3.7 according to equation (3.12) which

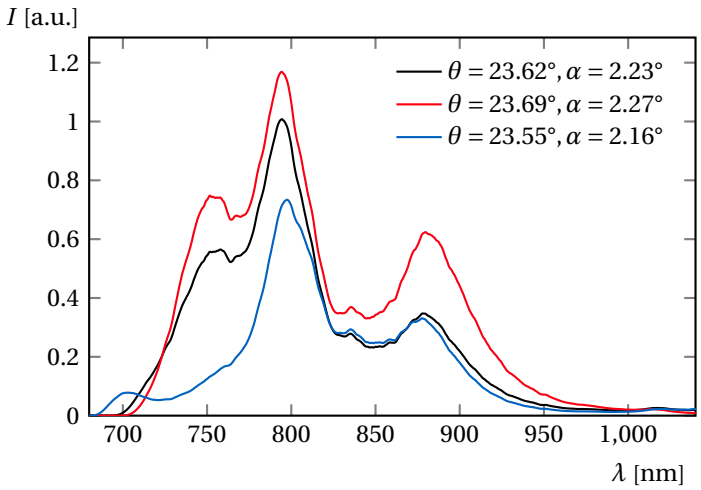

Fig. 3.6: Simulated spectra of OPCPA crystal 1A for different phase-matching conditions.

θ [°]	α [°]	$W_{s,out}$ [µJ]	η
23.62	−2.23	118	0.009
23.69	−2.27	138	0.011
23.55	−2.16	87	0.007

Tab. 3.1: Simulated 1A signal output energy $W_{s,out}$ and quantum efficiency η depending on (α,θ) combinations fir a 150 µJ seed.

agrees remarkably well to the calculated curves in figure 3.5d in shape and almost in magnitude. The difference in magnitude results from the underlying simplifications of equation (1.24a) where a flat-top beam is assumed. The maximum intensity of the super-Gaussian beam defined in the simulation was taken as magnitude of the flat-top pump beam. This leads to the conclusion that the analytic framework delivers useful output and the `Mathematica` notebook is a useful tool for phase-matching considerations. The fact that the input spectrum does not significantly affect the gain curve shows that this stage is operated far away from depletion and the accompanying saturation affects.

This is more clearly visible in figure 3.8 where the transversal beam profiles are plotted against the delay. Here, the time axis corresponds to the spectrum via its monotonic group delay with the blue part having a negative and the red part having a positive delay, cf. figure 2.2. The extraordinary pulses do not experience a large loss in intensity, thus leaving enough pump photons for the process to remain unsaturated. It must be pointed out that in this thesis all spatio-temporal profile plots are normalized which has to be taken in account for when comparing different plots.

The transversal asymmetry is caused by both, pump walk-off and the propagation of seed and idler in different directions caused by the noncollinear geometry. Over the crystal length of $L = 4.5\,\mathrm{mm}$, the displacement between pump and seed

$$\Delta x_{p,s} = L(\tan\rho - \tan\alpha) \tag{3.10}$$

amounts around 430 µm depending on the chosen geometry. The offset between idler and seed which is defined accordingly is nearly the same for $\lambda_s \approx 900\,\mathrm{nm}$ and grows above 700 µm for $\lambda \approx 700\,\mathrm{nm}$. As the pump beam walk-off takes place in positive x direction (see figure 1.4), the seed was shifted relative to the pump by +0.6 mm. Still, the highest intensity of the signal pulse lies in the positive direction which indicates that the region of spatial overlap should lie relatively far at the end of the crystal. This is mostly because of the relative idler offset which cannot be compensated.

As a final remark, the angular configuration in [50] agrees very well for the Sellmeier equations (A.1) used in the scope of this thesis and the simulations which will be confirmed for the B stages, too. A

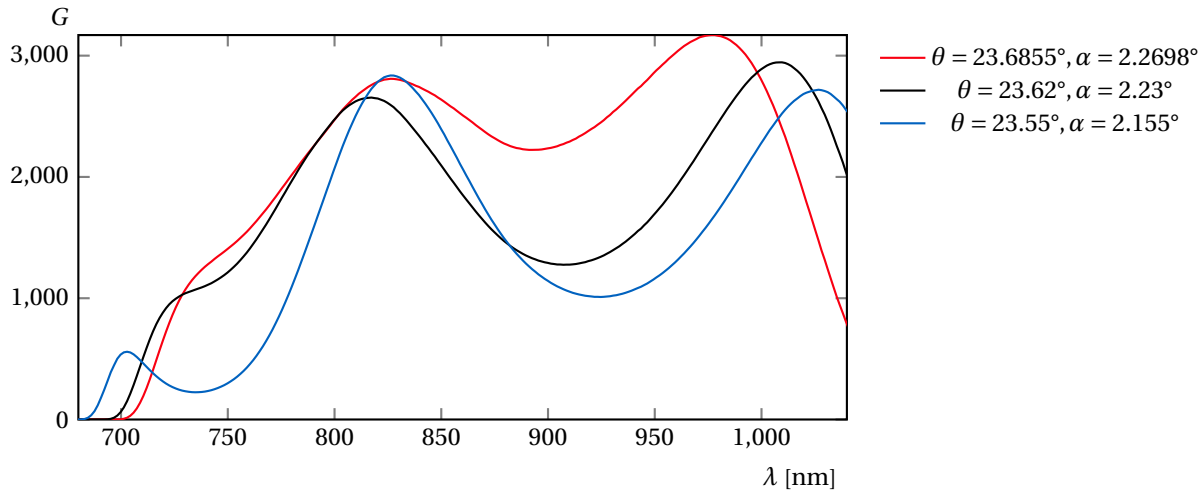

Fig. 3.7: Simulated energy gain curves of OPCPA crystal 1A for different phase-matching conditions.

slight detuning shifts the curve towards smaller wavelengths which is beneficial for narrowing the gap in the spectrum without losing much on the long-wavelength edge. Having said that, the room for improvement is not very large as the small shift in figure 3.3 cannot be continued arbitrarily without detrimental effects, see the examples described above. For the further simulations, the red curve ($\theta = 23.69°, \alpha = 2.27°$) was chosen.

3.2.4 Stage 2A

As the second A stage is amplifying the same spectral portion as the first one, the geometrical phase-matching considerations above apply here as well. The differences are beam size and energy as well as a slightly increased crystal length.

While the pump intensity is approximately half, the seed energy has increased by three orders of magnitude with an area that is increased by a factor of approximately twenty-five. This results in an increase of fluence by more than one and a half orders of magnitude as compared with stage 1A. This leads to higher conversion efficiencies and as it will be discussed in section 3.3.1, pump depletion and gain saturation come into play as a result.

The larger beam size leads to a reduced relative walk-off which is observable mainly in the pump beam profiles in figures 3.15 and 3.16. The signal pulses remain rather symmetric in intensity albeit being tilted due to the noncollinear propagation.

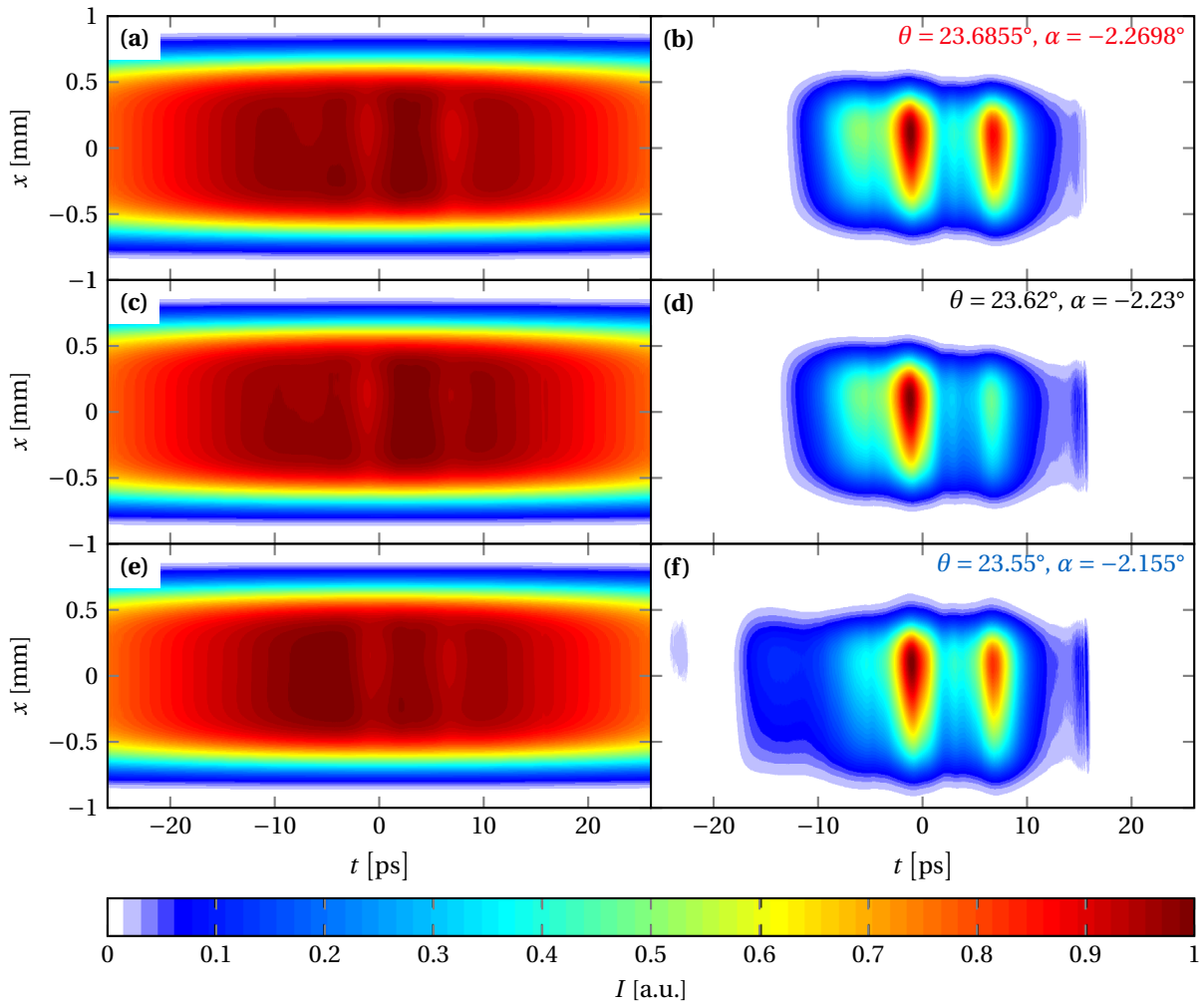

Fig. 3.8: Spatio-temporal intensity distributions of pump (a, c, e) and signal (b, d, f) after stage 1A.

3.2.5 Stages 1B and 2B

Owing to the different seed and pump wavelengths compared to the A stages, the geometry in the B stages has notably different features as visualized in figure 3.9. The first and most striking difference is the absence of an inflection point in the relevant parameter area caused by the larger slope of the angle-dependence on the wavelength, cf. figures 3.4a, 3.4b, 3.9a and 3.9b. Consequently, there are only at most two peaks in the phase-matching curves. The red and green curves in figure 3.9 show that there is a fine-tuning option since both angles can be varied by a similar amount in order to shift the phase-matching area. In all four plots, the have a very similar shape, except for being shifted. It is possible to push the peaks of optimal phase matching apart by decreasing θ and/or increasing α which goes in hand with a decrease of efficiency in between the peaks until they separate completely. This is exemplified by the orange and blue curves, where only θ was decreased with respect to the red and green curve.

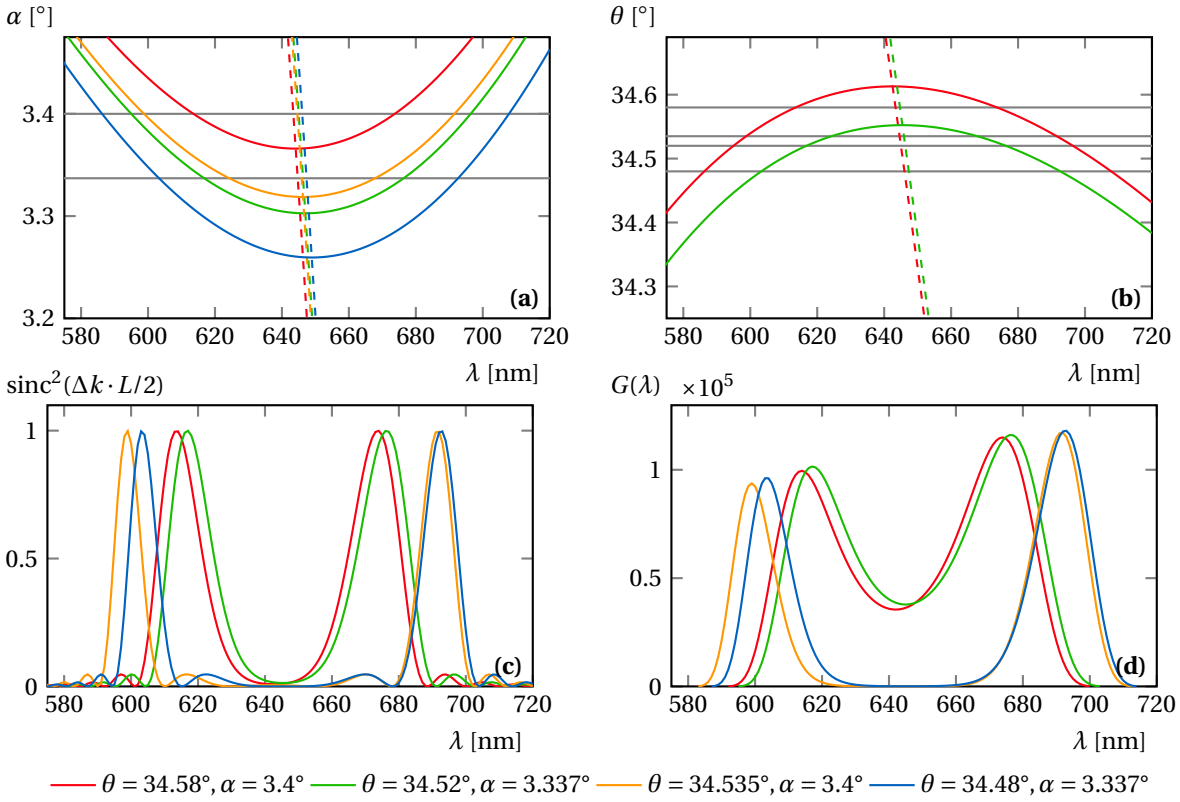

Fig. 3.9: Comparison of phase matching for different 1B geometries. (a) The optimal noncollinear angle α_{pm} (solid) and broad-bandwidth angle α_{bw} (dashed). (b) The optimal cut angle θ_{pm} (solid) and θ_{bw} (dashed). (c) The resulting phase matching amplitude modulation (normalized) as determined by equation (1.7).(d) Theoretical gain assuming $W_{\mathrm{p}} = 19\,\mathrm{mJ}$, $r_{\mathrm{p}} = 1.5\,\mathrm{mm}$, $L_{1\mathrm{B}}$ and a flat-top pump beam, cf. equation (1.24a).

Generally, the phase-matching range is much smaller than for the A stages due to the larger dispersion at small wavelengths. As figure 3.9c shows, the gain for a low-intensity pump splits up and nearly vanishes in the central region in the used geometry (red). Thus, it is not broad enough for amplifying the entire low-frequency part of the LWS-20 spectrum (figure 2.2). A certain minimum pump intensity is therefore necessary and when choosing appropriate angles, one should consider the finite-intensity gain curve plotted in figure 3.9d.

The input spectrum and phase for the simulation are the overall input from figure 2.2. For the simulation, the parameters from [50] ($\theta = 34.58$, $\alpha = -3.4°$, red curve in figure 3.9) were found to be very good also in these analytical considerations and were chosen as an input for simulations. The resulting amplified spectrum and gain curve are plotted in figure 3.10 which looks similar as predicted by figure 3.9d albeit having a dip to almost zero at 675 nm visible also in the spatio-temporal profile in figure 3.11. This is an artifact with unknown cause. It might be related to the fact that the pulses are not completely contained in the time window. For example, any components that move out of the temporal window in the positive direction will appear at the negative edge of the time window. This can cause odd effects which are completely unphysical.

The same configuration is desirable for 2B which could not be simulated because of the restrictions

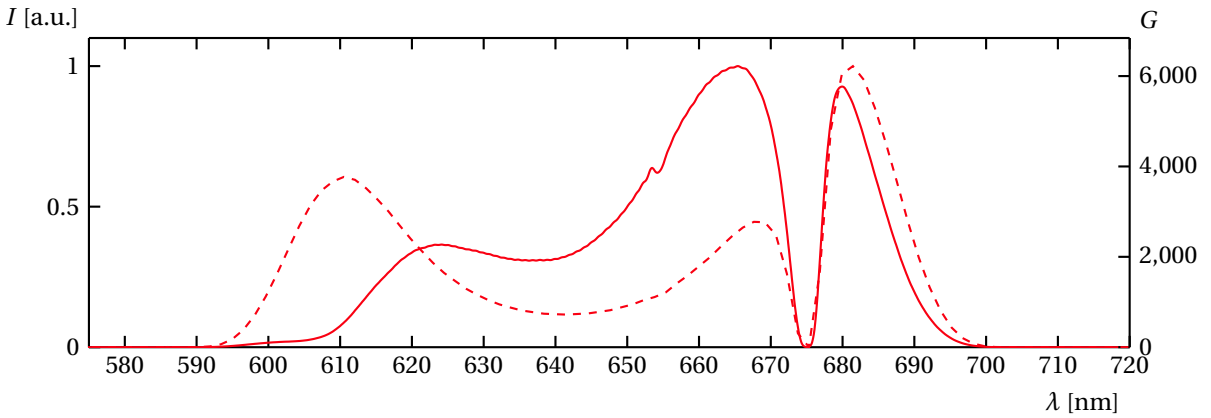

Fig. 3.10: Simulated output spectrum (solid) and gain curve (dashed) of stage 1B. The dip at 675 nm is an artifact which is not observed in the experiment.

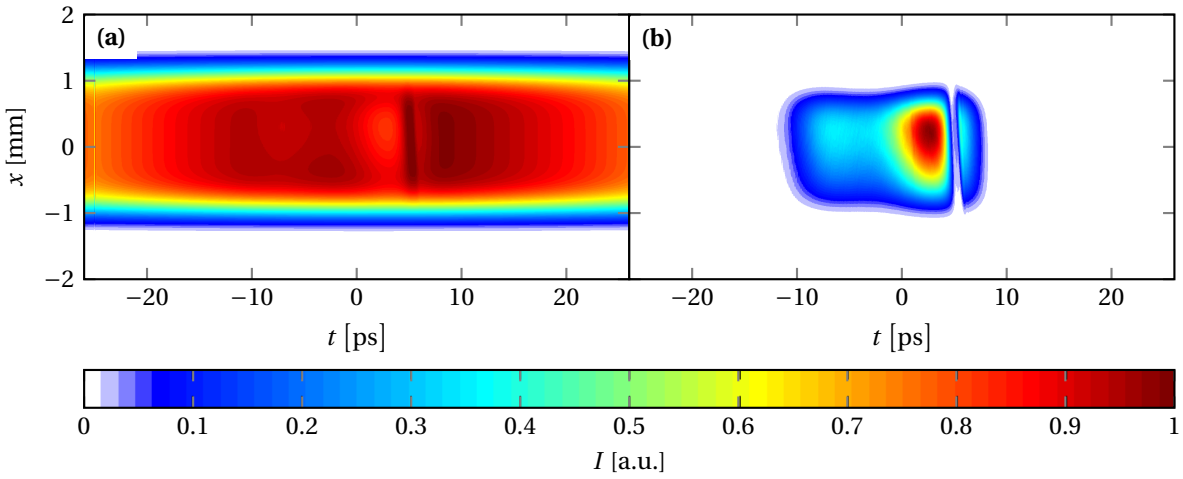

Fig. 3.11: Simulated spatio-temporal pump (a) and signal (b) pulse profiles after stage 1B. The gap around 5 ps delay is an artifact which is not observed in the experiment.

outlined in section 3.1.1.

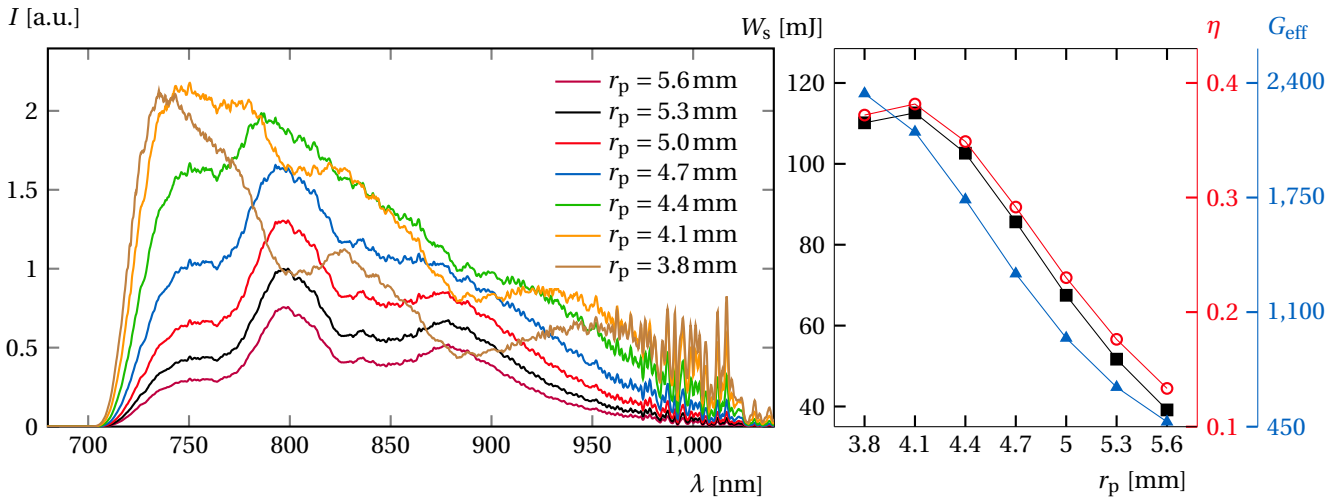

Fig. 3.12: Simulated spectra of OPCPA stage 2A for varying pump radii under otherwise constant conditions.

Fig. 3.13: Effect of the 2A pump radius on signal energy W_s (black squares), quantum efficiency η (red circles) and effective gain G_{eff} (blue triangles).

3.3 Influence of the pump intensity on the amplification

As the gain scales with the pump intensity (equation (1.24a)), this is a parameter that should be maximized whilst avoiding detrimental effects such as back-conversion of signal and idler to the pump. There were some experimental signs indicating that saturation is reached in stage 2A and pump intensity reduction might optimize the output. A possibility of increasing the pump beam's intensity while retaining its energy is to reduce its diameter. In this section, an assessment of an efficiency enhancement is done as well on other occurring effects. Additionally, results are compared with measurements with decreased pump energy.

3.3.1 Pump radius variation

Several parameter scans were performed varying the pump radius of amplifier stage 2A which is currently 5.3 mm as measured with a camera. As they shared the same basic results, one is exemplarily discussed in the following. It uses the output of the above described 1A simulation run represented by the red line in figure 3.6.

As shown in figure 3.13, the energy and quantum efficiency scale slightly different with the pump radius. This is due to a change of the spectral shape discussed below. Aside from that, both reach a maximum when the pump radius is decreased and decline for even smaller radii. The reason is that while the pump intensity increases, the fraction of the seed area that is being pumped decreases resulting in a reduced seed energy resp. photon number within the overlap area of pump and seed. It is thus instructive to consider the *effective* seed energy W_{eff} and gain G_{eff} bearing in mind and keeping

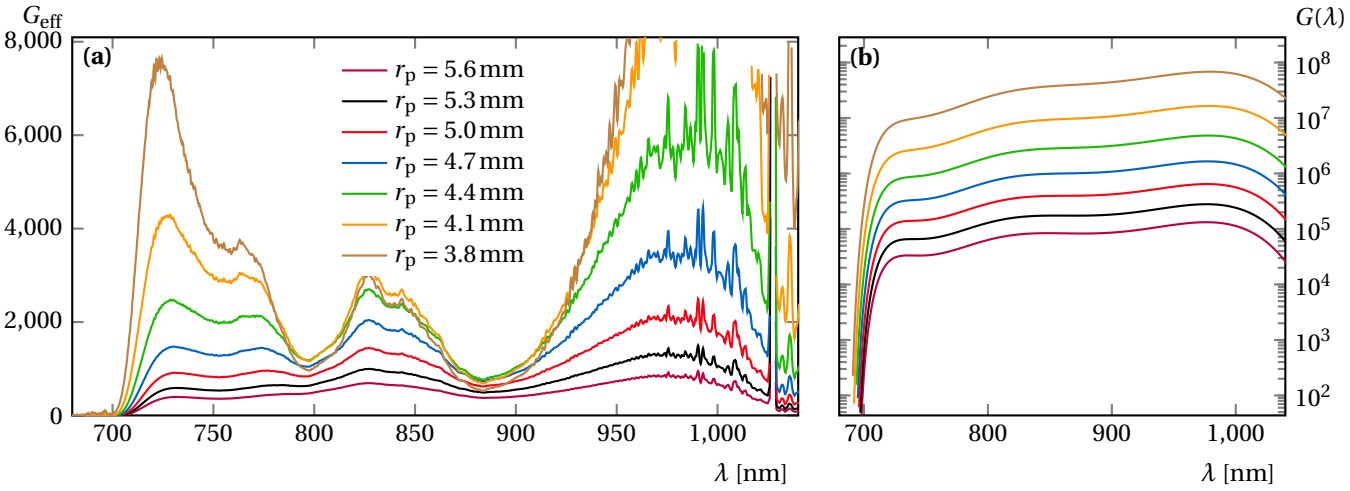

Fig. 3.14: Simulated (a) and calculated (b) 2A (effective) gain curves for various pump radii and a fixed pump energy of 460 mJ.

the notation of equation (2.1a) for the pump and seed profiles:

$$W_{\text{s, eff}} = W_{\text{s,tot}} \frac{\int_0^{\Delta x/2} I_{2,\text{s}}(r) I_{n,\text{p}}(r) r \,\mathrm{d}r}{I_{0,\text{p}} \int_0^{\Delta x/2} I_{2,\text{s}}(r) r \,\mathrm{d}r}, \tag{3.11}$$

$$G_{\text{eff}} = \frac{W_{\text{s,out}}}{W_{\text{s,eff,in}}}. \tag{3.12}$$

The integration is performed in order to consider the varying intensities over the profile.

As expected, the resulting spectrally integrated effective energy gain does not decrease for smaller radii. Regarding energy or quantum efficiency, respectively, a pump radius of 4.1 mm lies near the optimum with more than double of the output energy with $r_p = 5.3\,\text{mm}$ which makes it worth investigating closer.

The change of the spectra and effective gain curves in figures 3.12 and 3.14a is far more interesting with respect to beam quality and compressibility as it shows the different behaviour. A moderate decrease in pump radius down to 4.7 mm results in a slightly less modulated and broader spectrum without changing the overall spectral shape too much. Still the reduced amplification of the maxima compared to the minima unveils that the high intensity regime with saturation effects is reached already here, a fact that is apparent in comparison to the input spectrum plotted in red in figure 3.6 as well. All in all, from a spectral point of view, the positive effects of higher energy and a broader spectrum dominate here.

When proceeding to even smaller radii, the situation is completely different. Here, the maxima even become minima with values below the lower-intensity curves. Just in the wings below 770 nm and above 950 nm the intensity and gain keep increasing. A reason for this is certainly the reduced input photon number, the effective gain curve is still rising until 3.8 mm. Comparison of figures 3.14a and 3.14b shows that the analytically calculated gain curve sets only limits on the spectral amplification

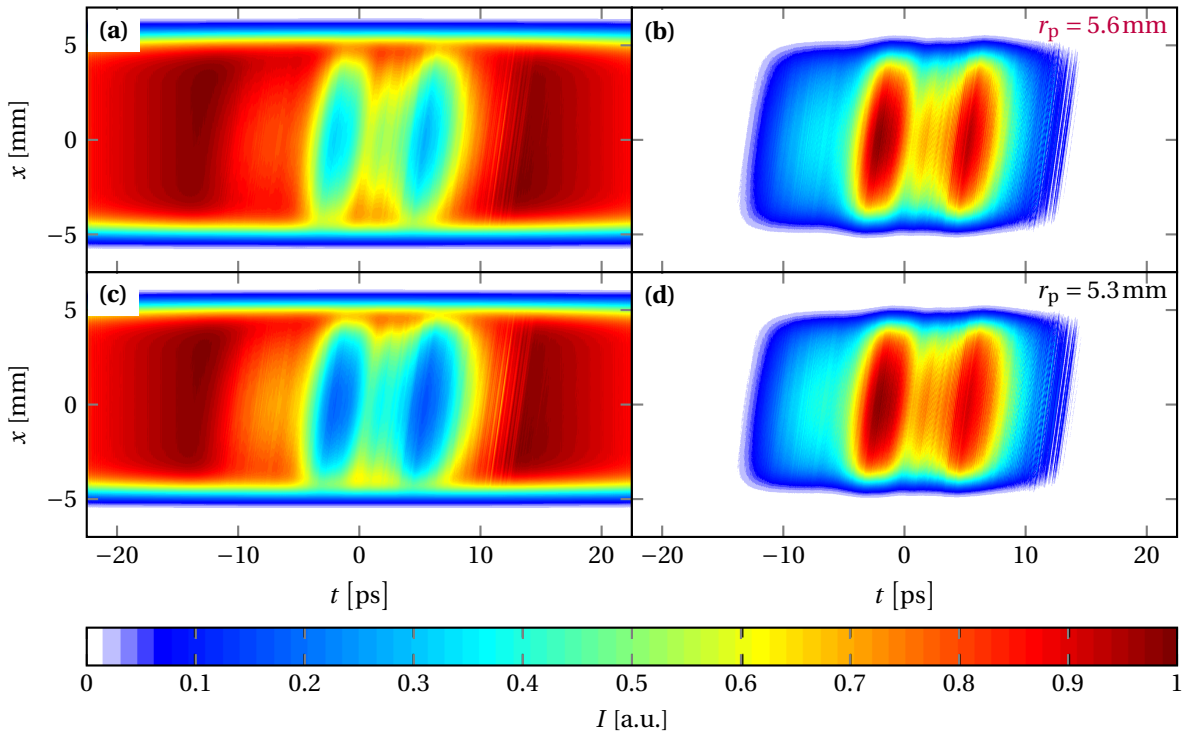

Fig. 3.15: Simulated spatio-temporal intensity distributions (normalized) of stage 2A output pump and signal with different pump radii.

range, and is losing its role of describing the actual gain which becomes minimal at maxima of the input and vice versa.

A closer look on the gain curve corresponding to the smallest pump beam and especially on the spatio-temporal beam profiles of pump and signal after the stage in figures 3.15 and 3.16 reveals that back conversion takes place at the location of the input maxima for radii smaller than 4.7 mm. As mentioned before, the time axis corresponds to the spectrum such that shorter wavelengths appear on the left (negative times) and longer wavelengths on the right (positive times). Most evident are the effects in the pump profile where already a significant depletion is visible with a pump radius of $r_p = 5.3\,mm$. Beginning at $r_p = 4.7\,mm$, the pump part belonging to the left maximum around 800 nm is fully depleted and that associated with the right maximum around 880 nm even shows some weak back-conversion. As the pump beam decreases the area of back-conversion increases and the sphere of pump depletion spans out farther. Furthermore, the reversal of maxima and minima can be observed in the profiles. Bear in mind that the increased gain bandwidth as the radius decreases which is visually an increase in the sketched signal pulse length in figure 3.16. This is not to be confused with an increase in the Fourier limit which would lead to the opposite, i.e. a shorter stretched pulse length.

In conclusion, reducing the pump radius is a low-cost option for further enhancing the output energy. However, pump depletion and thereby invoked back-conversion sets a strong limitation on the minimum pump diameter. The simulations suggest a viable diameter in between 4.7 mm and 5.0 mm which corresponds to an increase in energy of up to 65 %.

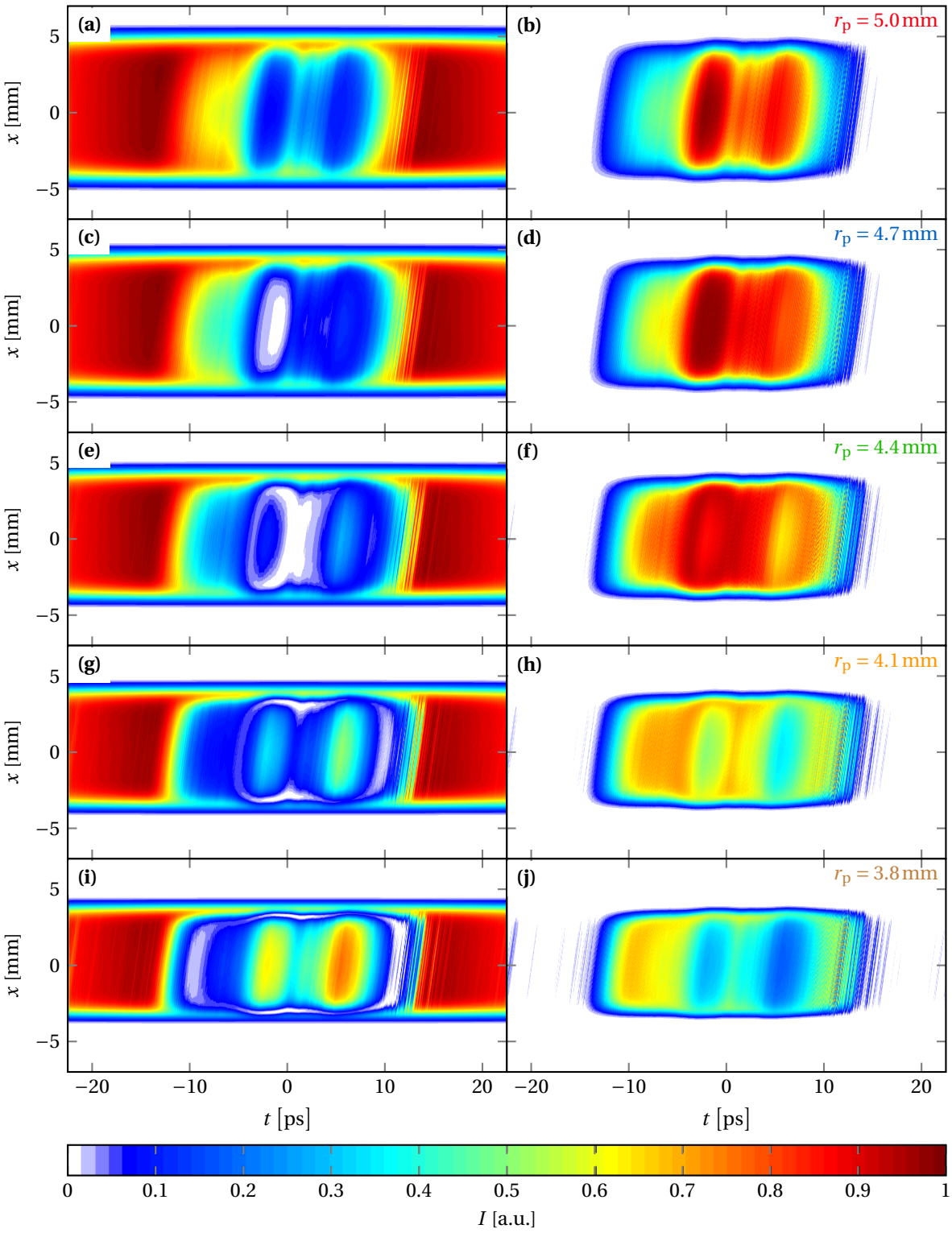

Fig. 3.16: Simulated spatio-temporal intensity distributions (normalized) of stage 2A output pump and signal with different pump radii. (f), (g), (h) appear to get weaker because they are normalized with respect to the highest ordinary-polarized intensity, here appearing at one location in the idler..

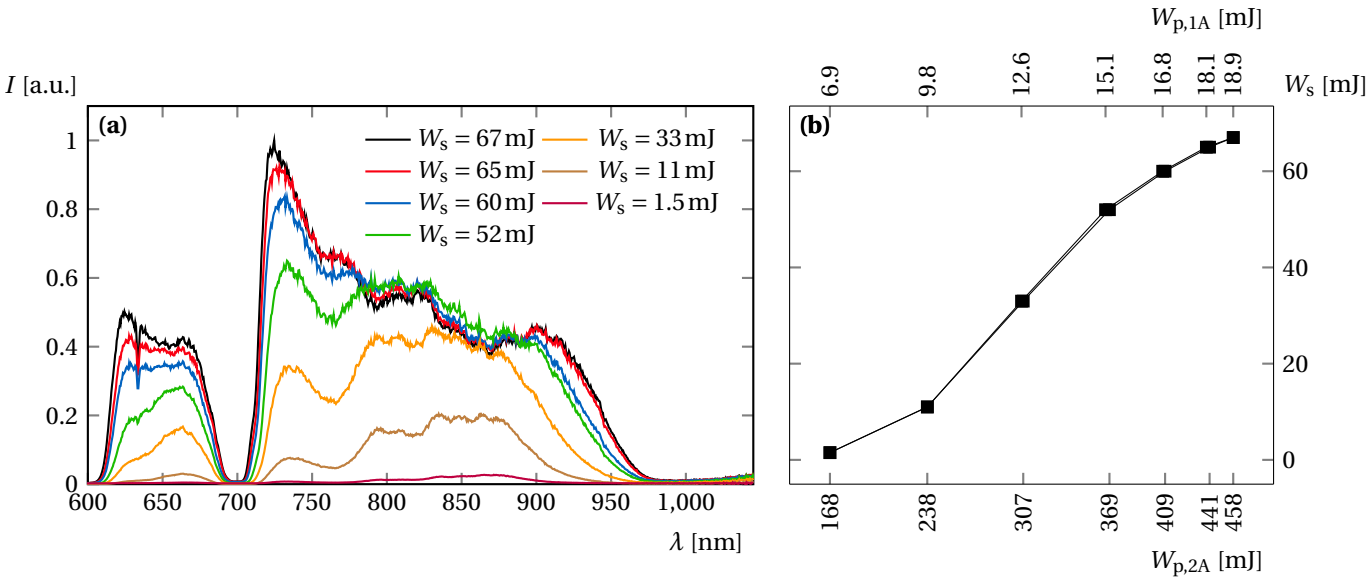

Fig. 3.17: Measured effect of reducing the pump power on the final NOPCPA output. (a) Spectra for varying pump power. The dependence of the amplified signal energy W_s on the pump energies of stage 1A (upper axis) and 2A (lower axis) are plotted in (b).

The modulations on the right (positive time) are largely caused by noise of the input spectrum which has not been smoothed for these simulations. When using smoothed input spectra, they largely disappear.

3.3.2 Pump energy variation

For the sake of a comparison to experimental values, a related experiment was performed. The spectra and output signal energies W_s were observed while the pump energy W_p was simply decreased. As the whole pump system power was decreased, the pump energy of all four stages changed almost proportionally to each other, just the 1B pump energy decreased slightly more. Nevertheless it is possible to identify and compare the saturation effects from around 780 nm to 900 nm which set in around a 2A pump energy of 370 mJ, see the reduced slope in figure 3.17b and the spectra in (a). The spectral area of saturation is thus the same as in the simulations with reduced pump diameter. A major difference between experiment and simulation is the already apparent much larger saturation in the experiment. This is another indication that the pump diameter should only be decreased moderately to avoid back-conversion.

The spectra also indicate that there is still some room for raising the pump intensity in stage 2B since saturation emerges only in the right portion for wavelengths longer than 650 nm.

As a result, simulations as well as actual measurements suggest benefits from pump diameter reduction by up to ten percent in conversion efficiency which should be tested experimentally because of probable higher saturation, damages and contrast degradation in an experiment.

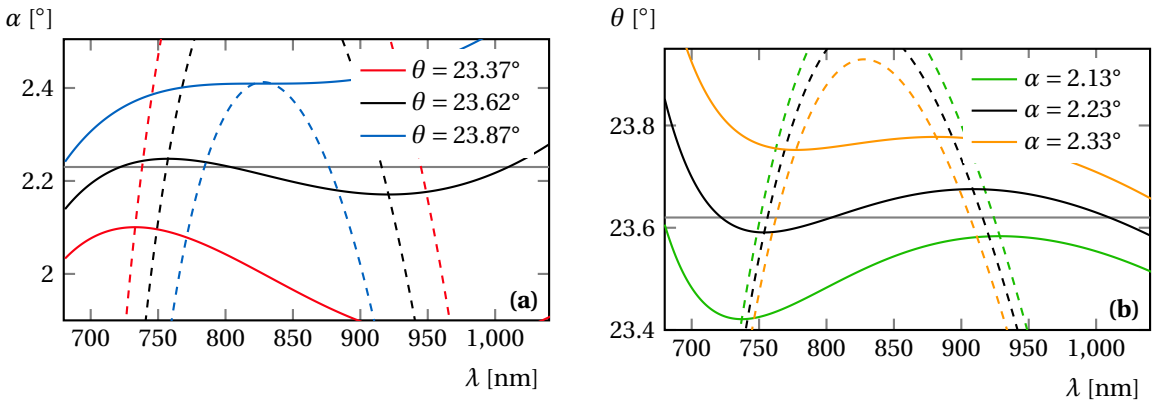

Fig. 3.18: Phase-matching geometries $\alpha_{\mathrm{pm}}(\theta)$ (a) and $\theta_{\mathrm{pm}}(\alpha)$ (b) for A' stages illustrating a narrow phase-matching range towards lower frequencies..

3.4 Additional crystals for broader phase-matching

Having assessed the possibilities of gain enhancement by reducing the pump diameter, a second goal is to improve the bandwidth. Analytical calculations have shown that a significant increase of the bandwidth is not possible in any of the stages by choosing a different geometry, see section 3.2. Of course the possibility of losing energy in the spectral wings and weakening the gap remains which is possible with corresponding alignment. However, a stable solution including the wings is highly desirable and would open the way for even shorter and more intense pulses.

3.4.1 Additional crystals

Adding another stage with independently tunable angles would open up many more phase-matching possibilities by tailoring both, α and θ to the specific needs. The resulting gain curves could then be combined. This, however, would require an own pump which imposes considerable effort. A substantially easier alternative is to leave the setup unchanged but simply add a second crystal behind the existing crystal of a stage with a different cut angle θ. The angle between pump and seed, α, is fixed to the already existing value.

The condition of a fixed noncollinear angle is a strong constraint. Figure 3.18 shows that for the A stages, broadband phase matching is almost impossible in the short wavelength edge of their amplification range. In fact, phase matching around 700 nm is only possible when increasing θ, cf. figure 3.18a. However, by virtue of the large slope of the curve, the phase-matching range will be extremely small since the angle α_{bw} for broadest phase matching drifts apart more and more. The same is deduced from figure 3.18b: For a fixed α (either black or green or yellow line), phase matching towards the smaller wavelengths is achieved when shifting up the horizontal line representing the chosen θ. Here, the phase-matching range is extremely small as explained before.

By contrast, stages B1 and B2 posses a parabola-like relation between phase-matching (θ) and non-collinear α angle. When choosing the former such that the latter is near the minimum, a certain spectral range is amplified efficiently. When decreasing θ, the phase-matching curve splits up into two distinct peaks on each side and the width and position of the peaks can be adjusted by solely

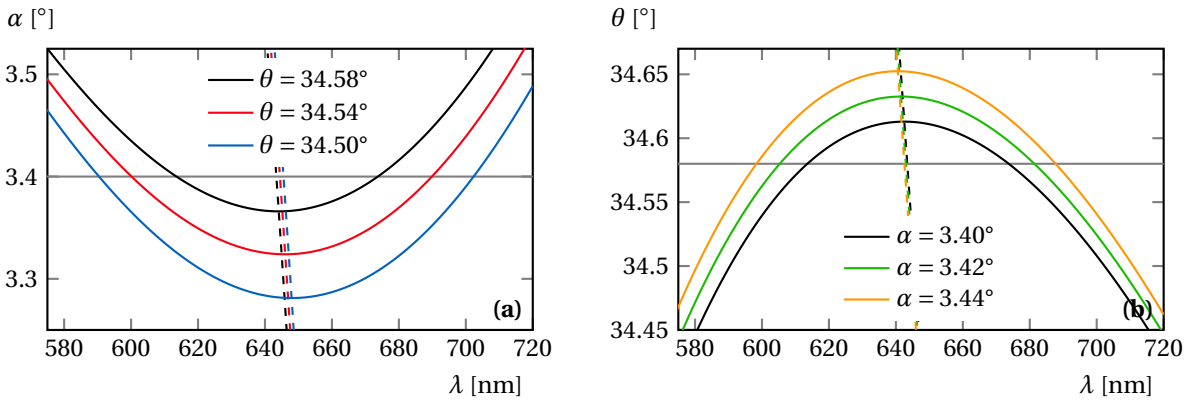

Fig. 3.19: Phase-matching geometries $\alpha_{\mathrm{pm}}(\theta)$ (a) and $\theta_{\mathrm{pm}}(\alpha)$ (b) for B' stages illustrating a splitting of the gain curve towards smaller θ.

tuning θ which follows clearly from figure 3.19a. In this way, the gap can be closed and the overall phase-matching range is even extended to shorter wavelengths. Consequently, the B stages are to be focused on for this task.

The above considerations are supported by figure 3.20 where the analytic gain curves of the stages 1A and 1B respectively 2A and 2B are plotted. It is apparent that adding crystals at the B stages is more promising than at the A stages where merely a weaker gain can be reached in the region of the gap.

For the simulations of 1B', the output signal spectrum and phase of the preceding unprimed crystal (1B with 34.54° and 3.42°) were taken as the input and seed and pump energy as well as radii were reduced accordingly. The reason is that it is not possible to save the full array for $E(f,\nu_x)$ in `chi2D` due to its large size. Consequently, just the spectra were saved including spectral phases. This discards particularly the spatial information in areas of depletion or asymmetries caused by walk-off. In fact, this imposes a major inaccuracy for high depletion such as in stage 2A, where back-conversion could happen in the additional crystal. A way to overcome this drawback is to tune the delay such that the spectral phase-matching range of the seed overlaps with one half of the pump and shift the delay afterwards for an overlap with the other, so far undepleted, half.

Furthermore, since the idler is angularly dispersed it was not possible to include this either. Test runs when including a collimated idler at a fixed angle as input pulse for primed stages did not show a noticeable difference which is why this anyway inaccurate approach was forgone and the idler from the unprimed stages was not regarded.

Bearing in mind these restrictions, angular configurations for additional crystals for each of the simulated stages were tested with results expounded in the following subsections. The additional crystals will be referred to as 1 and 2 A' and 1B' respectively.

Additional crystals 1A' and 2A'

Even though the B stages seems to offer easier tunability of the phase-matching curve, the outputs of both, stage 1A and 2A were taken as an input for another crystal with $\theta = 23.75°$ (blue) or $\theta = 23.81°$ (green) and the same $\alpha = 2.27°$.

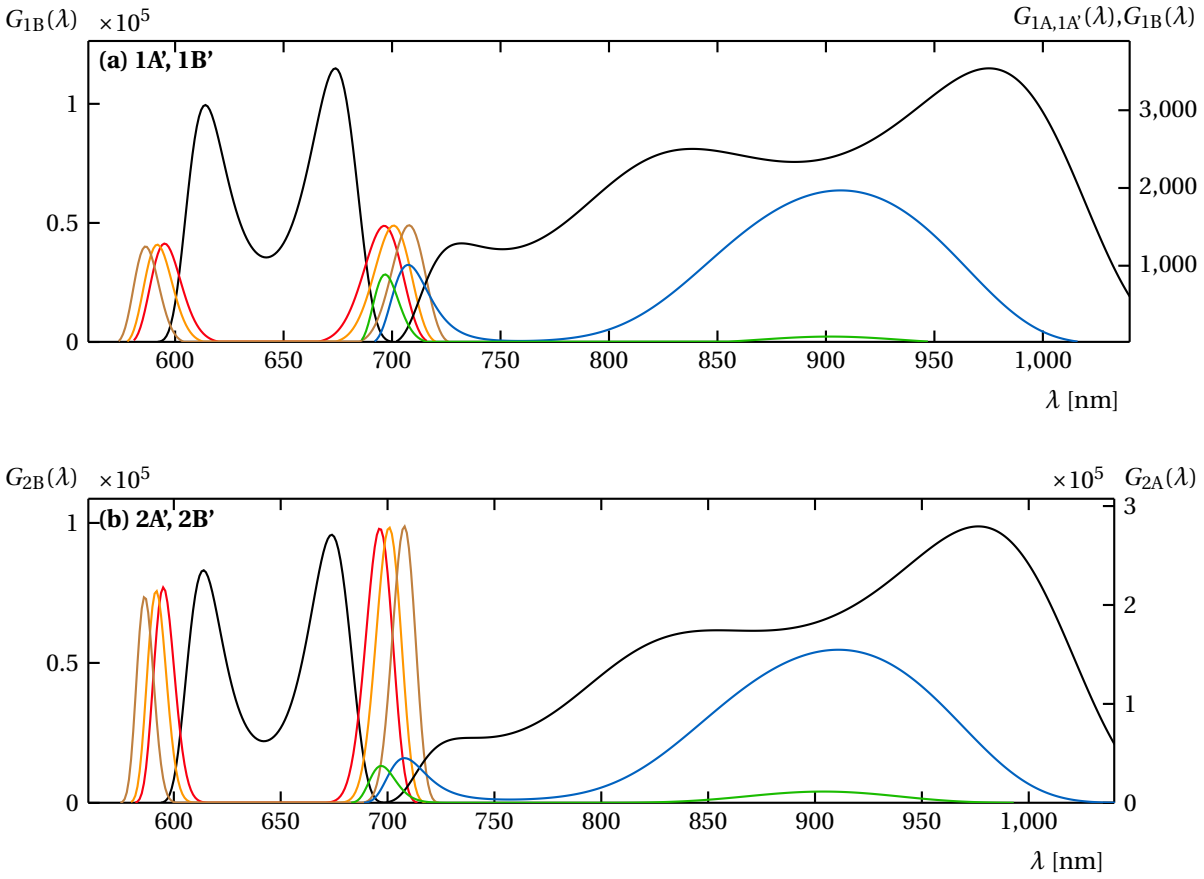

Fig. 3.20: (a) Left axis: calculated gain curves for 1B ($\theta = 34.58°$, $\alpha = 3.4°$, $L = 4.5$ mm, black). Right axis: 1B' with $\theta = 34.52°$ (red), $\theta = 34.51°$ (orange) or $\theta = 34.48°$ (brown) and 3 mm, as well as 1A ($\theta = 23.69°$, black) and 1A' with $\theta = 23.75°$ (blue) or $\theta = 23.81°$ (green) and a crystal.
(b) Calculated gain curves for 2A,B and 2A',B' with the same angles as in (a) and a length of 5 mm..

1A' Theoretical gain curves and output spectra of stage 1A' for both crystal angles and a length of 2 mm, 2.5 mm and 3 mm are plotted in figure 3.21a. Due to the expected onset of optical parametric fluorescence (OPF) which is not included in the simulations, longer crystals were not simulated. For the 2 mm long crystals, the gain is reduced by up to two orders of magnitude compared to the plotted curves for 3 mm.

The simulated gain curves are plotted in figure 3.21b. It can be seen that even though the gain is higher near 700 nm, the spectra are amplified by a similar amount over all the range in 2 mm long crystals which does not result in a considerably broader output nor does it help to close the spectral gap between A and B stages. For $L = 2.5$ mm and even more for $L = 3$ mm, the gain curves show more distinct features in the spectral wings leading to slightly broader spectra. While the shortest crystal shows larger gain for $\theta = 23.81°$ than for $\theta = 23.75°$ below 719 nm this point moves to 703 nm in both longer crystals. Considering that $\theta = 23.75°$ yields a higher gain above this threshold makes it preferrable for increasing the energy, but not really suitable for extending the gain curve towards

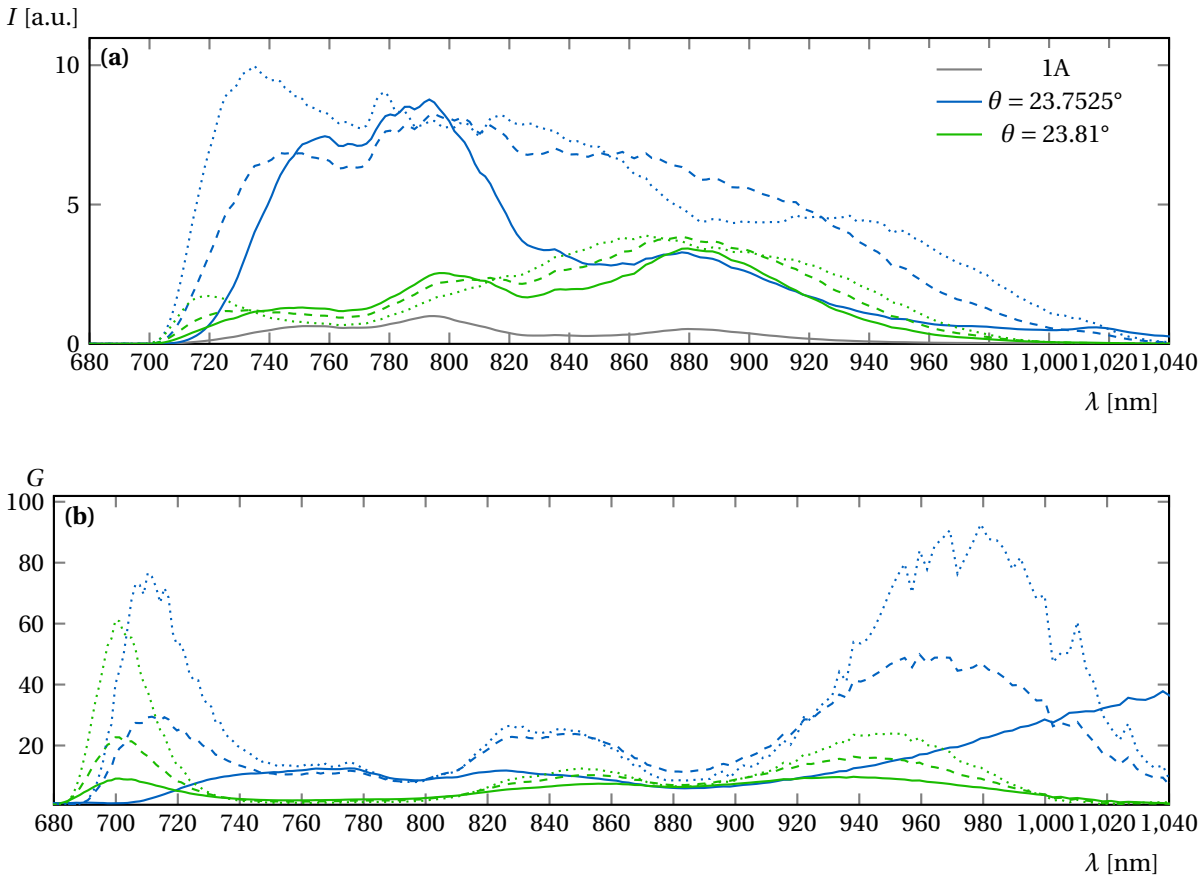

Fig. 3.21: Simulated spectra (a) and gain curves (b) of 1A' crystals after a 1A crystal with $L = 4.5\,\text{mm}$, $\theta = 23.69°$, $\alpha = 2.27°$ (red in figures 3.5 to 3.7, the spectrum is represented here in gray). Solid: $L_{1A'} = 2\,\text{mm}$, dashed: $L_{1A'} = 2.5\,\text{mm}$, dotted: $L_{1A'} = 3\,\text{mm}$.

shorter wavelengths. In an experiment, the angle should be varied to optimize between broader and higher gain to yield the effectively broadest spectrum. Anyway, the spectrum is not expected to be tunable considerably lower than 700 nm.

Seeing the benefits of a longer crystal, the length is not only limited by OPF but, as the beam profiles in figure 3.22 reveal, also by saturation and back-conversion. At the intensity maxima back-conversion sets in after around 2.5 mm propagation in the crystal. This limits the crystal length for 1A' to about that value.

Additionally, the beam profiles show that spatial walk-off between pump and seed is not a gain-limiting factor with the regarded crystal lengths. Nonetheless, the signal beam gets already slightly distorted spatially after 2.5 mm of propagation which is another reason why a much longer crystal is not advisable. Generally, the additional crystal should be placed very close after the existing crystal in order to obtain a sufficient spatial overlap.

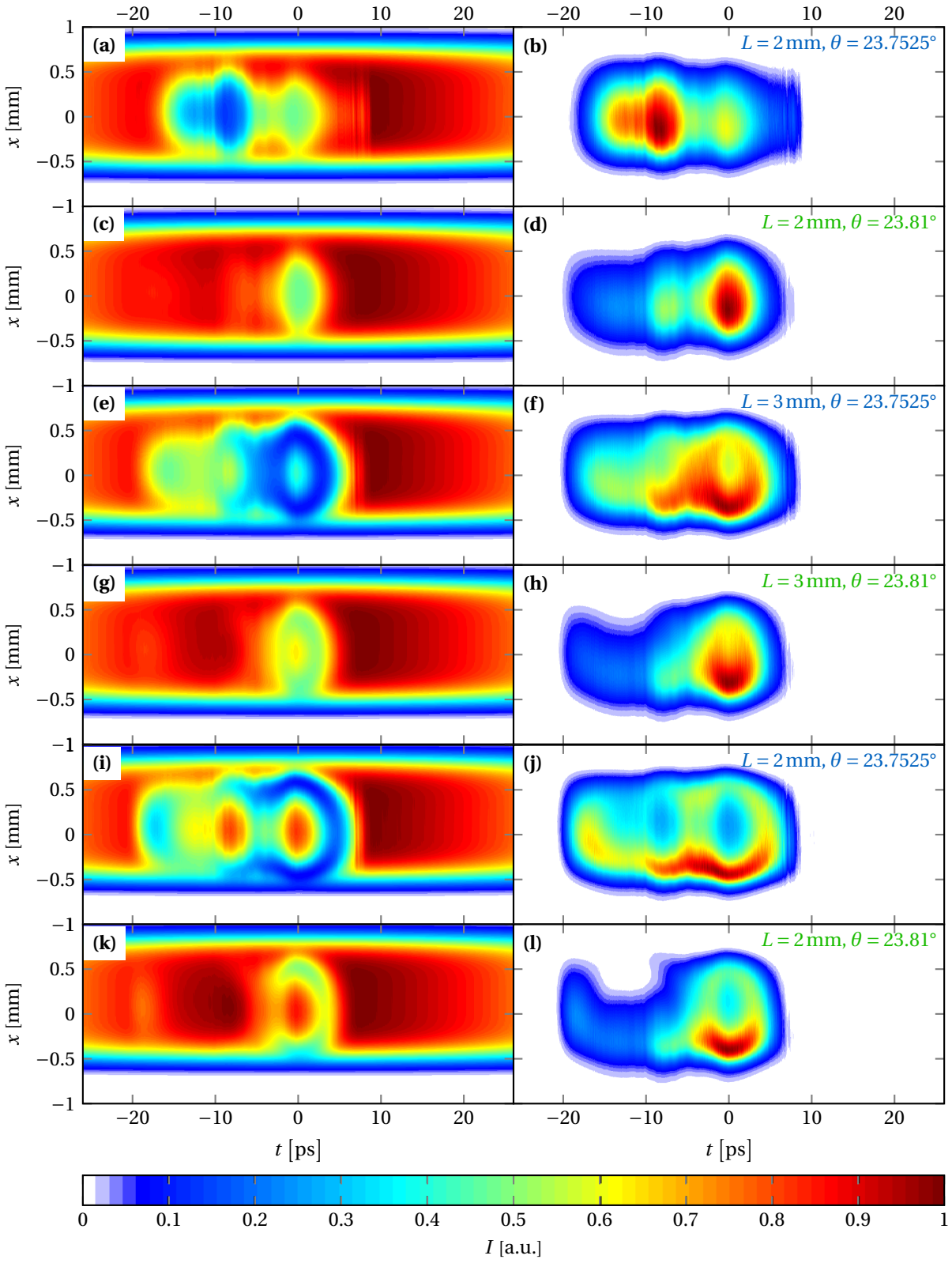

Fig. 3.22: Simulated spatio-temporal profiles of 1A' crystals after a 1A crystal with $L_{1A} = 4.5\,\text{mm}$, $\theta_{1A} = 23.69°$, $\alpha_{1A} = 2.27°$ (red in figures 3.6 and 3.7).

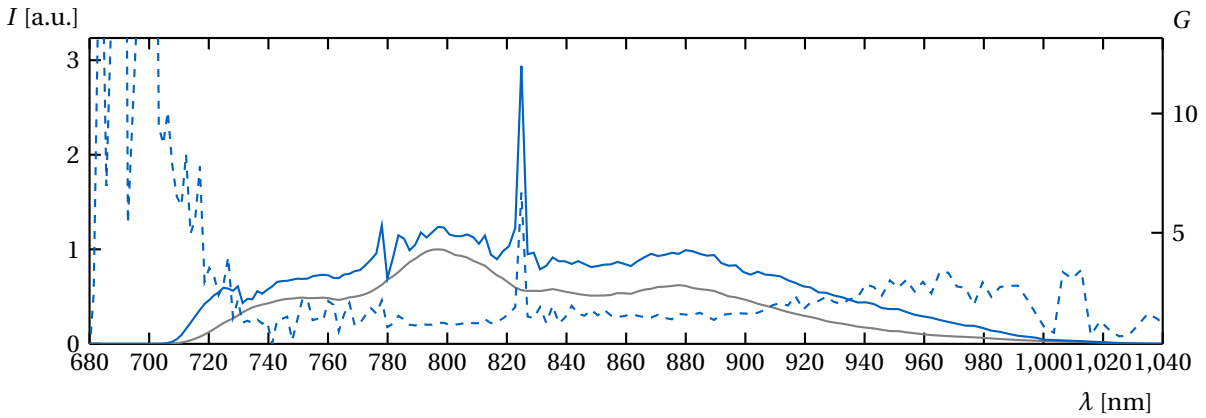

Fig. 3.23: Simulated spectrum (solid blue) and gain (dashed blue) of a 3 mm long 2A' crystal with $\theta = 23.75°$ after a 2A crystal with $L = 5\,\text{mm}$, $\theta = 23.69°$, $\alpha = 2.27°$ (black in figures 3.5, 3.12 and 3.14, the spectrum is represented here in gray).

2A' For 2A', the situation is similar. Although the gain curve for $\theta = 23.75°$ in figure 3.20b looks appropriate it lacks the input intensity around 700 nm resulting in an insignificant broadening, see figure 3.23. Howbeit, when operating stage 1B such that the spectral is weakened, there might be substantial gain with a 2A' stage. The narrow peak near 820 nm as well as the narrow width of the gain function are expected to be unphysical and caused by artifacts connected to discarding much information when exporting the 2A spectrum. Nevertheless, backed by figure 3.20a and the simulations of stages 1A and 2A, no large bandwidth enhancement neither energy increase is expected.

Contrarily, a contrast degradation due to OPF is very probable as well as detrimental spatial effects.

Additional crystal 1B'

As mentioned before, angular tuning is in theory much easier for the B stages and the almost symmetric behavior allows for broadening in both directions. Figure 3.24 shows that the analytic gain curve considerations are very well reflected qualitatively in the simulations. The beam profiles are of good quality, see figure 3.25. Decreasing the crystal angle leads to a larger separation of the gain peaks in the simulations as well. However, the gain is very weak because of the reduced crystal length of 2 mm. Since there are not so many detrimental effects expected in stage 1B', a longer crystal could be added. Crystal length is more critical in 2B.

In conclusion, adding thin crystals after each stage will help to eliminate the output spectrum gap as well as increase the seed for 2A and drive it into saturation. The present configuration allows for complete elimination of the gap if the A stages are tuned for a larger bandwidth, cf. figures 3.6 and 3.7 For achieving this, it would be necessary to detune especially the B stages as a whole. However, turning the B and B' crystals together after aligning them for an optimum individually is worth testing.

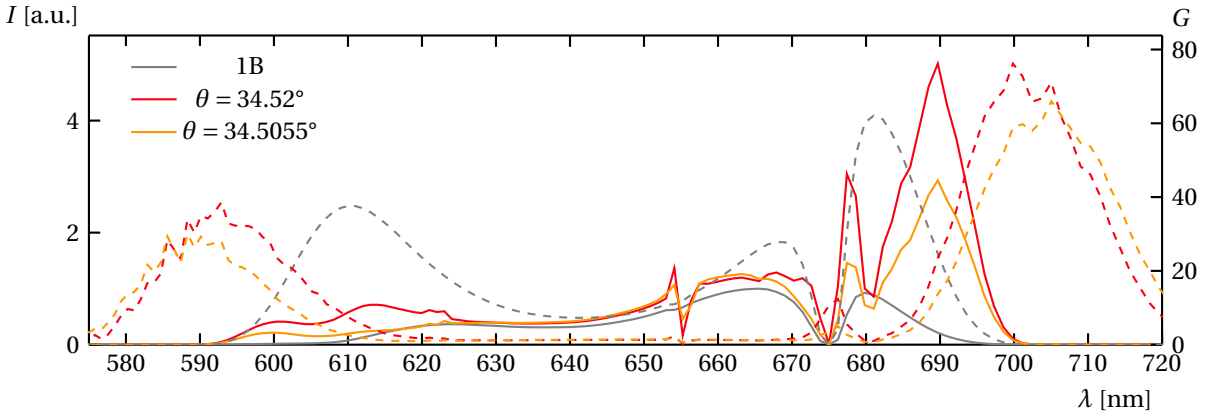

Fig. 3.24: Simulated spectrum (solid) and gain (dashed) of a 2 mm long 1B' crystal with $\theta = 34.52°$ (red) and $\theta = 34.5055°$ (orange) after a 1B crystal with $L = 4.5$ mm, $\theta = 34.58°$, $\alpha = 3.4°$ (red in figures 3.9 and 3.10). The 1B spectrum and the gain scaled by a factor of 10^{-2} is represented here in gray.

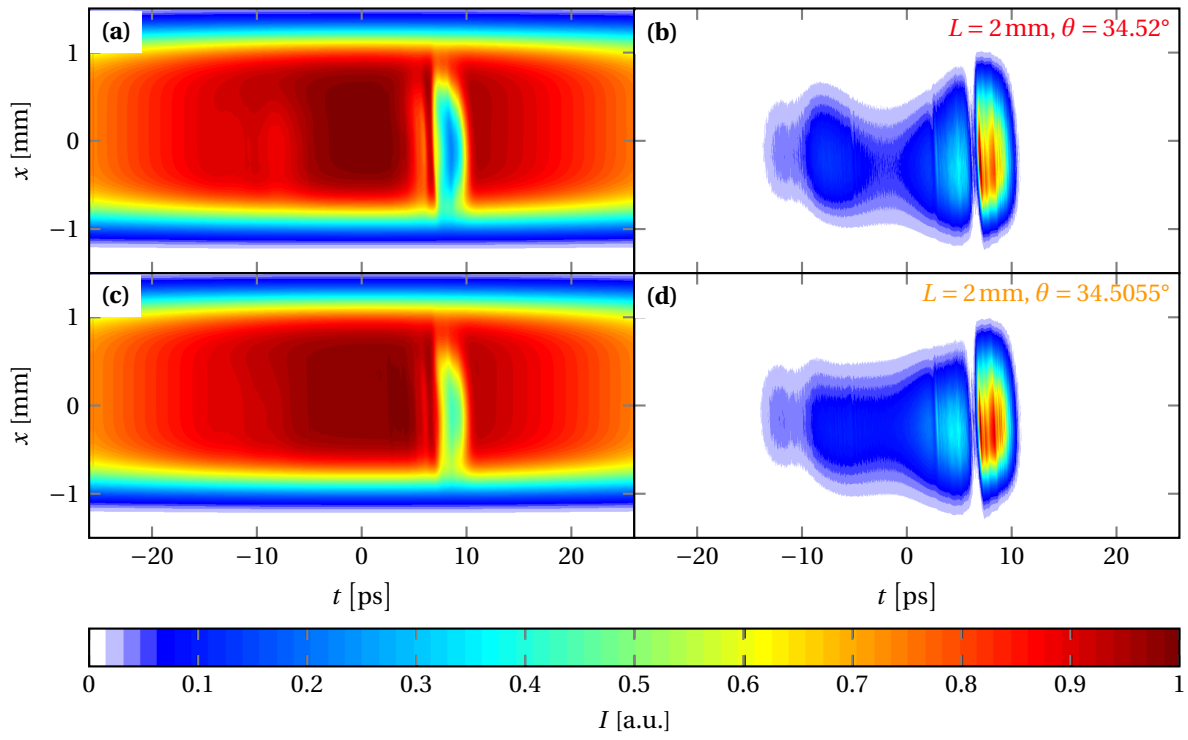

Fig. 3.25: Simulated spatio-temporal pulse profiles of pump (a, c) and signal (b, d) of a 2 mm long 1B' crystal with $\theta = 34.52°$ (a, b) and $\theta = 34.5055°$ (c, d) after a 1B crystal with $L = 4.5$ mm, $\theta = 34.58°$, $\alpha = 3.4°$ (red in figures 3.9 and 3.10).

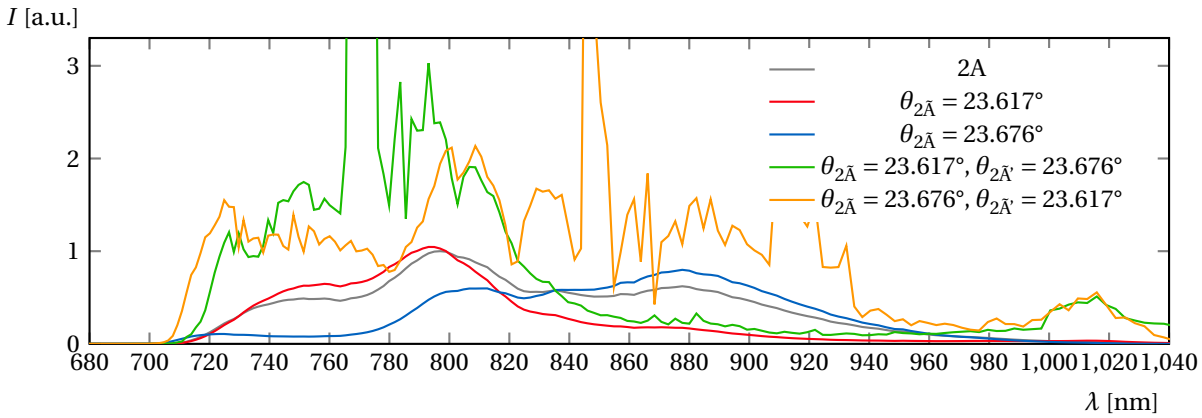

Fig. 3.26: Simulated spectra of 2Ã and 2Ã' crystals individually and after each other. Each crystal is 5 mm long and has an angle $\theta = 23.617°$ or $\theta = 23.676°$ with $\alpha = 2.27°$. For a comparison, the spectrum of 2A is plotted in gray.

3.4.2 Detuning the A crystals

A more sophisticated, yet substantially more tedious, approach might be applicable especially for the A stages. The crystals are to be replaced by two shorter ones, each detuned from the optimal such that their gain curves complement each other and give a broader combined gain. Compared to simply adding crystals to the existing setup geometry, it is more challenging to align this setup as the beam directions need to be changed for the right noncollinear angle and each angle needs to be optimized without experimentally obvious feedback on the optimal angles.

The new crystals are denoted as Ã and Ã'. Analytic calculations as well as varying the `Manipulate` sliders in `Mathematica` reveals only little prospect for improvement. A configuration with still some improvements was found to be $\alpha = 2.2395°$ and $\theta_\mathrm{i} = 23.617°$ and $\theta_\mathrm{ii} = 23.676°$ with a theoretical ambiguity in the order of the crystals. To understand the results better, simulations were conducted with two crystals with length of 5 mm each and the aforementioned angles. Both crystals were interchanged to see effects connected with the crystal order.

Nevertheless, test simulations were performed with the results displayed in figure 3.26. Similar to the simulation of crystal 2A', artifacts occur, producing mostly a very noisy output. For comparison of each single-crystal spectrum (red and blue) with the normal 2A spectrum, the crystal length was chosen to be 5 mm. The inset of back-conversion effects as well as OPF restricts the crystal length to thinner crystals in practice. However, even the resulting output of the long crystals indicates a small bandwidth increase compared to the present single-crystal 2A stage which on the one hand does not even reach down further than in section 3.4.1. On the other hand, the long-wavelength part gets amplified more which might help to improve overall efficiency.

When reducing the crystal length not only a dramatic decrease of the energy is expected but rather a narrower than a broader bandwidth. Weighing up the possibly higher amplification of the long-wavelength part and the much more tedious alignment in the laboratory, the benefit of the added degrees of freedom is questionable.

4 | Difference-frequency generation

A long-term goal for the LWS-20 has always been to obtain a stable carrier-envelope phase (CEP) for ultrafast highly-nonlinear experiments. So far, no measures have been implemented in order to reach that goal.

As discussed in the context of equation (1.25), the difference-frequency pulse of two pulses with the same phase will obtain a constant phase and is thus passively stabilized [37]. Intrapulse difference-frequency generation (DFG) after a spectral broadening of the seed will thus result in a passively CEP-stable OPCPA seed. Additionally, the nonlinearity of the process can be exploited for enhancing the temporal pulse contrast when used for OPCPA seed generation.

Recent reports of a conversion efficiency above 10 % [52] make DFG an interesting replacement option of the currently used cross-polarized wave generation (XPW) in the seed creation (cf. section 2.1). In this chapter, the efficiency of the process is tested in order to determine whether an implementation would be beneficial.

4.1 Setup

For testing DFG in our laser system, the pulses were picked up directly before XPW, i.e. after the hollow-core fiber (HCF) and the subsequent chirped mirror compressor (see figure 2.1). As the chirped mirrors over-compress the phase, additional fused silica windows were inserted at Brewster's angle. In order to achieve optimal compression, the amount of glass was varied by slightly detuning one of the windows. An as short as possible pulse is necessary because of the nonlinearity in the process which requires high intensities. Furthermore, a chirp is detrimental since the two frequency components participating should be present at the same time.

After compression, the beam was focused into a beta barium borate (BBO) crystal by a curved mirror with focal length $f = 500\,\mathrm{mm}$. The input power was 130 mW which corresponds to a pulse energy the spectrum is plotted in figure 4.1. The crystal's dimensions are $6\,\mathrm{mm} \times 6\,\mathrm{mm} \times 0.4\,\mathrm{mm}$, it is cut at $\theta_{\mathrm{cut}} = 29.2°$, $\phi = 90°$ and anti-reflection coated for second harmonic generation (SHG) of 800 nm. It was placed before the focus in order to avoid filamentation and to reach comparable intensities to those in [52]. The DFG spectra were measured with an intensity-calibrated spectrometer (Ocean Optics NIRQuest calibrated with Ocean Optics DH-3 plus-CAL-EXT). Its spectral range fits to the assumed difference frequency signal with wavelengths longer than 1400 nm.

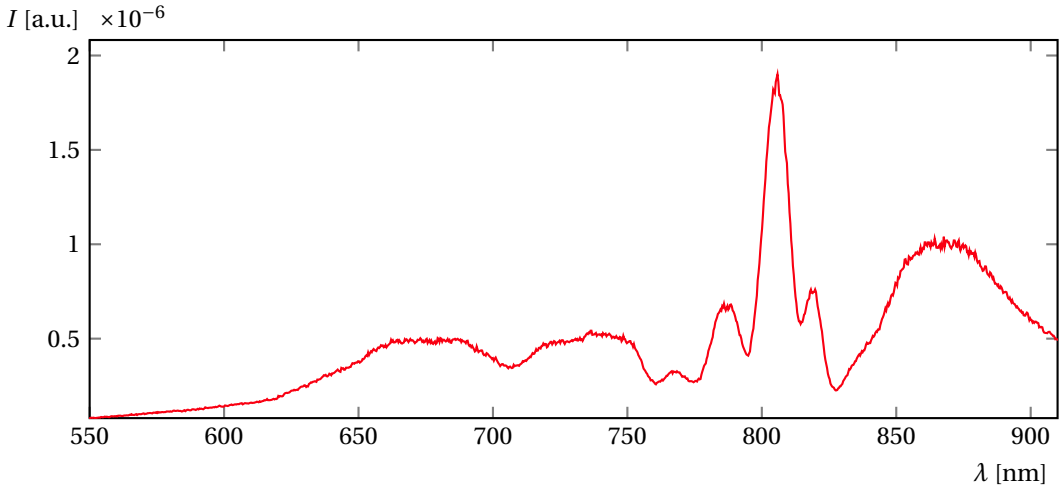

Fig. 4.1: Input spectrum for DFG that was taken after the HCF, the chirped mirror compressor and the fused silica bulks.

4.1.1 Phase matching

The collinear ($\alpha = 0$) DFG phase-matching angle θ_{DFG} is easily calculated using equations (1.6), (A.1), (A.4) and (A.5) for each of the phase-matching types (see table 1.1). The resulting angles have been plotted in figure 4.2 following the same naming convention as before such that $\lambda_{\mathrm{DF}} = \lambda_1 \geq \lambda_2 > \lambda_3$ and $\lambda_{2,3}$ are contained in the HCF output spectrum spanning from around 500 nm to 900 nm, cf. figure 4.1. The left panels in figure 4.2 show the respective phase-matching angle for DFG of the input wavelengths $\lambda_{2,3}$. The bleached-out areas correspond to a difference frequency below 1570 nm which was not expected to occur significantly given the input spectrum or above 2500 nm which is beyond the spectrometer range. The same holds for the completely white areas where additionally the phase matching angle is out of the range given by the color bar or no phase-matching is possible at all.

The right panels display the angular range under which a given difference frequency can be reached: the blue line is the upper limit which is obtained when producing the difference frequency of $\lambda_3 = 500\,\mathrm{nm}$ and a variable λ_2 whereas the orange line sets the lower limit, here $\lambda_2 = 900\,\mathrm{nm}$ is fixed and λ_3 varies accordingly.

For practical reasons, the input was polarized vertically which made adjusting the crystal angle more difficult. Several half-wave plates (HWPs) were tested to achieve an arbitrary polarization but there was none available which offered a sufficiently broad transmission. As a result of the reduced bandwidth, the difference frequencies would have been pushed to very long wavelengths and out of the observable range. For the same reason, the polarizer which is used for XPW was not used, at the cost of a slightly reduced polarization purity. The geometry for achieving the right DFG phase matching angle anyway is illustrated in figure 4.3. The crystal was mounted in a rotation mount which in turn was tilted by an angle θ_{yaw} around the vertical axes (a-b). Rotating the crystal around the rotation axis of the mount by

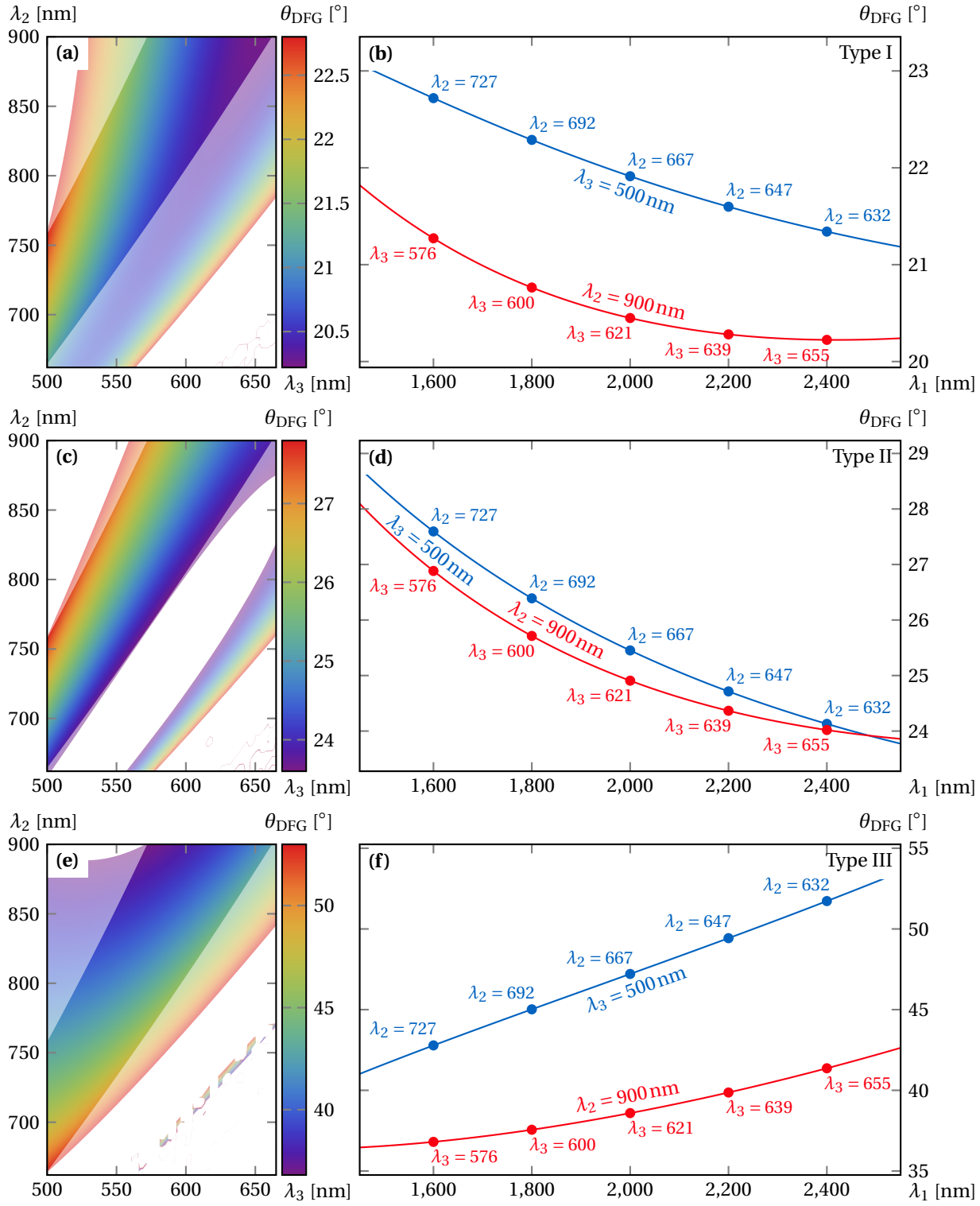

Fig. 4.2: (a,c,e) Calculated phase-matching angles for $1/\lambda_3 - 1/\lambda_2 = 1/\lambda_1$ depending on λ_3 (horizontal axis) and λ_2 (vertical axis), for type I to III. (b,d,f) Phase-matching angle range for the fundamental laser wavelengths depending on the difference frequency wavelength λ_1. Red: fixed $\lambda_2 = 900\,nm$, blue: fixed $\lambda_3 = 500\,nm$.

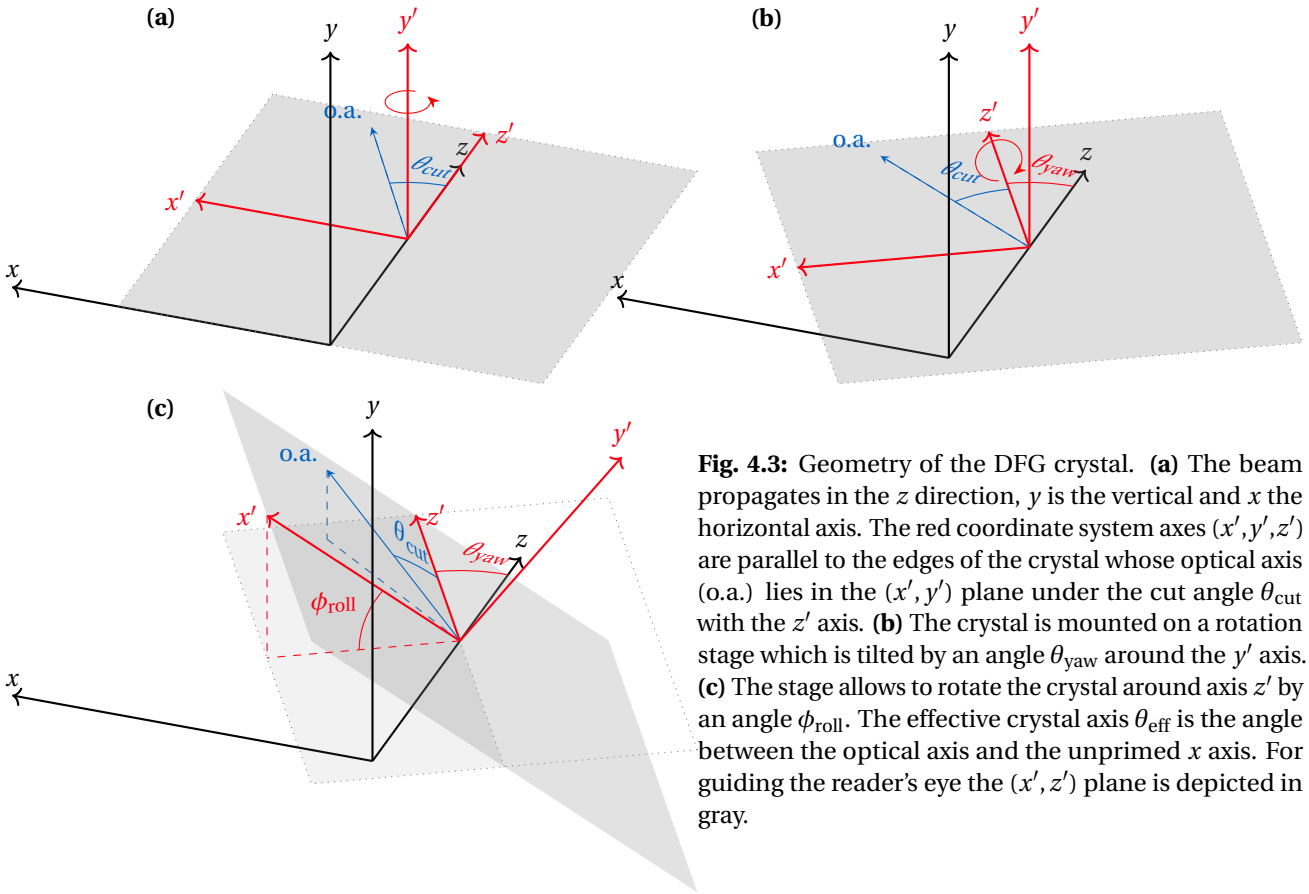

Fig. 4.3: Geometry of the DFG crystal. **(a)** The beam propagates in the z direction, y is the vertical and x the horizontal axis. The red coordinate system axes (x', y', z') are parallel to the edges of the crystal whose optical axis (o.a.) lies in the (x', y') plane under the cut angle θ_{cut} with the z' axis. **(b)** The crystal is mounted on a rotation stage which is tilted by an angle θ_{yaw} around the y' axis. **(c)** The stage allows to rotate the crystal around axis z' by an angle ϕ_{roll}. The effective crystal axis θ_{eff} is the angle between the optical axis and the unprimed x axis. For guiding the reader's eye the (x', z') plane is depicted in gray.

an angle ϕ_{roll} (b-c) yields an *effective* crystal angle θ_{eff}:

$$
\begin{aligned}
\theta_{\text{eff}} &= \arccos\left(\frac{A-B}{\sqrt{C^2+D^2+E^2}}\right);\\
A &= \cos(\theta_{\text{cut}})\cos(\theta_{\text{yaw}}),\\
B &= \cos(\phi_{\text{roll}})\sin(\theta_{\text{cut}})\sin(\theta_{\text{yaw}}),\\
C^2 &= \left(\cos(\phi_{\text{roll}})\cos(\theta_{\text{yaw}})\sin(\theta_{\text{cut}})+\cos(\theta_{\text{cut}})\sin(\theta_{\text{yaw}})\right)^2,\\
D^2 &= \left(\cos(\theta_{\text{cut}})\cos(\theta_{\text{yaw}})-\cos(\phi_{\text{roll}})\sin(\theta_{\text{cut}})\sin(\theta_{\text{yaw}})\right)^2,\\
E^2 &= \left(\sin(\phi_{\text{roll}})\sin(\theta_{\text{cut}})\right)^2.
\end{aligned}
\tag{4.1}
$$

In this way, the effective angle can be adjusted to any value. At least for the case of type I DFG, the effective azimuthal angle which is the angle between the principal plane and the (x, z) plane can be adjusted to 45°. Here, both extraordinary and ordinary component are equal, allowing for the best conversion efficiency.

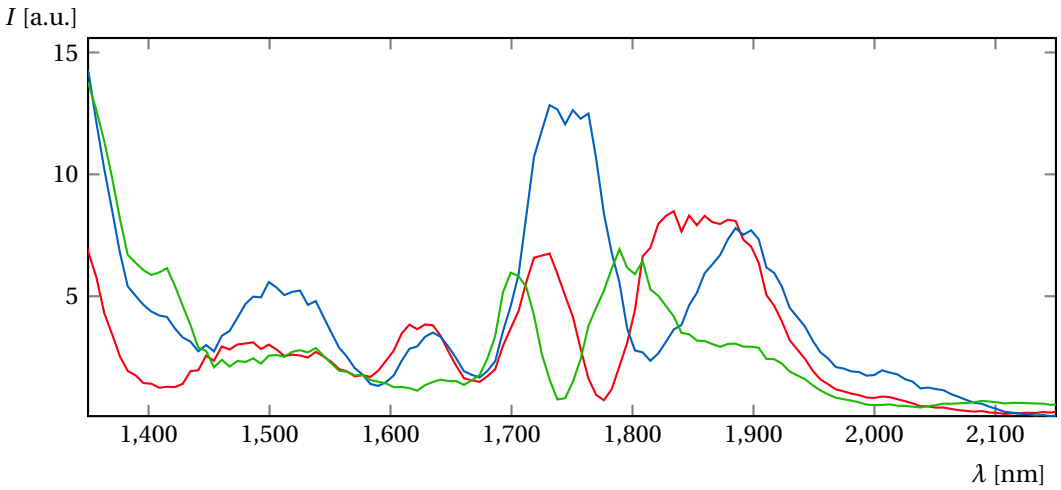

Fig. 4.4: DFG spectra for various compressions caused by turning one of the fused silica windows under otherwise constant conditions (uncalibrated).

4.2 Results and discussion

First of all, the compression was checked by tilting the thicker glass window and thereby changing the effective material dispersion. Figure 4.4 shows that this has a significant effect on the output. As the greatest effect of a change in compression is expected at the shortest pulse durations, the operation of the setup is near the optimal compression.

Experimentally, an angle of $\theta_{\text{yaw}} \approx 22°$ was found to produce clearly visible difference frequency components. The variation of the spectra with ϕ_{roll} was studied and thus, all considerations are made with respect to this angle.

4.2.1 Phase-matching types

First of all, it is useful not only for comparison to find the phase-matching types involved. As mentioned before, the major difference frequency components are expected above 1570 nm since these could be created from the spectral input parts carrying the largest energy. Experimentally, such difference frequency components were strong only at some crystal rotations. For a comparison with the theoretically calculated angles from figure 4.2, figure 4.5 compares the angular ranges of ϕ_{roll} under which a signal is theoretically expected (colored areas) with configurations where spectra were measured with a significant contribution above 1570 nm (darker areas).

Because of a lack of information about the exact position of the optical axes, there is an ambiguity of the corresponding azimuthal angles ϕ_{roll} to achieve a certain effective cut angle. This is represented by two mirrored, respectively 180° shifted, azimuthal plots for the calculated values. Furthermore, the zero angle for the experimental values might not be completely accurate. Nevertheless, this comparison allows to distinguish between the phase-matching types: The situation in figure 4.5a seems unrealistic due to the clear breakdown of a signal around 30° and 320° in between the darker shaded area where

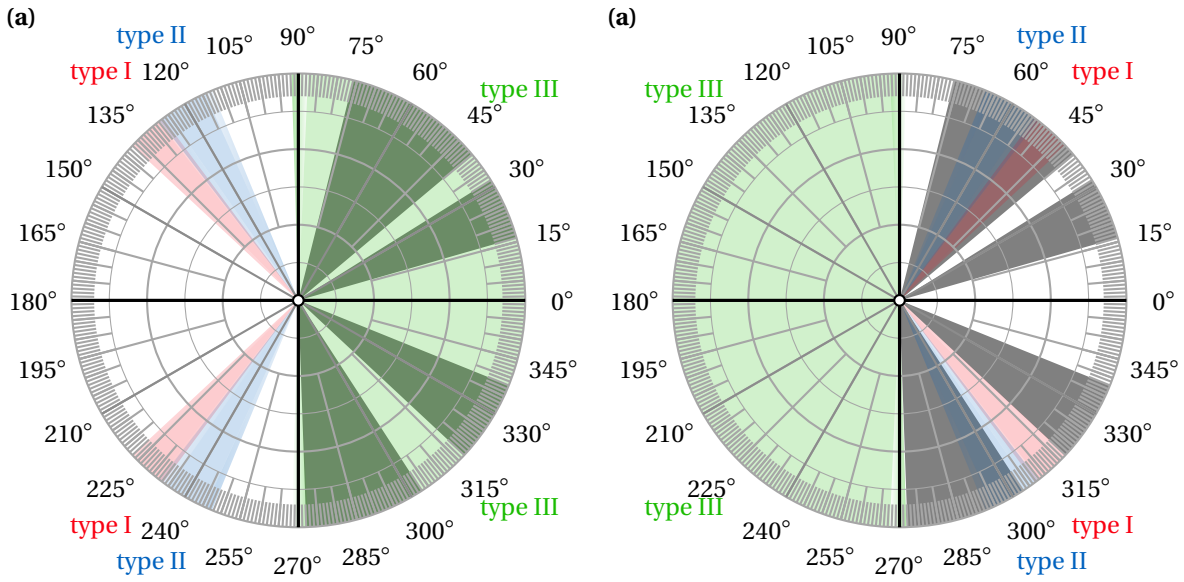

Fig. 4.5: Red, blue and green shaded areas: calculated ϕ_{roll} assuming $\theta_{\text{yaw}} = 22°$ under which DFG is possible for phase-matching types I, II and III, respectively, for a difference-frequency wavelength between 1570 nm and 2570 nm. Darker areas represent angular areas under which a signal was measured in the range 1600 nm to 2500 nm. (a) and (b) show the calculated ranges mirrored at the vertical axis to account for an ambiguity of the exact position of the optical axis.

the efficiency is expected to remain high when operating under the same phase-matching type. Even when considering the sinc^2-dependence of the intensity in equation (1.7), the expected areas for DFG do not broaden considerably (less than 2° per edge). Therefore, it is assumed that the observed angular areas correspond to type I and II phase matching.

4.2.2 Spectral features

As expected, the spectra with a similar absolute angle with respect to the horizontal have comparable features, cf. figure 4.6. In order to eliminate stray effects and higher order diffraction from shorter wavelength components which predominated, a long-pass filter was inserted to suppress all wavelengths $\lambda < 1100\,\text{nm}$. Furthermore, the spectrometer had been intensity-calibrated. By integrating the spectrum, the energy content of each wavelength range could be estimated. Therefore, it was assumed that the total area under the curve corresponds to the total measured power. This, of course, is not strictly true as the spectrometer range ends at 2500 nm. However, a more precise measurement was not possible when using filters and a power meter.

The spectra show a significant contribution of wavelengths in the area where mixing products of the fundamental and the difference frequency occur (the difference of the difference frequency and the fundamental). They will carry the same phase fluctuations as the fundamental and might even dominate. Phase-stability was not investigated here, but the whole region might be useless as a phase-stable OPCPA seed.

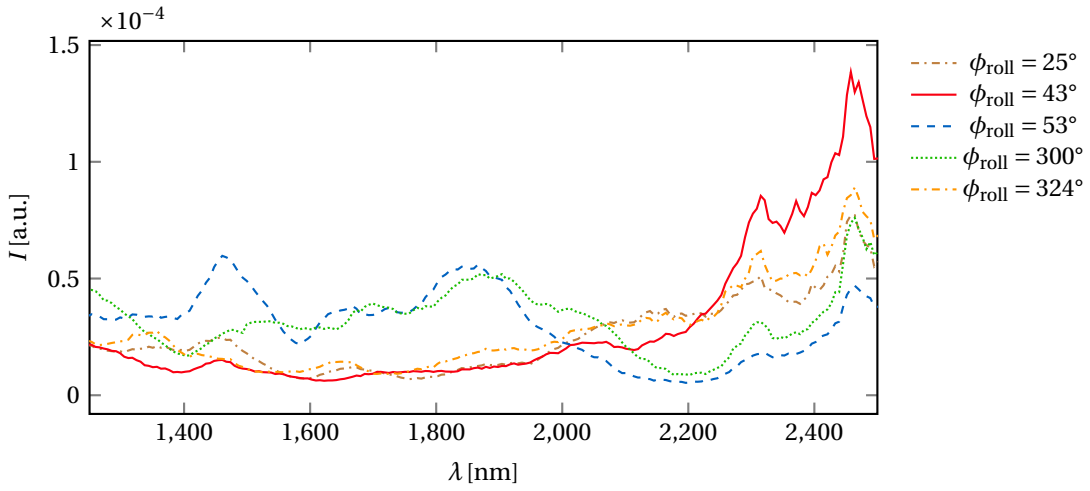

Fig. 4.6: Measured DFG spectra for various crystal rotation angles.

A dip in most spectra just below 1600 nm suggests that the limit between mixed DFG and mixing products has to lie close. This also makes sense when considering that for the difference frequency, $\lambda_{DF} \gtrsim 1600\,\text{nm}$. Then, the mixing products involving the peak of the input spectrum around 800 nm will be limited by $\lambda_{mix} \lesssim (800\,\text{nm})^{-1} - (1600\,\text{nm})^{-1} = (1600\,\text{nm})^{-1}$.

4.2.3 Conversion efficiency

Especially the spectra with a small absolute ϕ_{roll} are weak but exhibit steadily increasing intensity towards longer wavelengths. As the phase-matching angles decrease for longer difference frequencies, the contributions exceeding the spectrometer range might be slightly larger than expected. The total measured energy for $\lambda > 1100\,\text{nm}$ as well as the estimated spectral energies for $1570\,\text{nm} < \lambda < 2200\,\text{nm}$ and $2200\,\text{nm} < \lambda < 2500\,\text{nm}$ are given in table 4.1.

Considering the input energy of 130 µJ, the DFG efficiency lies below 3.5 %. By optimizing the geometry and putting the BBO crystal a bit closer to the focus, the efficiency could be raised a bit, but high DFG efficiency for unmixed DFG cannot be expected. Whilst the measured output energies would be still acceptable it should be considered that for the use of the difference frequency as seed for the LWS-20 the spectra must be shifted back to the fundamental wavelength, for example by the use of a photonic crystal fiber (PCF). This would introduce an additional loss of at least one order of magnitude. Placing the crystal in vacuum with a reduced focal spot size would enhance the efficiency as would the use of a special retardation plate which rotates the polarization of the spectral parts relative to each other [52]. Given the availability of the needed parts, both ideas might be considered for future testing. Yet at the moment, intra-pulse DFG of the seed is not a planned option for the LWS-20 laser system.

θ_{az}	$\theta_{cut,eff}$	$E_{>1100}$ [µJ]	$E_{1583-2196}$ [µJ]	$E_{2196-2501}$ [µJ]
25°	49.9° or 12.8°	1.55(1)	0.33	0.44
43°	47.5° or 19.4°	2.05(1)	0.34	0.92
48°	46.6° or 21.3°	3.30(3)	0.82	1.10
51°	46.0° or 22.4°	4.40(20)	1.46	0.44
53°	45.6° or 23.2°	4.34(2)	1.27	0.44
300°	44.1° or 25.7°	3.60(3)	1.18	0.55
304°	45.0° or 24.3°	2.72(1)	0.68	0.90
324°	48.6° or 16.8°	2.37(1)	0.50	0.68

Tab. 4.1: Overview of the experimental results of various characteristic measurements. As explained in the text, the second value for $\theta_{cut,eff}$ is supposed to be valid. $E_{>1100}$ is the measured value using a power meter and a long-pass filter, $E_{1583-2197}$ and $E_{2197-2501}$ are estimated values calculated from $E_{>1100}$ and the calibrated and integrated spectra.

4.3 Alternative strategy for CEP stability

An alternative strategy is active stabilization of the kHz system which is expected to reduce the phase fluctuations also for the output. The equipment for stabilization of the oscillator via a phase-locked loop (PLL) (phase locking electronics Menlo Systems XPS800) exists. The carrier-envelope offset (CEO) frequency is detected by a 0-f setup (cf. section 1.3.2) using an avalanche photodiode (APD) (APD210) and subsequently filtered and amplified (Menlo Systems OFD 80).

However the current alignment does not render it easy to produce the a sufficiently strong beat signal for phase-locking. Yet, optimizing the oscillator for phase-locking makes mode-locking more difficult which is why it has not been implemented yet in order not to encumber the experiments.

After a stabilization of the oscillator it is possible to observe the slower-fluctuating extra-cavity phase changes at different parts of the laser system using a setup as described in section 1.3.3. If they are not too big, a slow feedback loop could even be implemented for stabilization of the 10 Hz pulses.

5 | Conclusions

The goal of this thesis was on the one hand an investigation of possible enhancements of the non-collinear OPCPA (NOPCPA) system with respect to energy and bandwidth by performing simulations of the different existing stages as well as suggested changes in the setup. Furthermore, a possibility of creating a passively stabilized NOPCPA seed was tested.

The analytical framework presented in section 1.2.2 together with the simulations performed in chapter 3 are a very useful tool for assessing the performance of the NOPCPA stages. The former give way for quick estimations and choosing appropriate parameters for the simulations. Those in turn are time-consuming but account for depletion and spatial effects and thus allow to reproduce important features of the LWS-20 laser system.

The first task was the energy output optimization of LWS-20. As a relatively easily applicable result, the 2A conversion efficiency is increased by reducing the pump radius by up to 10 % (section 3.3). The pump beam size should ideally be adjustable in order to achieve the maximum possible pump intensity before detrimental effects, most notably back-conversion, set in. This especially because day-to day changes of the seed spectrum or the pump intensity are easier to compensate by experimental tuning than with slow simulations. Therefore, an adjustable telescope is needed with as little distortions of the relay imaging of the pump on the crystal as possible. Despite these challenges, the expected energy increase is a motivation for the associated efforts.

The second task was the spectral enhancing the spectral bandwidth of LWS-20. It has been shown both analytically and in the simulations that the blue-pumped amplifier stages (1B, 2B) offer both a more intuitive and more effective way to extend the wings of their gain curve by adding a thinner crystal right behind the present one (section 3.4.1). With that additional gain in the range of the spectral hole around 700 nm, an additional crystal might be useful also in the green-pumped stage 2A. However, placing additional crystals only in the A stages does barely help to achieve more amplification around 700 nm. Adding a ca. 3 mm long crystal behind each of the B crystals is expected to diminish the spectral hole considerably and to extend the spectrum towards lower wavelengths, possibly even to 575 nm. It offers a comparatively easily tunable measure for additional tweaking of the spectrum.

The idea of detuning the existing crystals and aiming at a broader combined amplification range has not shown to result in a considerably better spectrum than that one discussed above (section 3.4.2). Especially the detrimental effects, primarily contrast reduction due to optical parametric fluorescence (OPF), are expected to grow significantly. Consequently, it is sufficient to rely the experimentally more convenient solution which does not involve a complete detuning.

An upgrade of the LWS-20 with two additional stages for even higher energies is already partially available and is planned to be implemented. Similar simulations will be performed with the developed strategies in order to optimize the upgrade, as well.

With the results of chapter 3, a strategy for increasing the signal energy and a strong reduction of the spectral gap are at hand to be applied in the further development of the system.

The last task was tp investigate a passively CEP-stabilized front-end. The possibility of intra-pulse difference-frequency generation (DFG) for producing a phase-stable NOPCPA seed while enhancing its temporal contrast has been assessed experimentally (chapter 4). The observed conversion efficiency of a few percent is too low when considering that the spectrum has to be shifted back to the original range afterwards since this will decrease the energy further. An active stabilization of the kHz front-end is a possible approach for eliminating the phase fluctuations.

Appendix

A | Dispersion formulae

The formulae connected to dispersion that were used in the thesis can be found here.

A.1 Refractive index

For all calculations in the scope of this thesis, refractive indices were calculated using the following empirical Sellmeier's dispersion formulae:

$$n_{\mathrm{o,BBO}}(\lambda) = \sqrt{2.7359 + \frac{0.01878\,\mu\mathrm{m}^2}{\lambda^2 - 0.01822\,\mu\mathrm{m}^2} - 0.01354\,\mu\mathrm{m}^{-2}\lambda^2}, \tag{A.1a}$$

$$n_{\mathrm{e}\perp,\mathrm{BBO}}(\lambda) = \sqrt{2.3753 + \frac{0.01224\,\mu\mathrm{m}^2}{\lambda^2 - 0.01667\,\mu\mathrm{m}^2} - 0.01516\,\mu\mathrm{m}^{-2}\lambda^2}, \tag{A.1b}$$

$$n_{\mathrm{N-SF57}}(\lambda) = \sqrt{1 + \frac{2.30002\lambda^2}{\lambda^2 - 177.39\,\mu\mathrm{m}^2} + \frac{0.373757\lambda^2}{\lambda^2 - 0.064051\,\mu\mathrm{m}^2} + \frac{1.87544\lambda^2}{\lambda^2 - 0.014175\,\mu\mathrm{m}^2}}, \tag{A.2}$$

$$n_{\mathrm{FS}} = \sqrt{1 + \frac{0.897479\lambda^2}{\lambda^2 - 97.934\,\mu\mathrm{m}^2} + \frac{0.407943\lambda^2}{\lambda^2 - 0.0135121\,\mu\mathrm{m}^2} + \frac{0.696166\lambda^2}{\lambda^2 - 0.00467915\,\mu\mathrm{m}^2}}. \tag{A.3}$$

They were taken from [53] (BBO, according with [31]), [54] (N-SF57) and [55] (FS), respectively.

In the case of birefringence, the formulae for the two principal values n_{o} and $n_{\mathrm{e}\perp}$ are given. The component which is polarized perpendicular to the plane of propagation direction $\hat{k}$ and optical axis $\vec{a}$ is called *ordinary* and will thus have a refractive index which is independent of the angle $\theta = \angle(\hat{k}, \vec{a})$ of the propagation direction relative to the optical axis:

$$n_{\mathrm{o}}(\lambda, \theta) \equiv n_{\mathrm{o}}(\lambda)\,. \tag{A.4}$$

The beam with polarization lying in the plane, however, is called *extraordinary* and will experience a refractive index

$$n_{\mathrm{e}}(\lambda, \theta) = \left(\frac{\cos^2\theta}{n_{\mathrm{o}}^2(\lambda)} + \frac{\sin^2\theta}{n_{\mathrm{e}\perp}^2(\lambda)}\right)^{-1/2}. \tag{A.5}$$

A.2 Group velocity and spectral phase

For pulsed lasers in a dispersive medium, the group velocity v_g with which a pulse moves is different than the phase velocity $v_p = c/n$. It is related to the group index n_g:

$$n_g(\omega) = \frac{\partial(\omega n(\omega))}{\partial\omega} \tag{A.6}$$

$$v_g(\omega) = \frac{c}{n_g(\omega)}. \tag{A.7}$$

Very important effects are the group velocity dispersion (GVD) and group velocity mismatch (GVM):

$$GVD(\omega) = \frac{\partial}{\partial\omega}\frac{1}{v_g(\omega)} \tag{A.8}$$

$$GVM(\omega_1,\omega_2) = \frac{1}{v_g(\omega_1)} - \frac{1}{v_g(\omega_2)}. \tag{A.9}$$

The material length ℓ divided by the group velocity is equivalent to a group delay (GD) and the higher-order dispersions such as group delay dispersion (GDD), third-order dispersion (TOD), etc.:

$$GD(\omega,\ell) = \frac{\ell}{v_g(\omega)} = \frac{\partial\phi(\omega)}{\partial\omega} \tag{A.10}$$

$$GDD(\omega,\ell) = \frac{\partial GD(\omega,\ell)}{\partial\omega} \tag{A.11}$$

$$TOD(\omega,\ell) = \frac{\partial GDD(\omega,\ell)}{\partial\omega} \tag{A.12}$$

$$FOD(\omega,\ell) = \frac{\partial GDD(\omega,\ell)}{\partial\omega} \tag{A.13}$$

$$FID(\omega,\ell) = \frac{\partial GDD(\omega,\ell)}{\partial\omega}. \tag{A.14}$$

In the narrower sense GD, GDD, etc. are taken at the carrier frequency ω_c. As denoted, these are derivatives of the spectral phase $\phi(\omega)$ which is accumulated when traveling through a dispersive medium with the refractive index n_{Mat} over a propagation length ℓ:

$$\phi_{Mat}(\omega,\ell) = \omega\left(\frac{n_{Mat}(\omega)\cdot\ell}{c}\right). \tag{A.15}$$

Note that the offset of the GD is chosen freely such that $GD(\omega_c) = 0$.

B | List of Abbreviations

AOPDF acousto-optic programmable dispersive filter. 17, 19

APD avalanche photodiode. 56

ASE amplified spontaneous emission. 7

ATI above-threshold ionization. 21

BBO beta barium borate (β-BaB_2O_4). 4–6, 10, 19, 49, 55, III

CE carrier-envelope. 13, 15, 16, IX

CEO carrier-envelope offset. 13–15, 56

CEP carrier-envelope phase. iii, 3, 13, 15, 16, 21, 49, 56, 58

CPA chirped-pulse amplification. 1, 7

CPU central processing unit. 26

CUDA Compute Unified Device Architecture. 26

DF difference frequency. 14, 49–51, 53–55

DFG difference-frequency generation. iii, 3–5, 7, 49, 50, 52–55, 58, X

FF fundamental frequency. 16

FFT fast Fourier transform. 25, 26

FL Fourier limit(ed). 21

FS fused silica. 20, III

FT Fourier transform. 14, 15

FWHM full width at half maximum. 20

GD group delay. IV

GDD group delay dispersion. 14, 19, IV

GPO group-phase offset. 13, 14

GPU graphics processing unit. 26

GVD group velocity dispersion. IV

GVM group velocity mismatch. IV

HCF hollow-core fiber. 17, 49, 50

HHG high harmonic generation. 13

HWP half-wave plate. 50

iFFT inverse FFT. 25

LAP Laboratory for Attosecond and High-Field Physics. 17, XVII

LWS-20 Light Wave Synthesizer 20. iii, 1, 6, 8, 17, 23, 27, 28, 34, 49, 55, 57, 58, XVII

NIR near infrared. 6

NOPCPA noncollinear OPCPA. iii, 10, 17–19, 23, 27, 40, 57, 58

OPA optical parametric amplification. 1, 7, 8, 12, 18, 28–30

OPCPA optical parametric chirped-pulse amplification. 1, 3, 6, 8, 10, 12, 19, 21, 23, 26, 31, 49, 54, IX

OPF optical parametric fluorescence. 4, 43, 44, 48, 57

OPS optical parametric synthesizer. 18

OR optical rectification. 3, 4

PCF photonic crystal fiber. 14, 18, 55

PLL phase-locked loop. 56

PVWC Poynting vector walk-off compensation. 9, 10, 28, 29

QE quantum efficiency. 30

RAM random-access memory. 26

SFG sum-frequency generation. 3–5, 14

SH second harmonic. 14–16

SHG second harmonic generation. 3, 4, 12, 27–29, 49

SI spectral interferometry. 15, 16

SPDC spontaneous parametric down-conversion. 4

SPM self-phase modulation. iii, 6, 14, 17, 23–25

SVEA slowly varying envelope approximation. 12, 23, 24

TH third harmonic. 14

TL transform limit. 17

TOD third-order dispersion. IV

TPM tangential phase-matching. 9, 10, 21, 28, 29

WVM wave vector mismatch. 5, 8, 11, 12, 28, 30

XPW cross-polarized wave generation. 17, 19, 30, 49, 50

C | List of Figures

1.1 Schematic CPA principle 7
1.2 Principle of optical parametric amplification 8
1.3 Principle of collinear vs. noncollinear phase matching 9
1.4 PVWC vs. TPM geometry in a negatively birefringent crystal 10
1.5 A few-cycle pulse with a carrier frequency f_c, CEP ϕ_{CE} and a Gaussian envelope 13
1.6 A pulse train in the time domain is a frequency comb in the frequency domain 15

2.1 Layout of the LWS-20 laser system 18
2.2 Measured output spectrum of XPW and the full NOPCPA with calculated input GD . . . 19
2.3 Super-Gaussians of order 2 (normal Gaussian), 6 and 10 20

3.1 Possible second-order interactions of extraordinary and ordinary light fields 25
3.2 Working principle of the split-step code used by `chi2D.exe` 26
3.3 Angular sensitivity of phase-matching in the 1A stage 27
3.4 Noncollinear angle for OPA and SHG 29
3.5 Comparison of phase matching for three different 1A geometries 30
3.6 Simulated spectra of OPCPA crystal 1A for different phase-matching conditions 31
3.7 Simulated energy gain curves of OPCPA crystal 1A for different phase-matching conditions 32
3.8 Spatio-temporal intensity distributions of pump and signal after stage 1A 33
3.9 Comparison of phase matching for different 1B geometries 34
3.10 Simulated output spectrum and gain curve of stage 1B 35
3.11 Simulated spatio-temporal pump and signal pulse profiles after stage 1B 35
3.12 Simulated 2A spectra with varying pump radius 36
3.13 Effect of the 2A pump radius on efficiency and gain 36
3.14 Simulated 2A (effective) gain curves with varying pump radius 37
3.15 Simulated 2A pump and signal profiles with varying pump radius 38
3.16 Simulated 2A pump and signal profiles with varying pump radius 39
3.17 Measured effect of reducing the pump power on the final NOPCPA output 40
3.18 Phase-matching geometries $\alpha_{pm}(\theta)$ (a) and $\theta_{pm}(\alpha)$ (b) for A' stages. 41
3.19 Phase-matching geometries $\alpha_{pm}(\theta)$ (a) and $\theta_{pm}(\alpha)$ (b) for B' stages 42
3.20 Calculated gain curves for stages 1A,B, 1A',B', 2A,B and 2A',B'. 43
3.21 Simulated 1A' spectra and gain curves 44
3.22 Simulated 1A' pump and signal profiles 45
3.23 Simulated 2A' spectrum and gain 46

3.24 Simulated 1B' spectra and gain curves 47
3.25 Simulated 1B' pump and signal profiles 47
3.26 Simulated 2Ã, 2 A' spectra 48

4.1 difference-frequency generation input spectrum 50
4.2 Calculated phase-matching angles for DFG 51
4.3 Geometry of the DFG crystal 52
4.4 DFG spectra for various compressions 53
4.5 Comparison of calculated angular DFG phase-matching ranges and angles under which a spectrum was measured 54
4.6 Measured DFG spectra for various crystal rotation angles 55

D | List of Tables

1.1 Phase-matching types for SFG and DFG in BBO 5

2.1 Parameters of the OPCPA stages 21

3.1 Simulated 1A signal output energy and quantum efficiency 31

4.1 Measured DFG energies 56

E | Bibliography

[1] T. H. Maiman. Ruby laser systems, 1967. URL http://patft.uspto.gov/netacgi/nph-Parser?Sect2=PTO1&Sect2=HITOFF&p=1&u=/netahtml/PTO/search-bool.html&r=1&f=G&l=50&d=PALL&RefSrch=yes&Query=PN/3353115. U.S. Patent 3,353,115.

[2] F. J. McClung and R. W. Hellwarth. Giant Optical Pulsations from Ruby. *Applied Optics*, 1(S1):103, 1962.

[3] M. DiDomenico. Small-Signal Analysis of Internal (Coupling-Type) Modulation of Lasers. *Journal of Applied Physics*, 35(10):2870, 1964.

[4] L. E. Hargrove, R. L. Fork, and M. A. Pollack. Locking of He-Ne laser modes induced by synchronous intracavity modulation. *Applied Physics Letters*, 5(1):4, 1964.

[5] D. E. Spence, P. N. Kean, and W. Sibbett. 60-fsec pulse generation from a self-mode-locked Ti:sapphire laser. *Optics Letters*, 16(1):42, 1991.

[6] R. R. Alfano and S. L. Shapiro. Observation of Self-Phase Modulation and Small-Scale Filaments in Crystals and Glasses. *Physical Review Letters*, 24(11):592–594, 1970.

[7] A. Baltuška, Z. Wei, M. S. Pshenichnikov, and D. A. Wiersma. Optical pulse compression to 5 fs at a 1-MHz repetition rate. *Optics Letters*, 22(2):102, 1997.

[8] D. Strickland and G. Mourou. Compression of amplified chirped optical pulses. *Optics Communications*, 56(3):219–221, 1985.

[9] S. A. Akhmanov and R. V. Khokhlov. Concerning one possibility of amplification of light waves. *JETP*, 43:351–353, 1962.

[10] S. A. Akhmanov, A. I. Kovrigin, A. S. Piskarskas, V. V. Fadeev, and R. V. Khokhlov. Observation of parametric amplification in the optical range. *Soy. Phys. JETP*, 2:191–193, 1965.

[11] A. Dubietis, G. Jonušauskas, and A. Piskarskas. Powerful femtosecond pulse generation by chirped and stretched pulse parametric amplification in BBO crystal. *Optics Communications*, 88(4-6):437–440, 1992.

[12] C. Thaury and F. Quéré. High-order harmonic and attosecond pulse generation on plasma mirrors: basic mechanisms. *Journal of Physics B: Atomic, Molecular and Optical Physics*, 43(21):213001, 2010.

[13] F. Träger, editor. *Springer Handbook of Lasers and Optics*. Springer, Berlin, Heidelberg, 2nd edition, 2012. ISBN 978-3-642-19408-5.

[14] R. W. Boyd. *Nonlinear Optics*. Academic Press, Orlando, 3rd edition, 2008. ISBN 9780123694706.

[15] D. A. Kleinman. Nonlinear Dielectric Polarization in Optical Media. *Physical Review*, 126(6): 1977–1979, 1962.

[16] D. Eimerl, L. Davis, S. Velsko, E. K. Graham, and A. Zalkin. Optical, mechanical, and thermal properties of barium borate. *Journal of Applied Physics*, 62(5):1968–1983, 1987.

[17] D. F. Xue and S. Y. Zhang. Structure and Non-linear Optical Properties of β -Barium Borate. *Acta Crystallographica Section B Structural Science*, 54(5):652–656, 1998.

[18] R. L. Sutherland. *Handbook of Nonlinear Optics*, volume 36. Marcel Dekker, New York, NY, 2003. ISBN 9780824742435.

[19] J. E. Midwinter and J. Warner. The effects of phase matching method and of uniaxial crystal symmetry on the polar distribution of second-order non-linear optical polarization. *British Journal of Applied Physics*, 16(8):1135–1142, 1965.

[20] V. G. Dmitriev, G. G. Gurzadyan, and D. N. Nikogosyan. *Handbook of Nonlinear Optical Crystals*. Springer, Berlin, Heidelberg, 3rd edition, 1999. ISBN 9783642084720.

[21] D. Roberts. Simplified characterization of uniaxial and biaxial nonlinear optical crystals: a plea for standardization of nomenclature and conventions. *IEEE Journal of Quantum Electronics*, 28 (10):2057–2074, 1992.

[22] D. N. Nikogosyan. Beta barium borate (BBO). *Applied Physics A*, 52:359–368, 1991.

[23] W. Chen, A. Jiang, and G. Wang. Growth of high-quality and large-sized β-BaB2O4 crystal. *Journal of Crystal Growth*, 256(3-4):383–386, 2003.

[24] M. Pessot, P. Maine, and G. Mourou. 1000 Times Expansion/Compression of Optical Pulses for Chirped Pulse Amplification. *Optics Communications*, 62(6):419–421, 1987.

[25] R. Weber, B. Neuenschwander, and H. Weber. Thermal effects in solid-state laser materials. *Optical Materials*, 11(2-3):245–254, 1999.

[26] S. Chénais, F. Druon, S. Forget, F. Balembois, and P. Georges. On thermal effects in solid-state lasers: The case of ytterbium-doped materials. *Progress in Quantum Electronics*, 30(4):89–153, 2006.

[27] S. K. Zhang, M. Fujita, H. Y. R. Kodama, H. F. M. Nakatsuka, and Y. I. C. Yamanaka. Study on High Gain Broadband Optical Parametric Chirped Pulse Amplification. 3886:588–595, 2000.

[28] A. V. Smith, D. J. Armstrong, and W. J. Alford. Increased acceptance bandwidths in optical frequency conversion by use of multiple walk-off-compensating nonlinear crystals. *Journal of the Optical Society of America B*, 15(1):122, 1998.

[29] J. Matyschok, T. Lang, T. Binhammer, O. Prochnow, S. Rausch, M. Schultze, A. Harth, P. Rudawski, C. L. Arnold, A. L'Huillier, and U. Morgner. Temporal and spatial effects inside a compact and CEP stabilized, few-cycle OPCPA system at high repetition rates. *Optics Express*, 21(24):29656, 2013.

[30] T. Lang. *Ultrashort Laser Pulses from Optical Parametric Amplifiers and Oscillators*. Phd thesis, Gottfried-Wilhelm-Leibniz-Universität Hannover, 2014.

[31] T. Lang, A. Harth, J. Matyschok, T. Binhammer, M. Schultze, and U. Morgner. Impact of temporal, spatial and cascaded effects on the pulse formation in ultra-broadband parametric amplifiers. *Optics Express*, 21(1):949, 2013.

[32] J. A. Armstrong, N. Bloembergen, J. Ducuing, and P. S. Pershan. Interactions between Light Waves in a Nonlinear Dielectric. *Physical Review*, 127(6):1918–1939, 1962.

[33] I. N. Ross, P. Matousek, G. H. C. New, and K. Osvay. Analysis and optimization of optical parametric chirped pulse amplification. *Journal of the Optical Society of America B*, 19(12):2945, 2002.

[34] I. Ross, P. Matousek, M. Towrie, A. Langley, and J. Collier. The prospects for ultrashort pulse duration and ultrahigh intensity using optical parametric chirped pulse amplifiers. *Optics Communications*, 144(1-3):125–133, 1997.

[35] L. Xu, T. W. Hänsch, C. Spielmann, A. Poppe, T. Brabec, and F. Krausz. Route to phase control of ultrashort light pulses. *Optics Letters*, 21(24):2008, 1996.

[36] F. W. Helbing, G. Steinmeyer, J. Stenger, H. R. Telle, and U. Keller. Carrier-envelope-offset dynamics and stabilization of femtosecond pulses. *Applied Physics B: Lasers and Optics*, 74(SUPPL.):35–42, 2002.

[37] G. Cerullo, A. Baltuška, O. D. Mücke, and C. Vozzi. Few-optical-cycle light pulses with passive carrier-envelope phase stabilization. *Laser & Photonics Reviews*, 5(3):323–351, 2011.

[38] Z. Wei, H. Han, W. Zhang, Y. Zhao, J. Zhu, H. Teng, and Q. Du. Measurement and Control of Carrier-Envelope Phase in Femtosecond Ti:sapphire Laser. In M. Grishin, editor, *Advanced Solid-State Lasers: Development and Applications*, pages 301—-318. INTECH, Croatia, 2010. ISBN 9789537619800.

[39] M. Mehendale, S. A. Mitchell, J.-P. Likforman, D. M. Villeneuve, and P. B. Corkum. Method for single-shot measurement of the carrier envelope phase of a few-cycle laser pulse. *Optics Letters*, 25(22):1672, 2000.

[40] M. Kakehata, H. Takada, Y. Kobayashi, K. Torizuka, Y. Fujihira, T. Homma, and H. Takahashi. Single-shot measurement of carrier-envelope phase changes by spectral interferometry. *Optics Letters*, 26(18):1436, 2001.

[41] M. Kakehata, Y. Fujihira, H. Takada, Y. Kobayashi, K. Torizuka, T. Homma, and H. Takahashi. Measurements of carrier-envelope phase changes of 100-Hz amplified laser pulses. *Applied Physics B: Lasers and Optics*, 74(SUPPL.):43–50, 2002.

[42] T. H. Dou, R. Tautz, X. Gu, G. Marcus, T. Feurer, F. Krausz, and L. Veisz. Dispersion control with reflection grisms of an ultra-broadband spectrum approaching a full octave. *Optics Express*, 18 (26):27900, 2010.

[43] J. Tan. *Contrast and Dispersion Management in an OPCPA System*. Master's thesis, Ludwig-Maximilians-Universität München, 2016.

[44] F. Tavella. *Multiterawatt few-cycle pulse OPCPA for applications in high-field physics*. Phd thesis, Ludwig-Maximilians-Universität München, 2007.

[45] G. Arisholm, R. Paschotta, and T. Sudmeyer. Limits to the power scalability of high-gain optical parametric amplifiers. *J. Opt. Soc. Am. B*, 21(3):578, 2004.

[46] D. Herrmann, L. Veisz, R. Tautz, F. Tavella, K. Schmid, V. Pervak, and F. Krausz. Generation of sub-three-cycle, 16 TW light pulses by using noncollinear optical parametric chirped-pulse amplification. *Optics Letters*, 34(16):2459, 2009.

[47] T. Wittmann, B. Horvath, W. Helml, M. G. Schätzel, X. Gu, A. L. Cavalieri, G. G. Paulus, and R. Kienberger. Single-shot carrier–envelope phase measurement of few-cycle laser pulses. *Nature Physics*, 5(5):357–362, 2009.

[48] J. A. Fleck, J. R. Morris, and M. D. Feit. Time-dependent propagation of high energy laser beams through the atmosphere. *Applied Physics*, 10(2):129–160, 1976.

[49] J. A. Fleck and M. D. Feit. Beam propagation in uniaxial anisotropic media. *Journal of the Optical Society of America*, 73(7):920, 1983.

[50] D. Herrmann, C. Homann, R. Tautz, M. Scharrer, P. S. Russell, F. Krausz, L. Veisz, and E. Riedle. Approaching the full octave: noncollinear optical parametric chirped pulse amplification with two-color pumping. *Optics Express*, 18(18):18752, 2010.

[51] B. Mayer. *State-of-the-art high power laser development - Observation and control of phase matching in optical parametric chirped pulse amplification*. Master's thesis, Technische Universität München, 2011.

[52] H. Fattahi, A. Schwarz, S. Keiber, and N. Karpowicz. Efficient, octave-spanning difference-frequency generation using few-cycle pulses in simple collinear geometry. *Optics Letters*, 38 (20):4216, 2013.

[53] K. Kato. Second-harmonic generation to 2048 Å in β-Ba2O4. *IEEE Journal of Quantum Electronics*, 22(7):1013–1014, 1986.

[54] Schott AG. Optisches Glas: Datenblätter, 2015. URL `http://www.schott.com/advanced_optics/german/abbe_datasheets/schott-datasheet-all-german.pdf`.

[55] I. H. Malitson. Interspecimen Comparison of the Refractive Index of Fused Silica. *Journal of the Optical Society of America*, 55(10):1205, 1965.

Acknowledgments

> *Give thanks in all circumstances, for this is the will of God in Christ Jesus for you.*

1 Thess 5:18, *The Holy Bible*, English Standard Version

This thesis as a final project of my studies in physics involved many people in some or the other way. First of all, I owe gratitude to God, my heavenly father, who never left my side during all my studies.

Big thanks go to Prof. Dr. Laszlo Veisz, our group leader and my supervisor for giving me the possibility to work with his extraordinary group and sharing his deeper insights and experience trying to push science, but also everyone forward in order to achieve the best for all. I wish him good luck in the ongoing transition to Umeå university and a successful (not only) scientific life there!

It was an honor for me to be part of Prof. Dr. Ferenc Krausz' world-renowned Laboratory for Attosecond and High-Field Physics.

As hinted before, I would like to thank everyone in the LWS-20 team: Dr. Boris Bergues, Dr. Antonin Borot, Daniel Cardenas for spending two full days trying to phase-lock the oscillator with me, Shao-Wei Chou, Dr. William Dallari, Luisa Hofmann, Alexander Muschet, Daniel Rivas, Dr. Hartmut Schröder, Jeryl Tan for being my faithful office neighbor, Dr. George Tsakiris and Dr. Matthew Weidman. Thanks for letting me squeeze in, using your laser during your breaks and for the nice atmosphere. Speaking of which, cheers to my office mates Christian Burger, Harald Fuest, Till Klostermann, Marcel Neuhaus, Philipp Rupp and Johannes Stierle for having fun together in between the hard work.

Tino Lang's software `chi2D` was an essential tool for keeping the my simulation computer busy. Thanks for sharing the software and trying to fix the issues corresponding to very large arrays! I am grateful to Wolfang Huber, too, for setting up our new PCs and always immediately helping with several hard- and software problems.

During my studies, I was supported by the German National Academic Foundation (Studienstiftung des deutschen Volkes), both financially and intangibly, including countless inspiring conversations with other scholarship holders.

Last but not least, I am grateful for my faithful family and friends from SMD, my two "homes" who supported me not only in prayer throughout all my studies but also with great fellowship as well as my flat mates for being so relaxed with me during the stressful final weeks.

Erklärung

Hiermit erkläre ich, die vorliegende Arbeit selbständig verfasst zu haben und keine anderen als die in der Arbeit angegebenen Quellen und Hilfsmittel benutzt zu haben.

München, den 19. April 2016

_____

Pascal Jordan Weinert